Mechanical Regulation of Glioma Cell Migration

A DISSERTATION
SUBMITTED TO THE FACULTY OF THE
UNIVERSITY OF MINNESOTA
BY

Ghaidan Abdullah Sallam Shamsan

IN PARTIAL FULFILLMENT OF THE REQUIREMENTS
FOR THE DEGREE OF
DOCTOR OF PHILOSOPHY

Adviser: David J. Odde

January 2021

بِسْمِ اللَّـهِ الرَّحْمَـٰنِ الرَّحِيمِ

This dissertation is dedicated to my late father, and to my entire family who has supported me throughout my life. In particular, my eldest brother, Sanad Shamsan, who has always supported my academic pursuit. I am eternally grateful for your sacrifices and always believing in me.

Acknowledgements

I would like to thank my adviser, Dr. David Odde, for all his support and guidance throughout my graduate school. His thoughtful insights, passion for science, and compassion have made my graduate school experience very rewarding. I am deeply grateful for his mentorship.

My sincerest thanks to my dissertation committee (Dr. David Largaespada, Dr. Paolo Provenzano, and Dr. Patrick Alford) for their constant support and guidance. I particularly want to thank Dr. Largaespada for opening up his lab to conduct my research and collaborate with members of his lab. I also thank Dr. Steven Rosenfeld for providing thoughtful insights with regards to my projects. I would also like to thank the entire Biomedical Engineering department staff for their support and the fun conversations we had over the years. I am also thankful for our building custodians, in particular Geitu Osman, who I had the chance to interact and eat dinner with while working late in the lab.

I also would like to thank past and current members of the Odde lab: Brannon McCullough, Brian Castle, Benjamin Bangasser, Becky Klank, Emily Tubman, Louis Prahl, Chao Liu, Mahya Hemmat, Nima Ghaderi, Mariah McMahon, Sarah Anderson, Riley Manning, Lexi Doersch, and Nikolaos Memmos, whom I had the pleasure to know and interact with on a daily basis. Specifically, I want to thank Louis Prahl and Chao Liu for being great lab mates and amazing friends outside the lab. I am thankful for Becky Klank and Benjamin Bangasser for training me when I first joined the lab, and Brian Castle for all his guidance and help with microscopes. I thank undergraduate students: Brooke Braman, Jonathan Maleska, and Matthew Baxter, whom I worked with and got to know. Specifically, I want to thank Brooke Braman for her inspiring dedication and scientific contributions to this dissertation. I thank everyone who contributed to this dissertation.

Special thanks to all my awesome friends: Anh La, Steven Lee, Allison Siehr, Rohit Dhume, Lazarina (Inka) Gyoneva, Zeeshan (Zee) Syedain, Supriya Thathachary, Edgar Peña, Molly Kupfer, Rachel Edwards, George Markou, Ajay Dixit, Igor Dodevski, and Wes Errington. Thank you for your friendship.

Last and certainly not least, I thank my mom, my siblings and my nephews and nieces for their love, support, and encouragement throughout the years.

Abstract

Glioblastoma is an incurable aggressive brain tumor with median survival of less than 17 months. In Glioblastoma, tumor spreading is driven by tumor cells' ability to infiltrate healthy brain parenchyma, which prevents complete surgical resection and contributes to tumor recurrence. Thus, understanding the mechanisms driving glioblastoma cancer cell migration is critical for the development of effective anti-migratory therapies. Through extensive genomic analyses, distinct molecular subtypes were identified—proneural, classical and mesenchymal— and were shown to strongly correlate with specific genetic alterations (Mesenchymal: *NF1*; Classical: *EGFRvIII*; Proneural: *PDGFRA*). In this dissertation, I developed genetically induced tumor mouse models of human glioblastoma subtypes to study the migration behavior of mesenchymal and proneural cancer cells. Using a multidisciplinary approach, I identified key mechanistic differences between glioblastoma molecular subtypes involving cancer cell migration and immune cell infiltration. Using mathematical modeling, we demonstrated the elevation of adhesion molecules, notably the glycoprotein CD44, leads to enhanced cancer cell migration and force generation.

In the second part of my thesis, I developed a 2-dimensional compliant substrate to study the biophysics of CD44-dependent adhesion. Using immobilized anti-CD44 antibody, I demonstrated the ability of CD44 to support cell adhesion, migration and force transmission. Furthermore, I showed CD44-mediated migration and force transmission are stiffness and adhesion sensitive as predicted by a motor-clutch mechanism. In summary, this dissertation supports the role of CD44 as an adhesion molecule mediating glioblastoma cancer cell migration and highlights its therapeutic potential as an anti-migratory target. In addition, the work in this thesis informs future studies to explore targeting CD44 to slow glioblastoma cancer cell migration and to identify the factors driving immune cell infiltration in mesenchymal glioblastoma.

Table of Contents

List of Tables

List of Figures

Chapter 1

Introduction

1.1. Malignant brain tumors: Glioblastoma

Malignant brain tumors are one of the most feared types of tumors due to their poor prognosis and patient's low quality of life during the course of treatment [1]. Malignant gliomas account for 70% of all malignant brain tumors with ~17,000 new cases annually diagnosed, in the US alone, and an annual incidence of 5.26 per 100,000 [2]. Glioblastoma (World Health Organization (WHO) Grade IV) is one of the most common types of malignant gliomas with an incidence rate of 3.19 cases per 100,000 and accounts for 16% of all central nervous system (CNS) tumors [2]. Glioblastoma is a devastating, currently incurable disease with median survival of 15 months and a five-years survival rate under 5% [2].

Glioblastoma is highly aggressive due to the highly mitotic and invasive glioma cells. Recent work suggested the origin of glioma cells in glioblastoma is most likely neural stem cells within the subventricular zone [3]. In glioblastoma, glioma cells are able to infiltrate healthy brain parenchyma and spread beyond the tumor core, which makes achieving complete surgical resection very challenging. Typically, patients diagnosed with glioblastoma undergo surgery followed by radiation and chemotherapy [4]. However, despite these aggressive approaches, tumor recurrence occurs in almost all patients and long-term control of the disease is rarely achieved [5]. Patients with recurrent glioblastoma have

even worse survival outcome than primary glioblastoma with median survival of only ~9 months [5]. It is thought that the infiltrating tumor cells play a major role in tumor reoccurrence.

1.2. Glioblastoma therapies and clinical development

Historically, surgical resection and radiation have been used to treat patients diagnosed with GBM. In 2005, Temozolomide (TMZ), a DNA alkylating chemotherapy agent, was shown to improve overall survival when administered in combination with radiation therapy [6]. TMZ targets rapidly dividing cells and causes cell death as a results of accumulating DNA damage. Since the introduction of TMZ, different prognostics marker associated with survival outcome have been identified. *MGMT* promoter methylation has been shown to positively correlate with survival outcome and confers radiation and TMZ sensitivity [7]. In addition to MGMT promoter methylation, *IDH* mutations have been identified as a prognostic marker in gliomas. *IDH* mutations are most common in grade II and III astrocytomas and oligodendrogliomas and only present in less than 10% of primary glioblastomas [8]. Patients whose tumors harbor mutations in *IDH1* or *IDH2* were shown to have better survival outcome in response to standard of care therapy [8].

Many pharmacological interventions have been tried in glioblastoma and failed. Cilengitide, an integrin inhibitor peptide, was designed to target glioblastoma cell invasion by inhibiting αvβ3 and αvβ5 integrins but failed in a phase III clinical trial [9]. In addition, immunotherapy approaches have failed to show efficacy in improving clinical outcome [10]. Despite the numerous failed

phase III clinical trials, a more recent success emerges from the use of tumor-treating fields (TTF), a device-based therapy that transmit low-intensity electric fields which affect dividing cells [11]. TTF has been shown to improve progression free survival and overall survival in newly diagnosed glioblastoma [12]. Overall, the large number of failed clinical trials in glioblastoma highlights the need for better understanding of glioblastoma biology and better therapeutic targets.

1.3. Glioblastoma molecular subtypes

In an effort to better understand the biology of glioblastoma, genomic studies were utilized to identify the genetic and molecular changes associated with glioblastoma. In addition to the identification of *IDH* mutations and *MGMT* methylation discussed above, frequent genetic alterations within the RTK/RAS/PI3K, p53 and RB signaling pathways in glioblastoma were identified [13]. In addition, based on gene expression profiling, three distinct molecular subtypes: proneural, classical, and mesenchymal were identified and shown to strongly correlate with specific genetic alterations [14–16]. Proneural subtype is associated with mutations in *IDH1* (~30% of cases) and high expression of *PDGFRA*. Classical subtype is associated with high expression of *EGFR* and *EGFRvIII*. Lastly, mesenchymal subtype is associated with deleterious mutations and downregulation of *NF1*[15]. Single cell transcriptomic analyses and lineage tracing also demonstrate intra-tumoral subtype heterogeneity, subtype plasticity and correlation between cellular developmental states and molecular subtypes. [16–18]. Despite accumulating evidence of distinct transcriptomic and genetic signatures, the characteristic mechanistic differences between such signatures, if

any, have not been identified. As a result, it remains unclear how knowledge of the different subtypes should inform clinical decisions.

1.4. Process of cell migration

Cell migration is an important biological process that plays a key role in a variety of biological and pathological conditions including embryogenesis, wound healing, immune response, and cancer invasion and metastasis [19]. A classical view of cell migration is depicted as a multistep process involving membrane extension, formation and stabilization of attachments at the leading edge, and simultaneous contraction and rear adhesion release [20]. While this simple model depicts cell migration as a multistep process, in realty cell migration is an integrated, dynamic process involving active interaction between the cell cytoskeleton network, cell surface proteins, and the extracellular matrix [21]. Many studies have shown that cell migration depends on several factors including adhesion strength, type of substratum, external chemical and mechanical cues, and the organization of the cellular cytoskeleton [21]. These interactions have been heavily studied in the last few decades providing a working knowledge of the molecular parts and how they work together, which has allowed the field to start developing mathematical models that best depict cell migration behavior and predict new emergent behaviors.

1.5. Mathematical modeling of cell migration

DiMilla *et al*. were one of the first to develop a mathematical model describing cell migration as a function of adhesion density, or “adhesivity” [22]. Their model incorporated cytoskeletal force generation, cell polarization, and adhesion

dynamics and predicted a maximum migration speed at an intermediate “optimum” adhesivity. If adhesivity is very high, the cell is strongly adhered and unable to release rear adhesions, whereas if adhesivity is very low, the cell is unable to form and stabilize attachment at the leading edge and therefore cannot generate enough force for motion. These predictions were confirmed by measuring cell speeds on substrates coated with varying concentrations of ECM proteins [22,23].

A mathematical model of force transmission was developed to explain stiffness sensitive traction force dynamics and transmission based on the motor-clutch hypothesis [24,25]. In the widely used motor-clutch model, molecular motors transmit forces to the external environment through actin filaments and transmembrane molecular clutches. The motor-clutch model incorporates actin retrograde flow powered by myosin II motor proteins and molecular clutches which resists actin retrograde when coupled to the substrate. The key parameters in the model consists of the number of clutches and motors (n_c, n_m), clutch binding and unbinding rates (k_{off}, k_{on}), unloaded actin retrograde flow velocity (v_u), clutch rupture force and spring constant (F_b, κ_c), motor stall force (F_m) and substrate spring constant (κ_{sub}) [24]. Four key equations govern the interactions between the different components. The effective dissociation rate is governed by a Bell Model $k_{off}^{*} = k_{off} * e^{(\frac{Fclutch}{Fb})}$, where $F_{clutch} = \kappa_c * (x - x_{sub})$ and x is the clutch position and x_{sub} is substrate position. In addition, a linear force-velocity relationship defines F-actin retrograde flow $v_{filaments} = v_u(1 - \frac{\kappa_{sub} * x_{sub}}{F_{stall}})$ where $F_{stall} = n_m * F_m$ [24]. Since its early development, the motor-clutch model has been successfully

adapted to investigate key aspects of mechanotransduction including rigidity sensing, adhesion reinforcement, viscoelasticity sensing, and ligand density and distribution [24,26–34]

In recent work, we extended the motor-clutch model to simulate whole cell migration behavior [35,36]. The cell migration simulator (CMS) links together multiple motor-clutch modules, and each module exerts a force on a central cell body [36]. The CMS is governed by the same principles as the motor-clutch model with the addition of mass conservation and force balance between the cell body and modules. In addition to the eight motor-clutch module parameters, additional parameters are added to capture cell dynamics, presented in chapter 2 (Table S2.1) When clutch bonds break, the resulting force balance displaces the cell's center of mass, resulting in cell movement. The model predicts biphasic traction force, F-actin retrograde flow and migration rate as a function of substrate stiffness, each of which were experimentally validated using the U251 human glioma cell line cultured on polyacrylamide gels coated with type I collagen [36]. Furthermore, the CMS was used to investigate the effect of changes in adhesion molecule expression and migration in complex environments [37–39]

1.6. CD44: Structure and function

CD44 is a cell surface glycoprotein which serves as the major receptor for hyaluronic acid (HA) [40–42]. CD44 regulates many biological processes and it is considered a cancer stem cell and an epithelial-to-mesenchymal transition (EMT) marker [43–45]. CD44 has been linked to several different cancer types, such as breast, lung, prostate, and brain, and has been reported to contribute to cancer

invasiveness [46–48]. The structure of CD44 consists of four main structural domains: an N-terminal extracellular domain, stem region, a transmembrane domain, and a C-terminal cytoplasmic tail [49]. The N-terminal extracellular domain serves as a binding site for various ligands including the extracellular matrix glycosaminoglycan hyaluronic acid (HA), a relatively abundant extracellular matrix component in brain compared to collagen and fibronectin [40]. Using protein truncation, and site directed mutagenesis, Peach *et al.* identified two regions within the N-terminal domain, which contain residues important for CD44-HA binding [42]. Furthermore, using Surface Plasmon Resonance (SPR), the dissociation constant of CD44-HA interaction was estimated at ~20μM [50]. Moreover, the stem region of CD44 contains proteolytic cleavage sites for different enzymes, such as ADAM10, ADAM-17 and MT1-MMP [51,52]. These proteolytic cleavage sites provide an extra level of regulation of CD44 expression on cell surface. Lastly the C-terminal tail contains many phosphorylation sites and binds to intracellular adapter proteins (ankryin and ERM; ezrin/radixin/moesin proteins) that mediate CD44 mechanical coupling to the actin cytoskeleton [53–56].

Due to its interaction with hyaluronic acid and ability to link to the cytoskeleton via adapter proteins, CD44 is hypothesized to mediate cell adhesion and migration. Using hyaluronic acid-based hydrogels, CD44 was shown to support cell adhesion and migration [57,58]. Also, via its interaction with the ECM and actin cytoskeleton, CD44 has been shown to act as a transmembrane “picket” to limit transmembrane proteins diffusion during the process of phagocytosis [59].

1.7 CD44 in Glioblastoma

In glioblastoma, CD44 expression is associated with worse survival outcome and correlate with human mesenchymal subtype [14,15,17,60,61]. CD44 has been reported to promote GBM aggressiveness by increasing glioma cell proliferation, migration and resistance to therapy [62]. In earlier work from our group, CD44 expression was shown to be a prognostic marker with a biphasic dependence: better outcomes are observed at both lower and higher levels of CD44 while poorer outcomes are observed at intermediate levels, an example of optimality and the 'goldilocks' phenomenon [35]. In animal models, CD44 expression has further been shown to correlate with glioma cell migration in a biphasic relationship with a peak migration rate at intermediate expression level, which also correlated with the minimum in survival in both the animal model and human GBM [35]. This work hypothesizes the CD44 regulate glioma cell migration and disease progression via its function as an adhesion molecule. Overall, these findings raise the question of CD44 role within glioblastoma molecular subtypes and its function as an adhesion molecule mediating cell migration.

1.8 Thesis statement

In this dissertation, I sought to understand the mechanism driving glioma cell migration and progression. I hypothesize that a key mechanistic difference between GBM molecular subtypes is that proneural cells are slow migrating and mesenchymal cells are fast migrating (Chapter 2). In addition, I hypothesize that CD44 is able to function as an adhesion molecule to mediate cell migration and force transmission (Chapter 3). The ability of CD44 to mediate cell migration

could, therefore, explain the hypothesized difference in glioma cell migration within molecular subtype and provide a pathway to target glioma cell invasion.

Chapter 2

Differential migration mechanics and immune responses of glioblastoma subtypes

*Chapter 2 contains work by **Shamsan, G.A**., et al., In preparation*

Authors: Ghaidan A. Shamsan[1], Chao J. Liu[1], Brooke C. Braman[1], Susan K. Rathe[2], Aaron L. Sarver[2,3], Nima Ghaderi[1], Mariah M. McMahon[1], Rebecca L. Klank[1], Barbara R. Tschida[2], Joey McFarren[2], Pamela C. Rosato[4], David Masopust[4], Jann N. Sarkaria[5], H. Brent Clark[6], Steven S. Rosenfeld[7+], David A. Largaespada[2,8+], David J. Odde[9+]

Affiliations:
[1] Department of Biomedical Engineering, University of Minnesota, Minneapolis, MN 55455
[2] Masonic Cancer Center, University of Minnesota, Minneapolis, MN 55455
[3] Institute for Health Informatics, University of Minnesota, Minneapolis, MN 55455
[4] Department of Microbiology and Immunology, Center for Immunology, University of Minnesota, Minneapolis, MN, 55455
[5] Department of Radiation Oncology, Mayo Clinic, Rochester, MN, 55902
[6] Laboratory Medicine and Pathology, University of Minnesota, Minneapolis, MN 55455
[7] Department of Molecular Pharmacology and Experimental Therapeutics, Mayo Clinic, Jacksonville, FL 32224
[8] Department of Pediatrics, University of Minnesota, Minneapolis, MN 55455
[9] Department of Biomedical Engineering, University of Minnesota, Minneapolis, MN 55455, USA. Electronic address: oddex002@umn.edu.
[+] co-senior authors

Authors contribution:
GAS, RLK, BRT, SSR, DAL and DJO contributed to study initiation, conception and design.
GAS, CJL, BCB and DJO contributed to writing the manuscript
GAS, BCB and JMF contributed to developing mouse tumors
GAS, SKR and ALS contributed to the analysis of transcriptomic data.
GAS ran and analyzed the cell migration simulations
GAS, MMM and CJL contributed to the acquisition and analysis of glioma cell migration
GAS established tumor lines and performed traction force measurements
GAS, BCB and HBC contributed to imaging and analysis of histological sections
NG, PCR, DM and DJO contributed to the design and implementation of the Brownian Dynamics Tumor Simulator

2.1 Summary

Glioblastoma remains a deadly cancer characterized by diffuse infiltration of tumor cells into the brain. Transcriptomic analyses have revealed distinct molecular subtypes, including proneural and mesenchymal, but mechanistic differences are not clear. Here, we show that, as predicted by the motor-clutch model for cell migration, both mouse and human patient mesenchymal glioma cells are more spread, generate larger traction forces, and migrate faster in brain tissue compared to proneural cells. Despite their fast migration and comparable proliferation rate *in vitro*, mesenchymal mice live longer than proneural mice, which was due to an immune response in the mesenchymal mice that included T cell-mediated killing of cancer cells, similar to human tumors. Thus, mesenchymal tumors have aggressive migration, but are immunologically 'hot' which suppresses net proliferation. These two features counteract each other and may explain the lack of a strong survival difference between subtypes clinically, while also opening up new opportunities for subtype-specific therapies, especially those subtypes linked to an epithelial-to-mesenchymal transition (EMT).

2.2 Introduction

Glioblastoma (GBM: WHO grade IV primary brain tumor) progression can be characterized in terms of tumor growth and spreading, two key parameters which are influenced by many of the hallmarks of cancer [63]. In GBM, tumor spreading is driven by tumor cells' ability to infiltrate healthy brain parenchyma, which prevents complete surgical resection and results in tumor recurrence [64–66].

Molecular and genetic analyses of human GBM have identified at least three distinct molecular subtypes: proneural, classical, and mesenchymal [14–16]. These subtypes were shown to strongly correlate with specific genetic alterations (Mesenchymal: *NF1*; Classical: *EGFRvIII*; Proneural: *PDGFRA*) and cellular developmental states [15–18]. Despite accumulating evidence of distinct transcriptomic and genetic signatures, the characteristic mechanistic differences between such signatures, if any, have not been identified. As a result, it remains unclear how knowledge of the different subtypes should inform clinical decisions.

One intriguing correlate of subtype is the level of CD44 expression, a cell surface protein expressed on tumor and immune cells, which is known to play a role in cancer progression across a variety of cancers including GBM [16,17,35,47,48,60,62,67–69]. In GBM, we previously showed that CD44 expression is a prognostic marker with a biphasic dependence: better outcomes are observed at both lower and higher levels of CD44 while poorer outcomes are observed at intermediate levels, an example of optimality and the 'goldilocks' phenomenon [35]. In animal models, CD44 expression has further been shown to correlate with glioma cell migration in a biphasic relationship with a peak migration rate at intermediate expression level, which also correlated with the minimum in survival in both the animal model and human GBM [35]. In addition, *CD44* transcript levels are shown to vary across GBM molecular subtypes with elevated expression in mesenchymal tumors [14,15,60]. *CD44* expression in the mesenchymal tumors is, on average, closer to the *CD44* level that corresponds to the minimum in patient survival than the proneural subtype [35]. This suggests the possibility that

mesenchymal cells have a near-optimal level of CD44 adhesion molecules to serve as molecular “clutches” that resist myosin II motor forces, allowing them to migrate faster than proneural cells which on average have a lower, suboptimal level of CD44 clutches (see Figure 2B and 4E in Klank *et al.,* 2017). This could then explain the slightly worse outcomes for mesenchymal patients and higher cell migration and invasion [16,70]. In addition, it would predict that mesenchymal cells would be more spread, more polarized, and generate more traction force as they migrate. More generally, lower CD44 is indicative of an epithelial state and higher CD44 indicative of a mesenchymal state [44,45], and so an increase in myosin motors and adhesions, either integrin- or CD44-mediated, may be driving the epithelial-to-mesenchymal transition (EMT) in a variety of cancers such as breast cancer [31]

Based on these previous results, here we tested the hypothesis that a key mechanistic difference between GBM molecular subtypes is that proneural cells are slow migrating and mesenchymal cells are fast migrating. To address this question, we generated animal models recapitulating the transcriptomic signatures of human mesenchymal and proneural GBM in an immune competent background using perturbations of known GBM oncogenic pathways. Specifically, mesenchymal and proneural-like tumors were driven by SV40-LgT antigen, to mimic common inhibition of p53 and Rb signaling found in GBM [13,71], in combination with either NRASG12V (NRAS) or PDGFβ (PDGF), respectively, which resulted in mesenchymal and proneural transcriptomic features with only a single genetic change required to switch subtypes in a wild type mouse

background. As predicted, *CD44* expression was higher in NRAS-driven tumors and, consistent with our simulation predictions, *ex vivo* brain slice live imaging showed NRAS tumor cells migrate faster than PDGF tumor cells, and exhibit greater spreading, polarization, and force generation as well. Despite increased migration, the NRAS cohort had better survival than PDGF which was attributed to enhanced antitumoral immune response in NRAS tumors, consistent with increased immune cell infiltration in human mesenchymal GBM [16,72]. Overall our work identified a clinically actionable difference in migration mechanics between GBM subtypes and establishes an integrated biophysical modeling and experimental approach to mechanically parameterize and simulate distinct molecular subtypes in preclinical models of cancer.

2.3 Results

2.3.1 Genetically induced high-grade glioma mouse models recapitulate the transcriptomic signatures of mesenchymal and proneural GBM

To characterize the mechanics of GBM subtypes, we utilized the *Sleeping Beauty* (SB) transposon-based gene transfer system to induce high grade gliomas in immunocompetent FVB-strain mice [35,73–76]. Constructs of SB plasmids encoding oncogenic drivers (SV40-LgTA+NRASG12V or SV40-LgTA+PDGFB; here termed NRAS and PDGF, respectively) were used to model mesenchymal and proneural GBM tumors, respectively (Figure 2.1A). DNA plasmids encoding firefly luciferase and green fluorescent protein (GFP) were also injected to allow for confirming successful gene transfer, detecting tumor development and

monitoring tumor growth using bioluminescence imaging (BLI) and single cell tracking using fluorescence microscopy. Similar to human GBM, histological sections from these tumors exhibited highly mitotic tumor cells, necrosis, anaplasia, and perivascular infiltration and proliferation, (Figure 2.1B).

To assess whether the NRAS and PDGF tumors recapitulated the mesenchymal and proneural subtypes, respectively, we performed cross-species transcriptomic analysis using bulk RNA sequencing data from mouse and human tumors. Bulk RNA sequencing was performed on tumor tissues from both cohorts and on normal brain tissues (NBT) (NRAS N=4, PDGF N=4, and NBT N=3). IDHwt human GBM transcriptomic profiles were retrieved from Broad GDAC Firebrowse [77]. Unsupervised hierarchical clustering of the mouse dataset revealed clear differences between normal tissue and tumor tissue and between NRAS and PDGF tumors (Figure 2.S1A). Not surprisingly, gene ontology enrichment analysis, using EnrichR [78], showed an enrichment of cell cycle related processes in tumor tissue specific gene cluster (817 genes) (Figure 2.S1B) and neuronal processes in normal tissue cluster (1722 genes) (Figure 2.S1D). Interestingly, the NRAS-specific cluster (1327 genes) was enriched with cytokine-mediated signaling and inflammatory response processes (Figure 2.S1C).

To determine whether any variations observed between the two mouse cohorts were also present in human tumors, unsupervised hierarchical clustering was performed on both mouse and human tumor datasets and clusters were independently identified in both datasets. Three and 10 gene clusters were

identified in both mouse and human datasets, respectively, as shown in Figure 2.1C. We identified mouse cluster MC1 (n=1534 genes) as being significantly enriched in genes found in human cluster HC1 (n=1186 genes, $p < 1x10^{-15}$), MC2 (n=414 genes) is significantly enriched in genes found in HC2 (n=1098 genes, $p < 1x10^{-15}$), and MC3 (n=232 genes) is significantly enriched in genes enriched in HC4 (n=432, $p < 1x10^{-15}$). These results show that conserved transcriptomic patterns exist between the mouse and human tumors.

To assess whether the transcriptional patterns present in the mouse tumor models represent previously described GBM subtypes, we compared the expression of identified mouse gene clusters within human GBM subtypes. We found that MC1, which is enriched in NRAS tumors, is significantly enriched in human mesenchymal GBM relative to proneural and classical GBMs (Figure 2.1D). In contrast, MC3, which is enriched in PDGF tumors, is significantly enriched in proneural GBM relative to mesenchymal and classical GBMs (Figure 2.1D). Furthermore, we found the expression of known mesenchymal and proneural genes and gene signatures are relatively elevated in NRAS and PDGF tumors, respectively (Figure 2.1E, 2.1F and 2.S2). These results demonstrate that NRAS and PDGF tumors transcriptionally resemble mesenchymal and proneural GBMs, respectively.

2.3.2 Motor-clutch modeling of cell migration predicts NRAS/Mesenchymal tumor cells will migrate faster, be more spread, and generate more force than PDGF/Proneural tumor cells

To examine tumor cell migration, we used our cell migration simulator [35,36] to predict migration phenotypes in response to gene expression changes. The cell migration simulator is based on the motor-clutch model which incorporates actin-based protrusion dynamics, mass conservation, and force balances to reproduce cell polarization and random motility in 1D and 2D compliant microenvironments [24,33–39,79]. The number of adhesion/clutches and motors are key determinants of cell migration, with a relative balance being essential for efficient migration [22,34,36]. Using a set of 54 cell migration genes expressed in the human U251 GBM cell line [36], NRAS tumors significantly upregulate transcription of adhesion and adapter genes (Figure 2.S3A). A similar set of genes was also significantly upregulated in MES relative to PN GBM (Figure 2.S3B). Both NRAS and MES tumors upregulated *CD44* and its cognate adhesion adapter gene moesin (*MSN*), which mechanically links the CD44 cytoplasmic tail to F-actin [43,47,54,56,59,80,81]. Notably, the levels of myosin motor genes were not differentially expressed in the mouse dataset, while, in the human dataset, *MYH9* and *MYO1C* were modestly upregulated in MES tumors but to a lesser degree than adhesion molecules (Figure 2.S3B). These results suggest NRAS/Mesenchymal tumor cells have a higher number of adhesion/clutches than PDGF/Proneural tumor cells and little to no change in the number of motors.

Based on these results, we simulated the effect of CD44 expression level on cell migration by simply adjusting the number of adhesion bonds (number of clutches, N_c) in the model with simulated PDGF/Proneural cells having low clutches relative to motors (low adhesion) and simulated NRAS/Mesenchymal

cells having a medium level of clutches that balanced the number of motors (optimal adhesion), Figure 2.2A [35,36]. Our simulations show that lowering the number of adhesions, representing the PDGF/Proneural case, results in reduced cell migration, force transmission, cell spread area, and cell polarization due to an insufficient number of clutches relative to the number of motors, as shown in Figure 2.2. In the case where the number of clutches and motors are balanced, representing the NRAS/Mesenchymal case, where the number of adhesions is increased while holding the number of motors constant, simulated cells recover their ability to migrate, transmit forces, spread, and polarize across a range of substrate stiffnesses. Consequently, simulation results predict that NRAS/Mesenchymal tumor cells will migrate faster than PDGF/Proneural tumor cells due to increase of adhesion (i.e. CD44) expression in NRAS/Mesenchymal tumors and not due to small difference in molecular motor expression, (Figure 2.S3A and 2.S3B). In addition, due to their higher number of clutches and balanced motor-clutch ratio, NRAS/Mesenchymal tumor cells are predicted to generate higher force, have larger spread area, and be more polarized.

2.3.3 NRAS/Mesenchymal tumor cells migrate faster than PDGF/Proneural tumor cells in brain tissue

To test our model prediction that NRAS/Mesenchymal cells migrate faster than PDGF/Proneural cells, we performed live cell imaging on tumor bearing mouse brain slices using confocal microscopy. Time-lapse images of GFP-positive tumor cells were used to track single cell migration and generate single cell trajectories. As shown in Figure 2.3A and 2.3B, NRAS/Mesenchymal tumor

cells appeared qualitatively to move farther, have larger spread area, and polarize to a greater extent than PDGF/Proneural tumor cells. Quantitative analysis of single cell trajectories confirmed that NRAS/Mesenchymal tumor cells have a higher random motility coefficient than PDGF/Proneural tumor cells as shown in Figure 2.3C and 2.S4A. In addition, morphological analysis of tumor cells revealed cell spread area and cell aspect ratio (i.e. polarization) are also higher in NRAS/Mesenchymal tumor cells than PDGF/Proneural tumor cells (Figure 2.3D, 2.3E, 2.S4B and 2.S4C). As predicted by our modeling, and the hypothesis that NRAS/Mesenchymal has balanced motors and clutches while PDGF/Proneural lacks sufficient clutches, we find NRAS/Mesenchymal cells migrate faster, are more spread, and are more polarized than PDGF/Proneural cells.

2.3.4 Migration phenotype is species and tumor microenvironment independent

To determine whether migration phenotype is cancer cell intrinsic as predicted by our modeling and not due to microenvironment differences, we generated three primary mouse lines grown as neurospheres from each cohort to investigate their migration phenotype outside their tumor microenvironment. Organotypic mouse brain slice culture was used to image tumor cell migration in healthy mouse brain slices [37]. Dissociated mouse tumor cells were plated and allowed to invade and migrate in healthy mouse brain slices. Figure 2.4A shows representative fluorescence images of primary isolated cells in organotypic slice culture. Time-lapse imaging was used to track single cells and quantify their

migration rates. Consistent with the *ex vivo* migration in intact tumor-bearing brain slices, random motility coefficient in normal mouse brain tissue is higher for primary NRAS/Mesenchymal tumor cells than primary PDGF/Proneural tumor cells (Figure 2.4B and 2.S4D). Cell spread area is also higher in primary NRAS/Mesenchymal tumor cells than PDGF/Proneural (Figure 2.4C and 2.S4E). Furthermore, cell aspect ratio was higher in NRAS/Mesenchymal tumor cells than PDGF/Proneural but did not reach statistical significance (Figure 2.4D and 2.S4F).

To assess the relevance of these results to human GBM, we tested the migration phenotype of six patient-derived xenograft (PDX) lines (three mesenchymal and three proneural) using the organotypic mouse brain slice culture. Figure 2.4E shows representative fluorescence images of PDX cells in organotypic slice culture. We found mesenchymal PDX cells migrate faster than proneural PDX cells, (Figure 2.4F and 2.S4G). In addition, similar to our mouse models, mesenchymal PDX cells have larger cell spread area and aspect ratio relative to proneural PDX cells (Figure 2.4G, 2.S4H, 2.4H and 2.S4I).

2.3.5 Traction strain energy is larger for NRAS/Mesenchymal cells than for PDGF/Proneural cells, consistent with model predictions

In addition to migration rate and cell morphology, cell migration simulations predict NRAS/Mesenchymal tumor cells would have increased force generation as a result of higher number of clutches resulting in balanced myosin motors and clutches, relative to PDGF/Proneural tumor cells which would have insufficient clutches relative motors (Figure 2.2D). Using the primary isolated

mouse lines, traction force microscopy was used to measured traction strain energy generated by tumor cells on polyacrylamide hydrogels coated with type-I collagen [36,82]. Consistent with model predictions, NRAS/Mesenchymal tumor cells generate higher traction strain energy than PDGF/Proneural tumor cells across different substrate Young's moduli (Figure 2.5A and 2.5B). Cell spread area is also higher in NRAS/Mesenchymal than PDGF/Proneural on polyacrylamide hydrogels, Figure 2.5C. In addition, NRAS/Mesenchymal cells exhibit stiffness sensitive cell spreading; cells on stiff substrate (4.6 and 9.3 kPa) were more spread than on soft substrate (0.7kPa), $p < 0.00001$, (Figure 2.5C). Furthermore, we also examined force generation of mesenchymal and proneural PDX cells in mouse brain slices. Qualitative analysis of vasculature deformation is consistent with the model prediction that mesenchymal PDX cells generate larger deformations relative to proneural PDX cells, as shown in Figure 2.5D, 2.5E.

2.3.6 Mesenchymal mice have better survival and slower tumor growth rate

Since NRAS/Mesenchymal cells have nearly optimal CD44 expression, and therefore higher motility compared to PDGF/Proneural cells which have a suboptimal low level of CD44 expression [35], we asked whether the migration speed differences correlate with disease progression and survival. Specifically, based on the faster migration in the NRAS/Mesenchymal cohort, we expected that these mice would progress faster and die sooner than PDGF/Proneural mice. To test this hypothesis, we measured survival times of tumor bearing mice

and found that, opposite to our expectation, the NRAS/Mesenchymal cohort had better median survival than PDGF/Proneural cohort (NRAS N=21, PDGF N=24, 65 days vs. 35 days, log-rank test $p<0.0001$; Figure 2.6A). To explain the difference in survival, we quantified *in vivo* tumor growth using bioluminescence imaging (BLI) of tumor-bearing mice. Consistent with their shorter survival, we found PDGF tumors grew twice as fast as NRAS tumors (Slopes: 0.127±0.01191 vs. 0.0716±0.00343 $p <0.001$, Figure 2.6B and 2.6C). Using mouse tumor neurospheres, we quantified mouse primary tumor cell line proliferation rates *in vitro* and found no significant difference between NRAS/Mesenchymal and PDGF/Proneural cells (Figure 2.6D). These results imply that an additional factor, besides proliferation or migration, enables the NRAS/Mesenchymal mice to live longer and their tumors to grow slower *in vivo* than PDGF/Proneural mice.

2.3.7 Mesenchymal mice have increased immune response relative to PDGF/Proneural mice

Because mesenchymal GBMs are known to be immunologically “hot” – which presumably confers a survival benefit due to an antitumoral immune response- relative to immunologically “cold” proneural GBMs [16,17,72], we assessed the extent to which mouse NRAS/Mesenchymal tumors induce an immunological response relative to PDGF/Proneural tumors and normal brain tissues. Using our mouse transcriptomic dataset and previously published GBM immune gene sets [72], NRAS/Mesenchymal tumors were found to have increased expression of both immune activators and suppressors gene signatures similar to human mesenchymal GBM [72], as shown in Figure 2.7A and 2.7B. Specifically,

expression of immune cell marker genes such as *Aif1*, *Itgam* (microglia/macrophages) and *Cd3* (T cells) are elevated in NRAS/Mesenchymal tumors relative to PDGF/Proneural tumors (Figure 2.7C upper panel) and in mesenchymal GBMs relative to proneural and classical GBMs (Figure 2.7C lower panel). Consistent with the transcriptomic findings, IHC staining of NRAS/Mesenchymal and PDGF/Proneural tumor sections revealed significant levels of immune cell infiltration, including both microglia/macrophages and T-lymphocytes, in NRAS/Mesenchymal but much less so in PDGF/proneural tumors (Figure 2.7D). Furthermore, increased immune infiltration and activity in NRAS/Mesenchymal tumors was accompanied by increased cell killing as measured by granzyme B and cleaved caspase-3 staining (Figure 2.7D). Image clustering analysis was used to quantify CD3, IBA1, granzyme B, and cleaved caspase-3 staining, and statistically significant differences were observed between NRAS/Mesenchymal and PDGF/Proneural cohorts, Figure 2.7E-H. This anti-tumor response was also evident in the three instances where NRAS mice developed tumors and tumor regression was observed (Figure 2.S5). Despite the anti-tumor immune response observed in NRAS/Mesenchymal tumors, transcriptomic analysis also revealed elevated relative expression of immune checkpoint genes including *PDL1*, *CTLA4*, and *CD200R1* (Figure 2.S6). Thus, the NRAS/mesenchymal tumors, like human mesenchymal GBMs, are immunologically “hot” with evidence of both immune activation and immune suppression, as well as evidence of cell killing. Altogether, the enhanced immune cell-associated tumor cell killing provides a mechanism by which survival is

extended in NRAS/Mesenchymal tumors despite their enhanced migration speeds relative to PDGF/Proneural tumors.

2.3.8 Brownian dynamics simulations explain NRAS/Mesenchymal and PDGF/Proneural tumor progression

To quantitatively describe the interplay between tumor cell migration and proliferation and anti-tumoral immune response in tumor growth, we developed a three-dimensional (3D) Brownian dynamics tumor simulator (BDTS) based on our original 1D Brownian dynamics simulator [83,84]. The simulator takes into account anti-tumoral immune cells that infiltrate tissue, migrate, proliferate, encounter cancer cells, deliver cytotoxic agents, dissociate from cancer cells, undergo exhaustion, and, eventually, undergo apoptosis (or egress to lymphatics) as shown in Figure 2.8A. At the same time, cancer cells migrate, proliferate and undergo CTL-mediated death in the presence of anti-tumoral immune cells in the case NRAS/Mesenchymal tumors. In the case of PDGF/Proneural tumors, no anti-tumoral immune cells were simulated. Figure 2.8B shows simulation output at day 0 and day 16, which showed the observed behavior of overall faster growth of PDGF/Proneural tumors. In the NRAS/Mesenchymal tumor simulations, cancer cells appear more dispersed, whereas, in PDGF/Proneural simulations, cancer cells are less dispersed. Simulated tumor growths were plotted in Figure 2.8C. Using the parameters in Table 2.S1, including the experimentally observed single cell migration speeds and neurosphere proliferation rates, simulated tumors qualitatively recapitulate

the *in vivo* growth profile of NRAS/Mesenchymal and PDGF/Proneural tumors without parameter adjustment (Figure 2.8C).

2.4 Discussion

Understanding glioma progression and the mechanism driving glioma cell migration is critical for the design of effective therapies. Here we developed high-grade glioma mouse models which capture the transcriptomic and the immune microenvironment changes associated with human proneural and mesenchymal GBMs. Using the mouse models and patient-derived xenograft (PDX) lines, we defined a mechanistic difference in glioma cell migration which highlights a functional characteristic of GBM molecular subtypes. The migration difference was consistent with changes in cellular adhesion, notably CD44, but not molecular motors such as myosin II motors. This finding points toward an anti-migratory therapy approach targeted against cellular adhesion as opposed to myosin motors. With the failure of a phase III integrins inhibitor, Cilengitide, clinical trial in GBM [9], it is reasonable to conclude that integrins may not be the major adhesion molecules utilized by glioma cells to migrate but instead they could utilize CD44. While anti-CD44 therapies have not been tried in GBM, an anti-CD44 monoclonal antibody therapy (RO5429083, Roche, Basel, Switzerland) has been investigated in phase I trials in patients with solid tumors and with AML [85,86].

Furthermore, the upregulation of CD44 in mesenchymal tumors is supportive of the existing literature which defines CD44 as a marker of cancer

stem cell and epithelia-to-mesenchymal transition (EMT) [43–45]. During EMT, cancer cells take a more mesenchymal migratory phenotype to allow them to migrate through dense ECM and metastasize [87]. Our results associate enhanced migration in mesenchymal glioma cells with increased traction forces as a result of increased adhesion molecules expression 'clutches' including CD44. Similarly, in breast cancer cells, TGF-β-induced EMT is associated with increased traction forces and clutch number [31]. Interestingly, downregulation of NF1, a negative regulator of Ras, in epithelial breast cancer cells and Schwann cells also induces expression of transcription factors related to EMT [88]. Moreover, in our study, NRasG12V was used to mimic NF1 downregulation and inactivation in mesenchymal GBM [15,89]. Ras hyperactivation of MAPK pathway is required for EMT but not PI3K activation by Ras [90]. Altogether, our results implicate EMT in enhanced glioma cell migration and force transmission associated with increased molecular clutches through, and suggest upregulation of clutches, either integrins or CD44, as a conserved feature of EMT across a range of cancers.

Despite the faster migration of the NRAS/Mesenchymal cells, the anti-tumoral immune response within the NRAS/Mesenchymal mouse model is able to slow disease progression and improve survival despite enhanced migration relative to the PDGF/Proneural mouse model. Such an anti-tumor response could potentially be used to slow disease progression and improve clinical outcome for GBM patients. In both mouse and human GBM, mesenchymal tumors are immunologically 'hot' relative to the immunologically 'cold' proneural tumors [16,72]. Despite the presence of immune cells within mesenchymal tumors,

immune suppression leads to tumors ultimately prevailing against the anti-tumoral immune response. Based on these findings, we propose an immune checkpoint inhibition strategy, in combination with an anti-migratory therapy, targeting mesenchymal GBM but not proneural GBM. On the other hand, an immune stimulating strategy, e.g. oncolytic virus, to target proneural GBM but not mesenchymal GBM.

Our study utilizes an integrated, state of the art experimental approach to study GBM progression and model GBM molecular subtypes by switching a single oncogenic driver (NRASG12V→ PDGFB), in an immunocompetent background without the need for genetically engineered mouse strains or further breeding. Using live cell and brain slice imaging, we identify key mechanical differences between mesenchymal and proneural tumor cells, with mesenchymal cells being bigger, stronger, and faster. The functional differences were all predicted by a motor-clutch model for cell adhesion and migration where mesenchymal cells have an optimal level of CD44-mediated adhesion (clutches) relative to myosin motors, while proneural cells lack sufficient CD44 to match the myosin motor activity. Despite the faster migration, NRAS/Mesenchymal mice live longer, consistent with the presence of an anti-tumoral immune response that is lacking in PDGF/Proneural mice (Fig. 2.8D), dynamics that are readily captured computationally with little parameter adjustment using a 3-D Brownian dynamics tumor simulator (BDTS). Overall, this work establishes an integrated *in vivo* genetic and biophysical modeling framework to connect animal model and human transcriptionally-defined subtypes to fundamental mechanistic

understanding, which has the potential to enable a new modeling-centric approach to clinical translation with application in a wide range of cancers [91].

2.5 Materials and Methods

Generation of mouse tumor models

All animal studies were conducted according to guidelines approved by the Institutional Animal Care and Use Committee at the University of Minnesota. All animals were housed in a daily monitored animal facility. FVB strain of mice were used in this study. Malignant gliomas were induced in neonatal mice by DNA plasmids injection into the right lateral ventricle as described previously [73,74]. Briefly, neonatal mice were injected with 1 µg of plasmid DNA mixed with polyethyleneimine (jetPEI, Polyplus, Berkeley, CA), and 5% dextrose in a total volume of 2 µL at a rate of 0.7 µL/min. The following four plasmids were used (1:1:1:1) ratio: empty vector, pT2/C-Luc/PGK-SB100, pT/CMV-LgTAg-IRES-GFP, pT2/Cag-NrasV12 or pT2/Cag-mPDGF. Animals were monitored daily for morbidity.

Immunohistochemistry of mouse tumor sections

Formalin fixed and paraffin embedded (FFPE) mouse brain tissues were used to prepare 4 µm thick slides. FFPE tissue slides were stained with hematoxylin and eosin (H&E) or IHC using standard methods.

Quantification of IHC staining of mouse tumor sections

Immunohistochemistry data was quantified by counting the number of pixels in an image that were positively DAB stained. To avoid user bias and

subjective counting, k-means clustering was used to identify pixels representing areas of positive DAB, hematoxylin staining, and background. In this implementation, every pixel in an analyzed image is assigned to one of four clusters, each cluster representing a different component in the image: positive DAB-stained areas (brown), positive hematoxylin counter-stained areas (blue), unstained tissue (light blue), and background glass slide (beige). Digital images of equal sizes (2000x2000 pixels) of DAB stained and hematoxylin counterstained tumor samples were converted from RGB to the HSV color model.

Using a custom written MATLAB algorithm, user input is used to define areas representing the four components (positive DAB stain, hematoxylin counterstain, unstained tissue, and background glass slide). These points are used as the initial estimates for the centroid locations of each of the four clusters. The squared Euclidean distance between each pixel's HSV coordinates and the HSV coordinates of each cluster's centroid is computed. Each pixel is then assigned to the cluster with the minimum squared Euclidean distance to the cluster centroid. Cluster centroids are recalculated as the mean of the HSV coordinated of all current members. This process is iterated until the centroid of each cluster is stable. The number of pixels in the positive DAB-stained cluster is used to quantify percent positive pixels in Figure 2.7E-H.

Transcriptional profiling of mouse tumors

Mice were euthanized in a CO_2 chamber and perfused transcardially with isotonic saline. Mouse brains were extracted and GFP goggle (#FHS/EF-2G2;

BLS-ltd, Budapest, Hungary) was used to dissect GFP-positive tumor tissues from NRAS and PDGF mouse brains. Two matched normal brain tissues were collected from brain regions away from the tumor and an additional normal brain tissue sample was collected from a health FVB adult mouse. All samples were immediately placed in *RNALater* solution (Sigma, St. Louis, MO) for 24 hours then flash frozen in liquid nitrogen and stored in -80 °C for downstream processing. RNA extraction and sequencing were performed at the University of Minnesota Genomics Center (UMGC, Minneapolis, MN). RNA was extracted using *RNAeasy* Plus Universal Mini kit (Qiagen, Venlo, Netherlands) and libraries were prepared using *TruSeq* stranded mRNA (Illumina, San Diego, CA).

Next-generation sequencing was performed on the prepared RNA libraries using an Illumina HiSeq 2500 device in high output mode and generated 51 bp reads with an approximate depth of 20 million paired reads per sample. Mapping and expression calculations were generated using the rnaseq-pipeline of Gopher-pipelines (https://bitbucket.org/jgarbe/gopher-pipelines), which executed TopHat2 [92] and Cuffnorm [93] using the UCSC mm10 version of the mouse reference genome. Fastq files and the Cuffnorm output were deposited at Gene Expression Omnibus (GSE161154).

Human GBM transcriptomic data

UNC RNASeqV2 level 3 expression (normalized RSEM) profiles of 171 samples (TCGA-GBM) were retrieved from Broad GDAC Firebrowse [77]. IDH status and subtype information were added to each sample based on the *Wang*

et al. classification [16]. For downstream analysis, 147 IDHwt samples were used (57 Classical; 52 Mesenchymal; 38 Proneural).

Clustering analysis of mouse and human expression profiles

To analyze the transcriptional profiles of mouse and human datasets, a value of 0.1 was added to all FPKM and RSEM values to minimize the impact of inaccurate low values [94]. The expression data was log transformed and mean centered and transcripts with Standard Deviation > 1 were clustered using average linkage hierarchical clustering in MATLAB. Pearson correlation was used as the similarity metric. A custom written MATLAB script was used to systematically identify transcriptional clusters within each dataset. In mouse dataset, a correlation greater than 0.5 and > 100 transcripts were used to identify gene clusters. Whereas, in human dataset, a correlation greater than 0.2 and >100 transcripts were used. Fisher's exact test was used to compare cluster memberships in Figure 2.1C.

To quantify the relative expression of gene clusters in Figure 2.1D and subtype gene signature set in Figure 2.S2C and 2.S2D, the average relative expression of each gene set was computed for all samples. The average relative expression from each sample was plotted and used to calculate mean relative expression within each mouse cohort and within human GBM molecular subtype.

Generation of mouse primary tumor lines

For each line, a tumor bearing mouse was euthanized and transcardially perfused with isotonic saline. Tumor tissue was collected and minced with a

scalpel. Minced tumor fragments were incubated with PBS for 15 min at 37 °C. Tumor fragments were further dissociated by mixing them up and down using a 1000 µl micropipette. Finally, tumor suspension was passed through a 40 µm sterile cell strainer (Thermo Fischer Scientific, Waltham, MA) and filtrate was spun down and plated on a Matrigel (354230; Corning, Corning, NY) coated T-75 flasks (Corning, Corning, NY) using NSC media which consisted of DMEM/F12 (Gibco 11320033; Thermo Fischer Scientific, Waltham, MA) with 1X B-27 supplement (Gibco 12587010, Thermo Fischer Scientific, Waltham, MA) and 1X penicillin/streptomycin (Corning, Corning, NY). Twenty ng/ml EGF (PeproTech, Rocky Hill, NJ) and FGF (PeproTech, Rocky Hill, NJ) were added to the cell culture media every 2-3 days. Cells were cultured in a 37 °C 5% CO_2 incubator. Once a confluent layer was achieved, cells were detached using 0.25% Trypsin EDTA (Corning, Corning, NY) and frozen down for later use.

Once tumor lines were established, cells were grown as neurospheres using NSC media and Ultra-Low Attachment 6-well plates (Corning, Corning, NY). Neurospheres were dissociated using accutase (Innovative Cell Technologies, San Diego, CA). In total, six different mouse primary tumor lines were established: three NRAS and three PDGF.

Patient-derived xenograft (PDX) cell line culture

The patient-derived xenograft (PDX) cell lines were taken from the Mayo Clinic GBM PDX collection (managed by Dr. Jann Sarkaria, Mayo Clinic, Rochester, MN). Three mesenchymal PDX lines (GBM 16, 39 and 44) and three

proneural PDX lines (GBM 64, 80 and 85) were selected to study their migration in organotypic mouse brain slice. Cells were cultured on Matrigel (354230; Corning, Corning, NY) coated tissue culture flasks in a 37 °C 5% CO_2 incubator. NSC media was used to culture PDX cell lines and 20 ng/ml EGF and FGF were added to the cell culture media every 2-3 days.

Ex vivo confocal imaging of tumor-bearing brain slices

Tumor-bearing mice were sacrificed when bioluminescence signals were around 5×10^7 radiance (p/sec/cm^2/sr). Mice were euthanized in a CO_2 chamber and perfused transcardially with isotonic saline. Mouse brains were extracted and kept in chilled artificial cerebrospinal fluid (124 mM NaCl, 2.5 mM KCl, 2.0 mM $MgSO_4$,1.25 mM KH_2PO_4, 26 mM $NaHCO_3$, 10 mM glucose). Coronal brain slices of thickness 300 µm were prepared using a vibratome (Leica Biosystems, Buffalo Grove, IL). Only one slice was used for live-cell imaging. Isolectin GS-IB4 (Alexa Fluor 568; Molecular Probes, Eugene, OR), which labels endothelial cells, was used to label the vasculature.

Before imaging, the slice was washed and transferred into a No. 0 glass bottom 35 mm culture dish (P35G-0-20-C; MatTek, Ashland, MA). A tissue culture anchor (SHD 42-15; Warner Instruments, Hamden, CT) was placed on top of the slice to prevent movement during imaging. The slice was then imaged on a Zeiss LSM 7 Live swept-field laser confocal microscope (Zeiss, Oberkochen, Germany) at 15 minutes intervals for up to 20 hours in humidified 5% CO_2 air. Images were collected with a 20x Plan-ApoChromat, 0.8 NA objective lens. The number of Z stacks of several regions of interest was

adjusted to ensure that the data acquisition was completed in under 15 minutes (10-20 planes with 10 µm z-step was typically used). Maximum intensity projections from multiple Z stacks were used to generate 2D images for quantitative morphological and trajectory analysis. Images were registered by an affine transformation using ImageJ StackReg plug-in (École Polytechnique Fédérale De Lausanne) to account for stage drift and tissue relaxation during time-lapse imaging.

Live-cell imaging of tumor cells in organotypic brain-slice culture

Healthy mouse brain slices were prepared using the same method as tumor-bearing brain slices above. For experiments using GFP-positive mouse primary tumor lines, neurospheres were dissociated using accutase (Innovative Cell Technologies, San Diego, CA). After creating a single cell suspension, 300,000 cells in 3 mL of media were plated onto the brain slice. The cells were co-cultured with the brain slice for 4 hours at 37 °C and 5% CO_2 before imaging to promote cell infiltration into the brain slice. Phenol-free NSC media +2% FBS (Gibco, Thermo Fischer Scientific, Waltham, MA) was used. Isolectin GS-IB4 (Alexa Fluor 568; Molecular Probes, Eugene, OR) was also added to the culture to label the vasculature. The slices were washed several times using cell culture media and transferred into a No. 0 glass bottom 6-well plate (P06G-0-20-F; MatTek, Ashland, MA). The slices were imaged on a Zeiss LSM 7 Live swept-field laser confocal microscope at 15 minutes intervals for 16 hours in humidified 5% CO_2 air. Images were collected with a 10x Plan-ApoChromat, 0.45 NA objective lens. Five Z stacks were acquired (10 µm z-step). Maximum intensity

projections from multiple Z stacks were used to generate 2D images for quantitative morphological and trajectory analysis.

For PDX cells, 500,000 – 800,000 cells were stained using DiO membrane dye (V22886; Thermo Fisher Scientific, Waltham, MA) for 5 minutes and then washed twice before plating onto the brain slice inside a 35mm tissue culture dish. Similar to mouse primary cells, PDX cells were co-cultured with the brain slice for 4 hours before imaging to promote cell infiltration into the brain slice. Also, Isolectin GS-IB4 (Alexa Fluor 568; Molecular Probes, Eugene, OR) was used to label the vasculature. Phenol-free DMEM (Gibco 21063029; Thermo Fisher Scientific, Waltham, MA) was used with PDX cells in brain slices. The slice was then imaged on a Zeiss LSM 7 Live swept-field laser confocal microscope using a 20x Plan-ApoChromat, 0.8 NA objective lens. The number of z-stacks was adjusted to ensure that the data acquisition of the whole slice was completed under 15 min (six to eight planes with 10 µm separation was typically used). The Z stacks were then imaged every 15 min for up to 16 h at 37 °C in a humidified.

For both mouse primary tumor cells and PDX cells, maximum intensity projections from multiple Z stacks were used to generate 2D images for quantitative morphological and trajectory analysis. Images were registered by an affine transformation using ImageJ StackReg plug-in (École Polytechnique Fédérale De Lausanne) to account for stage drift and tissue relaxation during time-lapse imaging.

Single cell tracking and morphology analysis

Single cell migration was tracked as previously described using a custom-written image segmentation algorithm in MATLAB [35,36]. Using cell centroid coordinates, the mean squared displacement (MSD) of the cell trajectories over time was calculated using the time interval overlap method [95]. To quantify the dispersion of cells, the MSD over time was used to calculate the random motility coefficient μ according to the equation (MSD(t)=4μt; assuming 2-D geometry). Using segmented cell regions, cell area and cell aspect ratio, defined as the ratio between the major and minor axis length of a fitted ellipse, were measured for each individual tracked cell. Distributions of random motility coefficients, cell area and cell aspect ratio for the different conditions were compared using the Kruskal-Wallis test, which is a non-parametric rank-based test.

Bioluminescence imaging and analysis

Animals were monitored for tumor development and progression using noninvasive bioluminescence imaging. Oncogene-injected animals were injected intraperitoneally with 100 μl of 28.5 mg/ml luciferin (GoldBio, St. Louis, MO) prior to imaging. Mice were then anesthetized using 3% isofluorane and imaged on an IVIS50 or IVIS100 instrument (Xenogen, Alameda, CA). Images were acquired ten minutes after injection with five minutes exposure time (Xenogen LivingImage Software, Alameda, CA). To avoid saturation, exposure time was reduced appropriately in fully grown tumors and accounted for in the analysis. BL images were processed using a custom written MATLAB algorithm where background signal was subtracted and pixels away from the tumor were set to zero. BL signal

from each animal was then normalized to the initial time point when tumor was first detected.

Quantification of proliferation of mouse primary tumor line

To measure proliferation rate, 200,000 cells from each line were plated into an ultra-low adhesion 6-well plate and grown as neurospheres. Growth factors were added every 2-3 days. At day six, neurospheres were dissociated and cells counted. After counting, the remaining cells were replated and resumed growing as neurospheres. Cells were also counted and replated at day nine and day 13. Experiment was repeated three times using each of five mouse primary tumor lines (three NRAS and two PDGF tumor lines). For each replicate, the average cell count for each cohort was calculated using the cell count from the different corresponding tumor lines.

Traction force measurements

Traction force measurements of mouse primary tumor lines were performed using traction force microscopy on polyacrylamide gels embedded with 0.2 μm crimson fluorescent beads (Thermo Fischer Scientific, Waltham, MA) and coated with Type-I Collagen (Corning, Corning, NY). Collagen coated polyacrylamide gels of varying Young's modulus were prepared as previously described [36,96]. Briefly, 0.7, 4.6, and 9.3 kPa polyacrylamide polymer mixture with fluorescent beads were cast onto a No. 0 glass bottom dish then coated with Type-I Collagen using Sulfo-SANPAH (Thermo Fischer Scientific, Waltham, MA).

Mouse primary tumor cells were dissociated from neurospheres and plated on prepared gels at low density (1-5 cells/mm^2) using NSC media +2% FBS.

To measure force transmission, Traction Force Microscopy (TFM) was performed as previously described [36]. Briefly, Nikon TiE and Ti2 epifluorescence microscopes were used to image fluorescent bead positions before and after cell detachment via trypsin. A Zyla 5.5 sCMOS camera (Andor Technology, Belfast, United Kingdom) and a 40x/0.95NA Ph2 lens with 1.5x intermediate zoom (60x total magnification, 110 nm spatial sampling) was used. Cells were maintained at 37 °C and 5% CO_2 for the duration of imaging using an Oko lab Bold Line top stage humidified incubator (Okolab, Ottaviano, Italy). At each stage position, a phase contrast image of the cell was acquired. Next, an image of fluorescent beads at the top surface of the gel was captured using a 575/25 nm LED and eGFP/mCherry filter set with LED fluorescence illumination from a SpectraX Light Engine (Lumencor, Beaverton, OR). Media in dishes was carefully removed, cells were detached with 0.25% trypsin/EDTA (Corning, Corning, NY), and fluorescence images of beads in the absence of cells were acquired at saved stage positions.

Using a previously described method [36], the displacement field was determined using particle image velocimetry (PIV) using the before and after bead images. A window size of 80-pixels (8.8 µm) square was used in PIV and a final lattice spacing of 20 pixels (2.2 µm) was achieved. Stress and displacement vectors were obtained by solving the inverse Boussinesq problem in Fourier space [82]. By integrating the product of the stress and displacement vectors over

the entire image, substrate strain energy was determined as previously described[36].

Stochastic cell migration simulator

The previously described [35,36] cell migration simulator (CMS v1.0) was used to simulate cells migration dynamics in response to changes in cell adhesion. The parameters used in the simulations are presented in Table S1. The number of adhesive clutches (N_c) was adjusted to model the change in adhesion observed between PDGF/Proneural and NRAS/Mesenchymal tumors. N_c of 2500 and 7500 clutches were used to simulate PDGF/Proneural and NRAS/Mesenchymal tumor cells, respectively. Four hours of cell dynamics were simulated and the first hour was excluded from analysis to allow the system to reach steady state. Analysis was performed using a ten-minute sampling interval as previously described [36].

Brownian dynamics tumor simulator (BDTS)

The Brownian dynamics tumor simulator was used as previously described with modifications [83,84]. In the present study, we extended the BTDS to 3-dimentional tumors and incorporated immune cells' dynamics as shown schematically in Figure 2.8A. Briefly, simulations started with 27 cancer cells, modeled as rigid sphere with radius (r_{cancer}), placed in a 3x3x3 grid where the distance between each cancer cell (center-center) is $3*r_{cancer}$. In simulation including immune response, eight T cells, also modeled as rigid sphere with radius (r_{CTL}), were included, and each was placed $1.5*r_{cancer}$ away from a

randomly selected cancer cell. At each simulation time step of 1 min, cancer and T cells are allowed to move randomly and grow as spheres with a linear volumetric growth rate. Movement and growth are rejected if the newly assigned space is already occupied by a like cell (i.e. no-overlap enforced between cancer cells and between T cells). However, a cancer cell and T cell contact occurs when a proposed cell movement put the distance between cell centers less than or equal ($r_{CTL}+r_{cancer}$). The duration of the contact is ($1/k_{dissoc}$), in this case 10 minutes. For every contact, both cancer cell and T cell take a “hit” that reduces their hit points (HP) by one. Both cancer cell and T cell have limited HP and once HP is depleted (equals 0), the cell dies or become exhausted. For NRAS simulations, T cells were added to the tumor simulator and T cell-mediated killing was simulated. For PDGF simulation, only cancer cells were simulated. Cancer cell motility was estimated from *ex vivo* brain slice imaging of tumor cells (Figure 3C) and proliferation rate was estimated from the *in vitro* proliferation of mouse primary tumor lines (Figure 2.7D). The rest of parameters were estimated based on previous published work or used as an adjustable parameter (see Table 2.S3).

Statistical analysis

Fisher’s exact test was used to compare the mouse and human transcriptomic clusters. One-way analysis of variance was used to compare transcript levels. Rank test, Kruskal-Wallis, one-way analysis of variance was used to compare single cell behaviors and IHC quantifications. Where

appropriate, a subsequent Dunn-Sidak test for multiple comparisons was performed.

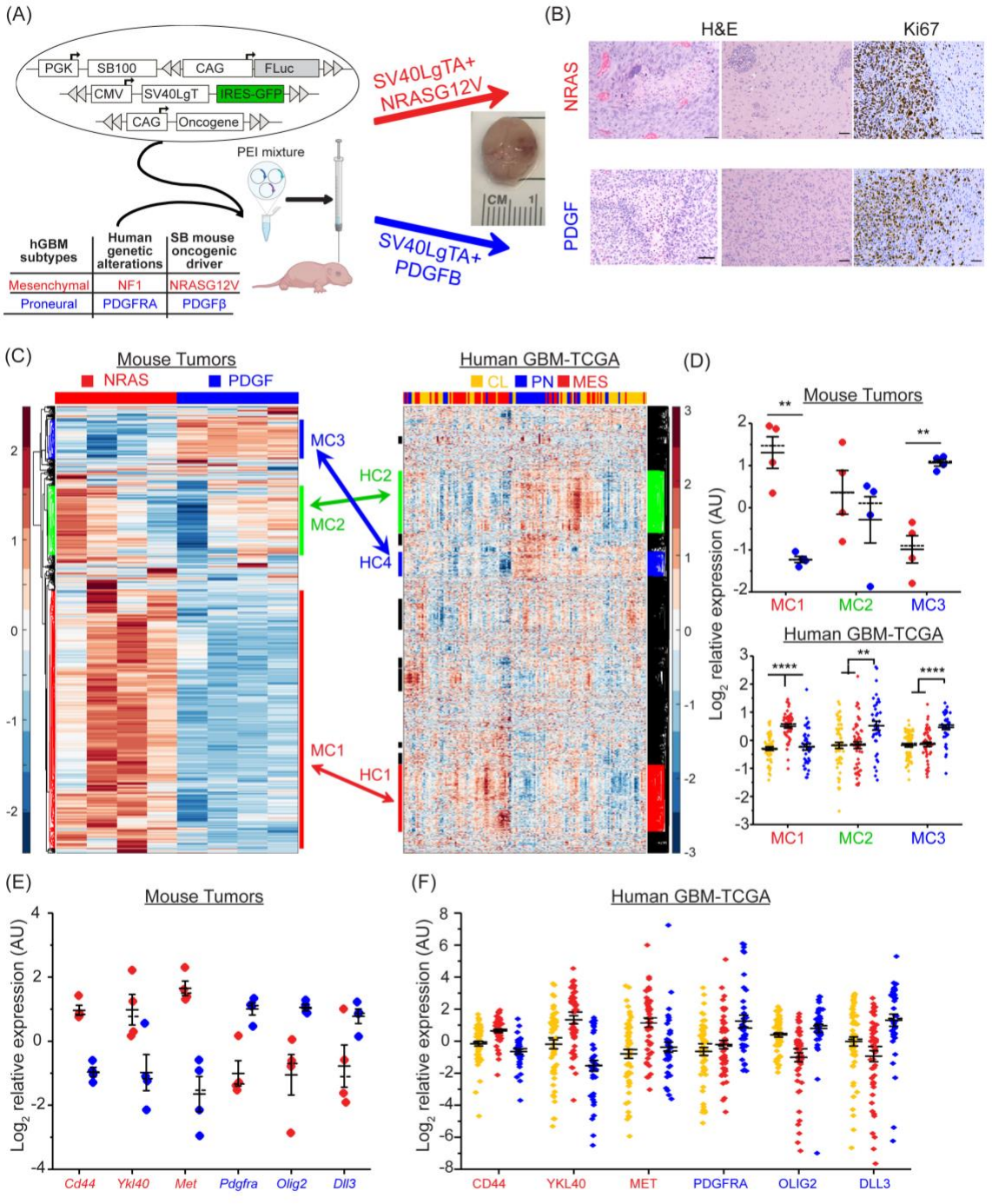
(A)
PGK
SB100
CAG
FLuc
CMV
SV40LgT
IRES-GFP
CAG
Oncogene
PEI mixture
SV40LgTA+
NRASG12V
SV40LgTA+
PDGFB
hGBM subtypes
Human genetic alterations
SB mouse oncogenic driver
Mesenchymal
NF1
NRASG12V
Proneural
PDGFRA
PDGFβ
(B)
H&E
Ki67
NRAS
PDGF
(C)
Mouse Tumors
NRAS
PDGF
Human GBM-TCGA
CL
PN
MES
MC3
MC2
MC1
HC2
HC4
HC1
(D)
Mouse Tumors
Log2 relative expression (AU)
MC1
MC2
MC3
Human GBM-TCGA
(E)
Mouse Tumors
Log2 relative expression (AU)
Cd44
Ykl40
Met
Pdgfra
Olig2
Dll3
(F)
Human GBM-TCGA
Log2 relative expression (AU)
CD44
YKL40
MET
PDGFRA
OLIG2
DLL3

Figure 2.1. *De novo* induced GBM mouse models using immune competent mice recapitulate mesenchymal and proneural subtypes of human GBM.

A) Schematic of mouse models. Plasmids encoding oncogenic drivers NRASG12V or PDGFβ in combination with SV40LgTA were injected into P1 FVB mice to induce mesenchymal and proneural high grade gliomas, respectively. B) H&E and Ki67 IHC staining of NRAS and PDGF tumor sections. Scale bar: 50 µm. C) Unsupervised hierarchical clustering of mRNA expression in induced mouse tumors and human IDHwt GBM-TCGA. Arrows indicate conserved genes present in both mouse and human gene clusters as defined by systematic comparison of gene cluster membership between datasets. D) Quantification of relative expression of mouse gene clusters within the mouse dataset (top panel) and human GBM molecular subtypes (lower panel). E,F) Relative expression of key mesenchymal and proneural genes within mouse tumors (E) and human tumors (F). Solid and dashed lines represent mean and median values, respectively. Error bar represents S.E.M. + $p < 0.05$, * $p < 0.01$, ** $p<0.001$, *** $p<0.0001$, **** $p<0.00001$

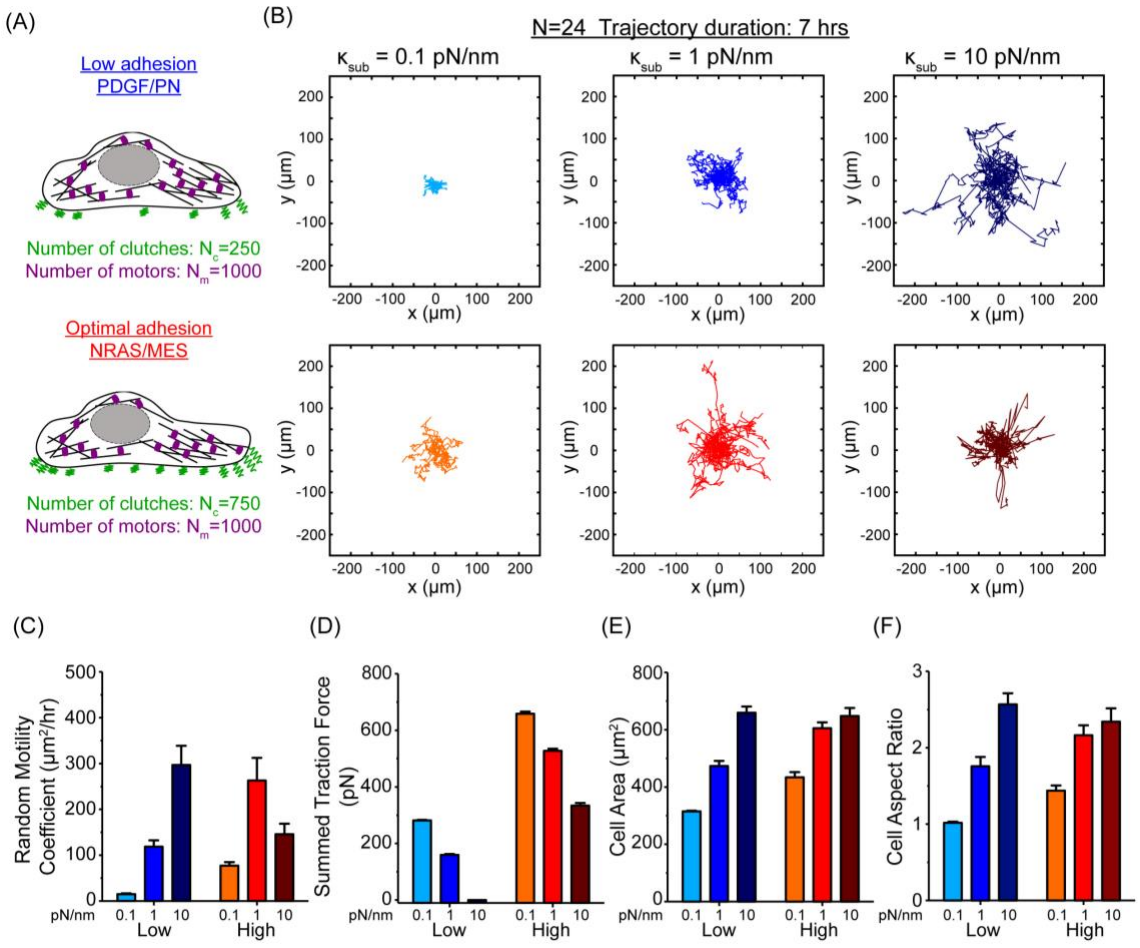

Figure 2.2. Simulations of cell migration speed as a function of subtype based on CD44-mediated cellular adhesive clutches.

A) Schematic of proneural (low CD44) and mesenchymal (medium CD44, i.e. optimal) subtypes. B) Wind-rose plots of simulated cell trajectories on different stiffnesses (κ_{sub}= 0.1, 1, 10 pN/nm). C) Simulated cell migration random motility coefficients show higher migration with increased (optimal) adhesion across a range of substrate stiffnesses. D) Cell summed traction force exhibits higher traction forces with increased (optimal) adhesion across all stiffnesses. E, F) Cell spread area and aspect ratio increase with increased adhesion on substrate stiffnesses of 0.1 and 1 pN/nm. Error bars are S.E.M.

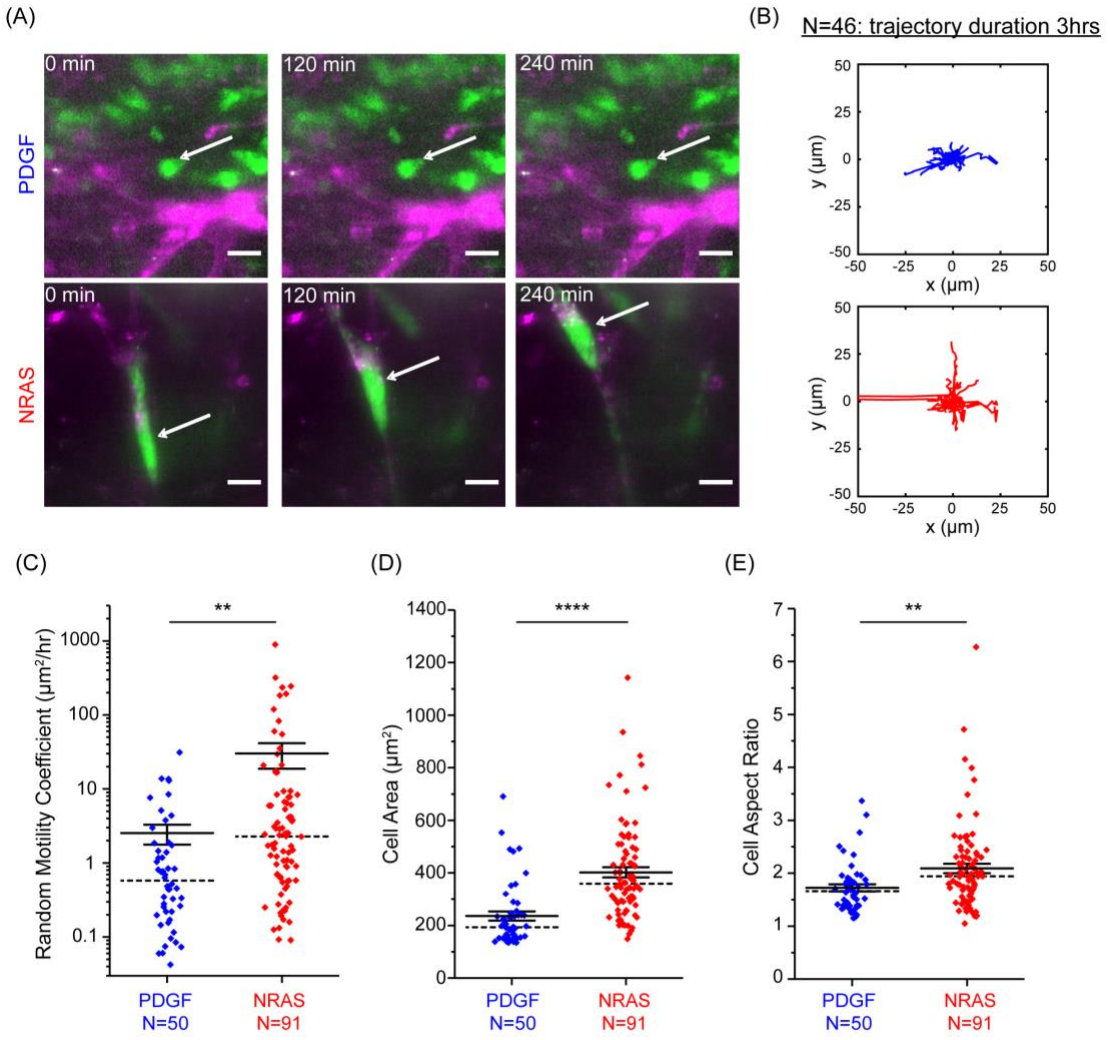

Figure 2.3. NRAS/Mesenchymal cells migrate faster, are more spread, and are more polarized than PDGF/Proneural cells in *ex vivo* tumor-bearing brain tissue.

A) Representative *ex vivo* fluorescent montage of GFP-tagged tumor cells (green) and blood vessels staining using isolectin B4 (magenta). B) Wind rose plots of NRAS/Mesenchymal and PDGF/Proneural migrating tumor cell migration trajectories (N=46). C) NRAS/Mesenchymal cancer cell motility is faster than for PDGF/proneural cancer cells. D&E) NRAS/Mesenchymal cancer cells are more spread and polarized than PDGF/Proneural cells as evidenced by larger spread area and aspect ratio. Solid and dashed lines represent mean and median, respectively. Error bars are S.E.M. +p <0.05 * p <0.01, ** p<0.001, *** p<0.0001, **** p<0.00001**.**

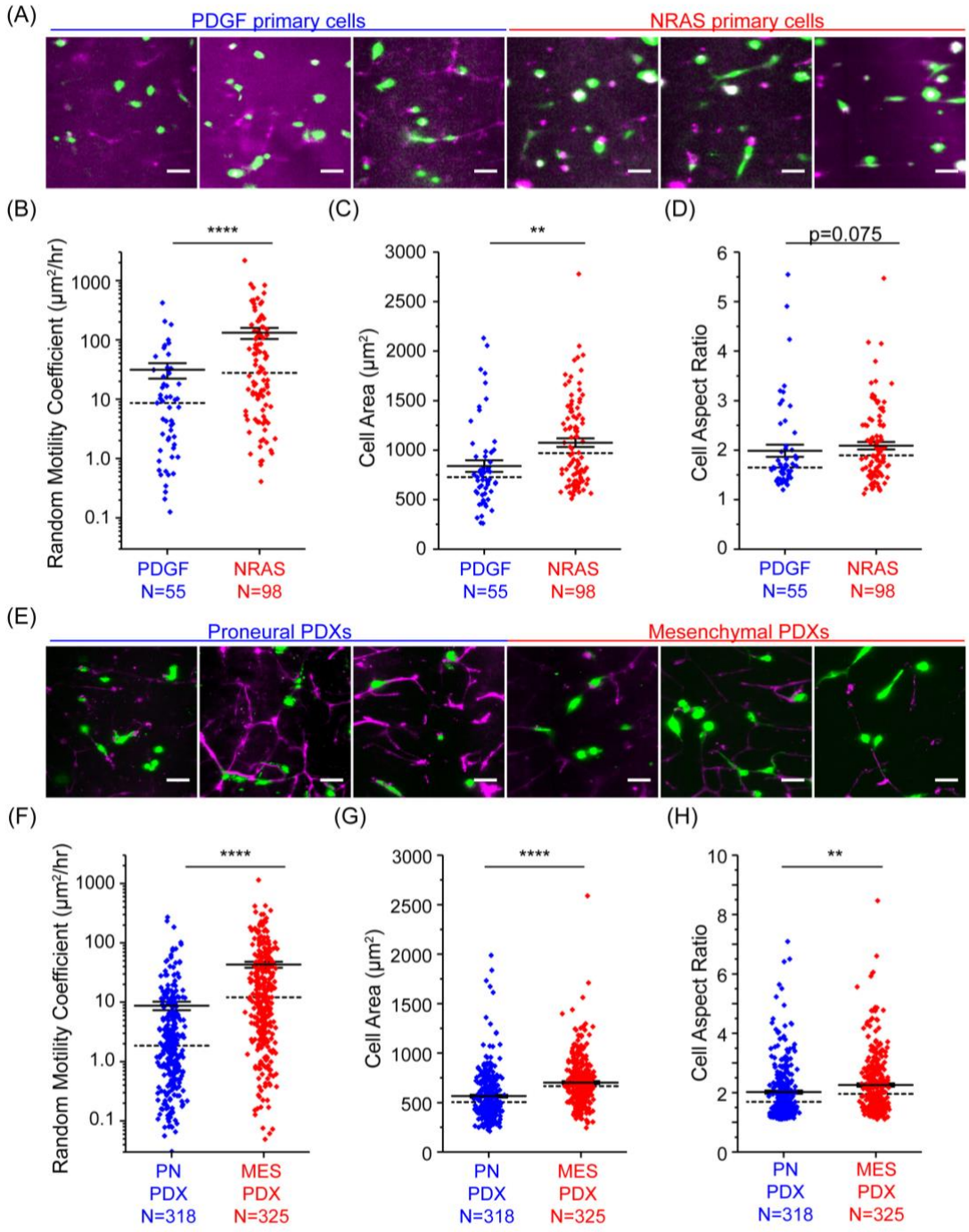
(A)
PDGF primary cells
NRAS primary cells
(B)
Random Motility Coefficient (μm²/hr)
****
PDGF N=55
NRAS N=98
(C)
Cell Area (μm²)
**
PDGF N=55
NRAS N=98
(D)
Cell Aspect Ratio
p=0.075
PDGF N=55
NRAS N=98
(E)
Proneural PDXs
Mesenchymal PDXs
(F)
Random Motility Coefficient (μm²/hr)
****
PN PDX N=318
MES PDX N=325
(G)
Cell Area (μm²)
****
PN PDX N=318
MES PDX N=325
(H)
Cell Aspect Ratio
**
PN PDX N=318
MES PDX N=325

Figure 2.4. Cancer cell migration is subtype specific and independent of the tumor microenvironment and species.

A) Six representative images of primary isolated cells from each of the two mouse tumor subtypes (3 NRAS and 3 PDGF). GFP-tagged tumor cells (green) and blood vessels staining using isolectin B4 (magenta). B) NRAS/Mesenchymal primary isolated tumor cancer cells migrate faster than PDGF/Proneural primary isolated cancer cells in normal mouse brain tissue as measured by random motility coefficientC&D) Quantification of cell spread area and cell aspect ratio showing that NRAS/Mesenchymal cancer cells are more spread (C) and tend to be somewhat more polarized (D), p=0.075, than PDGF/Proneural cancer cells in healthy brain slices. E) Six representative images of proneural and mesenchymal PDX lines cells in healthy mouse brain tissue. Labeled tumor cells using DiO membrane dye (green) and blood vessel staining using isolectin B4 (magenta). F) Mesenchymal PDX cells migrate faster than proneural PDX cells in normal mouse brain tissue as measured by random motility coefficient. G&H) Quantification of cell spread area and cell aspect ratio showing that mesenchymal PDX cells are more spread (G) and are more polarized (H) than proneural PDX cells in healthy brain slices. Solid and dashed lines represent mean and median values respectively. Error bars are S.E.M. +p <0.05 * p <0.01, ** p<0.001, *** p<0.0001, **** p<0.00001

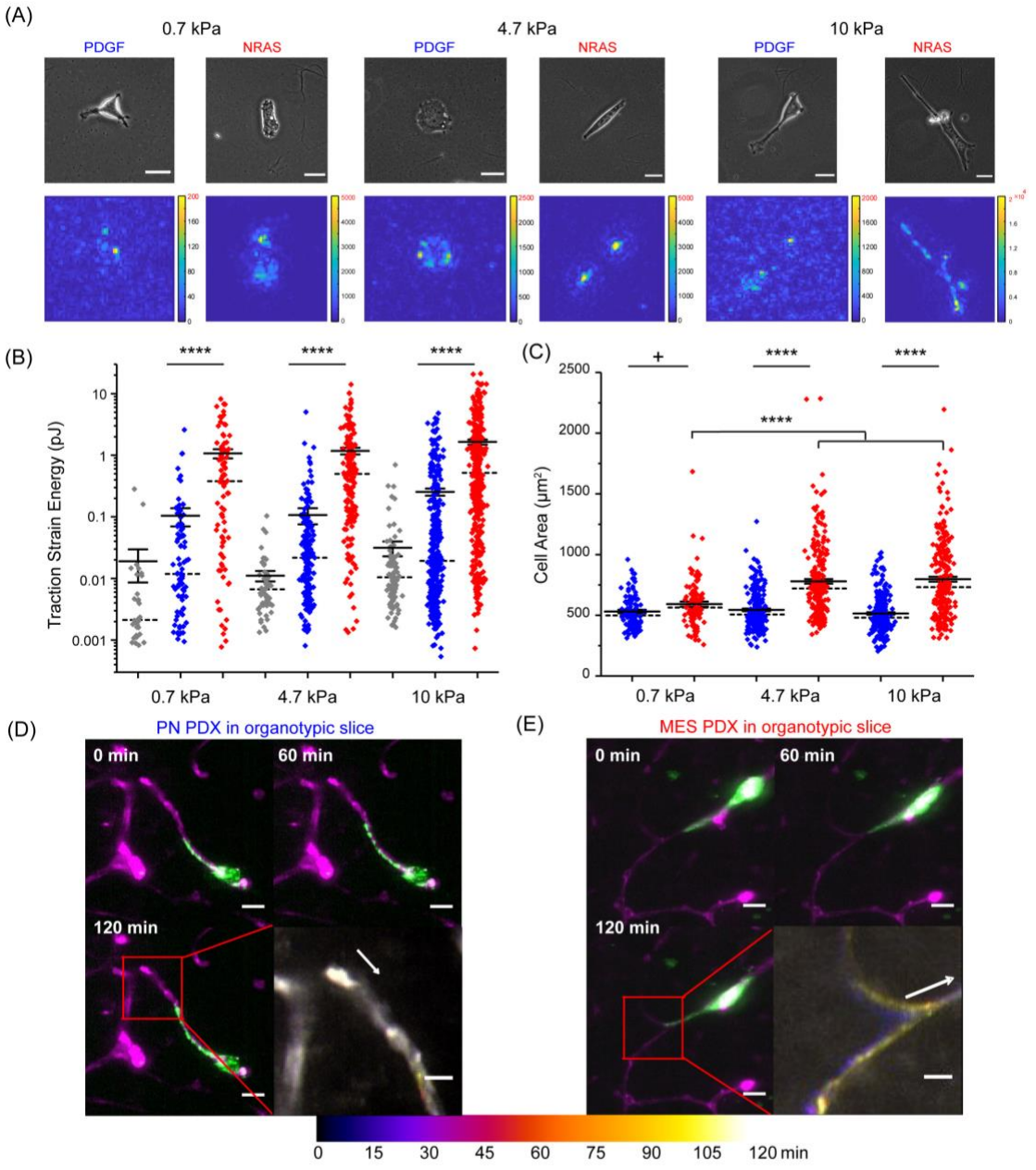
(A)
0.7 kPa
4.7 kPa
10 kPa
PDGF
NRAS
(B)
Traction Strain Energy (pJ)
0.7 kPa
4.7 kPa
10 kPa
(C)
Cell Area (μm²)
(D)
PN PDX in organotypic slice
0 min
60 min
120 min
(E)
MES PDX in organotypic slice
0 15 30 45 60 75 90 105 120 min

Figure 2.5. NRAS/Mesenchymal cancer cells generate larger traction forces *in vitro* on 2D hydrogels and *ex vivo* in brain slices than PDGF/Proneural cancer cells.

A) Representative phase contrast images and traction force magnitude heatmaps on type I collagen-coated polyacrylamide hydrogels across different substrate stiffnesses. B) NRAS/Mesenchymal cancer cells (red) generate higher traction forces as measured by total strain energy relative to PDGF/Proneural (blue) cancer cells. Measurement noise is presented (grey) across all stiffnesses. C) Similar to mouse brain slices, NRAS/Mesenchymal cancer cells (red) cultured on collagen-coated polyacrylamide hydrogels have larger spread area than PDGF cancer cells (blue). D &E) Tissue deformation visualized using temporal-color coding using 2 hours time-lapse and 15 minutes time interval. Mesenchymal PDX cells generate larger deformations of mouse brain capillaries (E) than proneural PDX cells shown in (D). Scale bar = 20µm, and inset scale bar = 10µm. Solid and dashed lines represent mean and median values, respectively. Error bars are S.E.M. +p <0.05 * p <0.01, ** p<0.001, *** p<0.0001, **** p<0.00001**.**

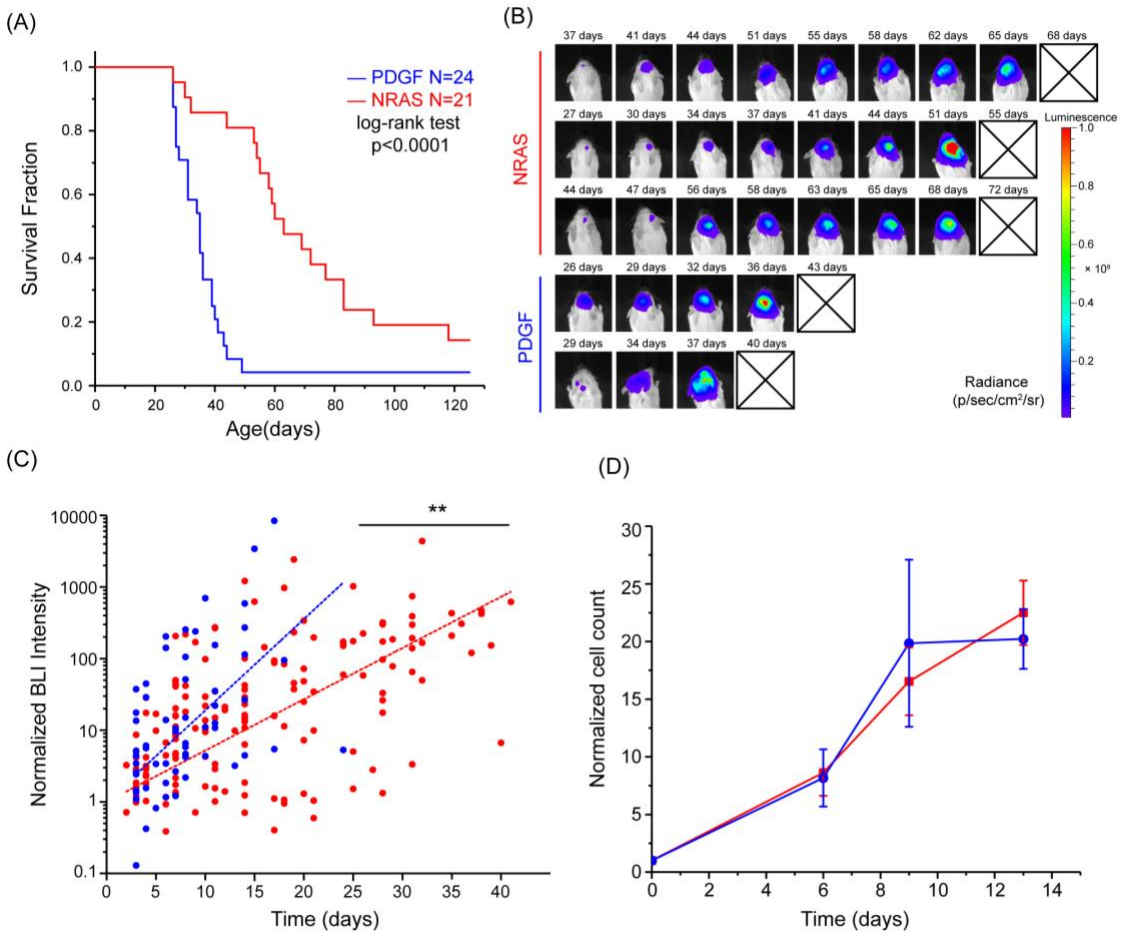

Figure 2.6. NRAS/Mesenchymal mice live longer than PDGF/Proneural mice.

A) Kaplan-Meier plot of animal survival for NRAS/Mesenchymal and PDGF/Proneural tumor-bearing mice shows extended survival of the NRAS/Mesenchymal cohort. Log rank Mantel–Cox test p<0.00001. B) Bioluminescence imaging (BLI) of NRAS/Mesenchymal mice shows slower growing tumors relative to PDGF/Proneural mice. C) Quantification of BLI integrated intensity for the two cohorts. Normalized BLI intensity for all data points and linear fits for each cohort. PDGF/Proneural slope=0.127±0.01191 and NRAS/Mesenchymal slope=0.0716±0.00343, D) Ki67 IHC staining of mouse tumor sections, scale bar = 50 μm. E) Normalized cell count of primary isolated mouse tumor cells showing no significant difference in proliferation rate *in vitro* using neurosphere culture. Solid and dashed lines represent mean and median values, respectively. Error bars are S.E.M. +p <0.05 * p <0.01, ** p<0.001, *** p<0.0001, **** p<0.00001.

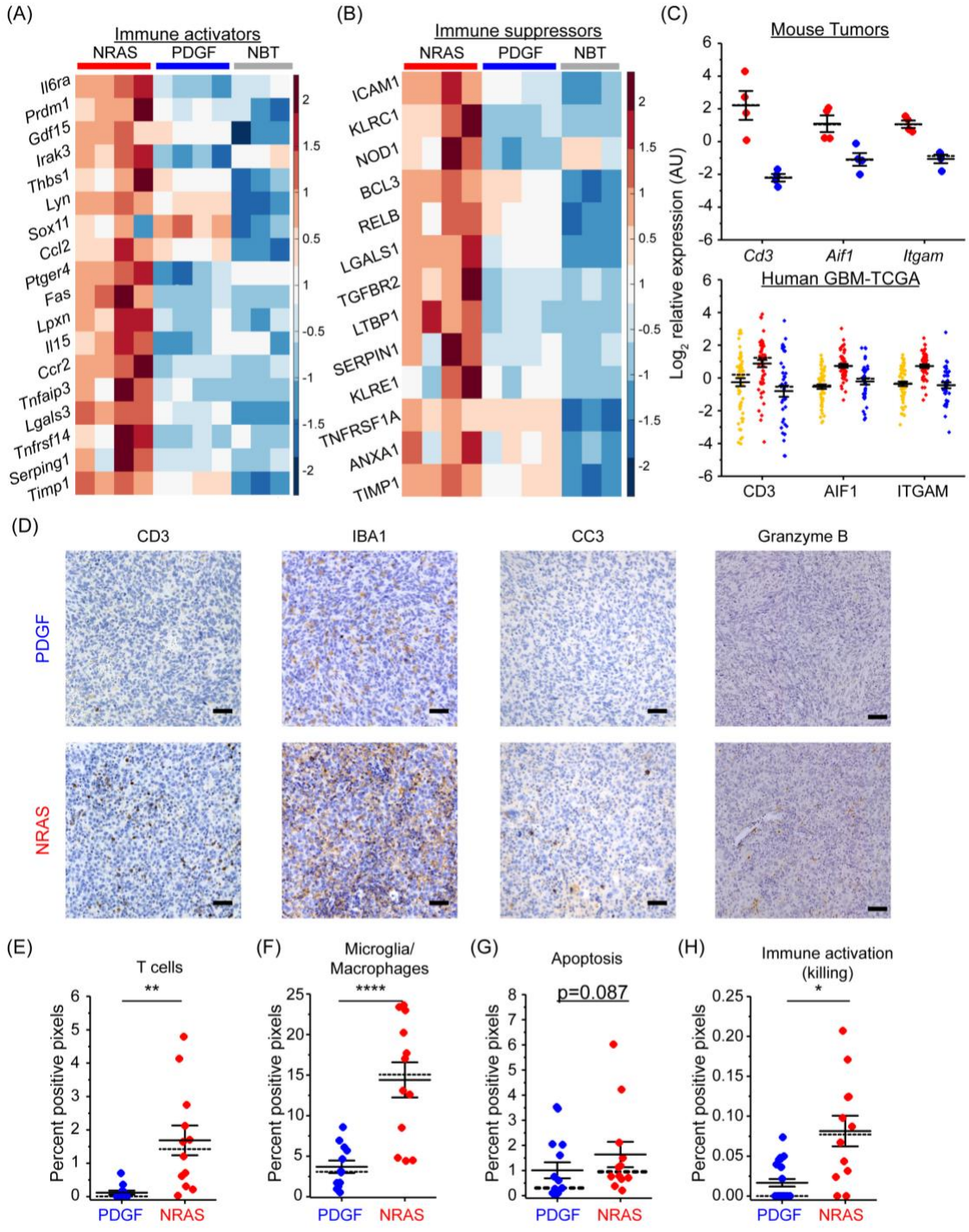
(A)
Immune activators
NRAS
PDGF
NBT
Il6ra
Prdm1
Gdf15
Irak3
Thbs1
Lyn
Sox11
Ccl2
Ptger4
Fas
Lpxn
Il15
Ccr2
Tnfaip3
Lgals3
Tnfrsf14
Serping1
Timp1
(B)
Immune suppressors
NRAS
PDGF
NBT
ICAM1
KLRC1
NOD1
BCL3
RELB
LGALS1
TGFBR2
LTBP1
SERPIN1
KLRE1
TNFRSF1A
ANXA1
TIMP1
(C)
Mouse Tumors
Cd3
Aif1
Itgam
Human GBM-TCGA
CD3
AIF1
ITGAM
Log2 relative expression (AU)
(D)
CD3
IBA1
CC3
Granzyme B
PDGF
NRAS
(E)
T cells
**
Percent positive pixels
PDGF
NRAS
(F)
Microglia/
Macrophages
****
Percent positive pixels
PDGF
NRAS
(G)
Apoptosis
p=0.087
Percent positive pixels
PDGF
NRAS
(H)
Immune activation
(killing)
*
Percent positive pixels
PDGF
NRAS

Figure 2.7. NRAS/Mesenchymal tumors are immunologically “hot” and PDGF/Proneural tumors are immunologically “cold,” consistent with human GBM subtypes.

A, B) Clustering analysis of immune activators and suppressors previously reported in human GBM (Doucette *et al*., 2013). Similar to mesenchymal GBM, NRAS/Mesenchymal tumors have elevated immune activator and suppressor expression relative to normal brain tissue and PDGF/Proneural tumors. C) Expression of immune cell surface marker genes in mouse (top) and human (bottom) tumors shows elevated expression in NRAS/Mesenchymal tumors and human mesenchymal GBM tumors relative to PDGF/Proneural and human proneural GBM tumors. D) Immunohistochemistry (IHC) confirms elevated immune cell infiltration in NRAS tumors and associated elevation of immune-mediated killing of tumor cells. E,F,G,H) Quantification of IHC images using a k-means clustering algorithm. Solid and dashed lines represent mean and median values, respectively. Error bars are S.E.M. +p <0.05 * p <0.01, ** p<0.001, *** p<0.0001, **** p<0.00001.

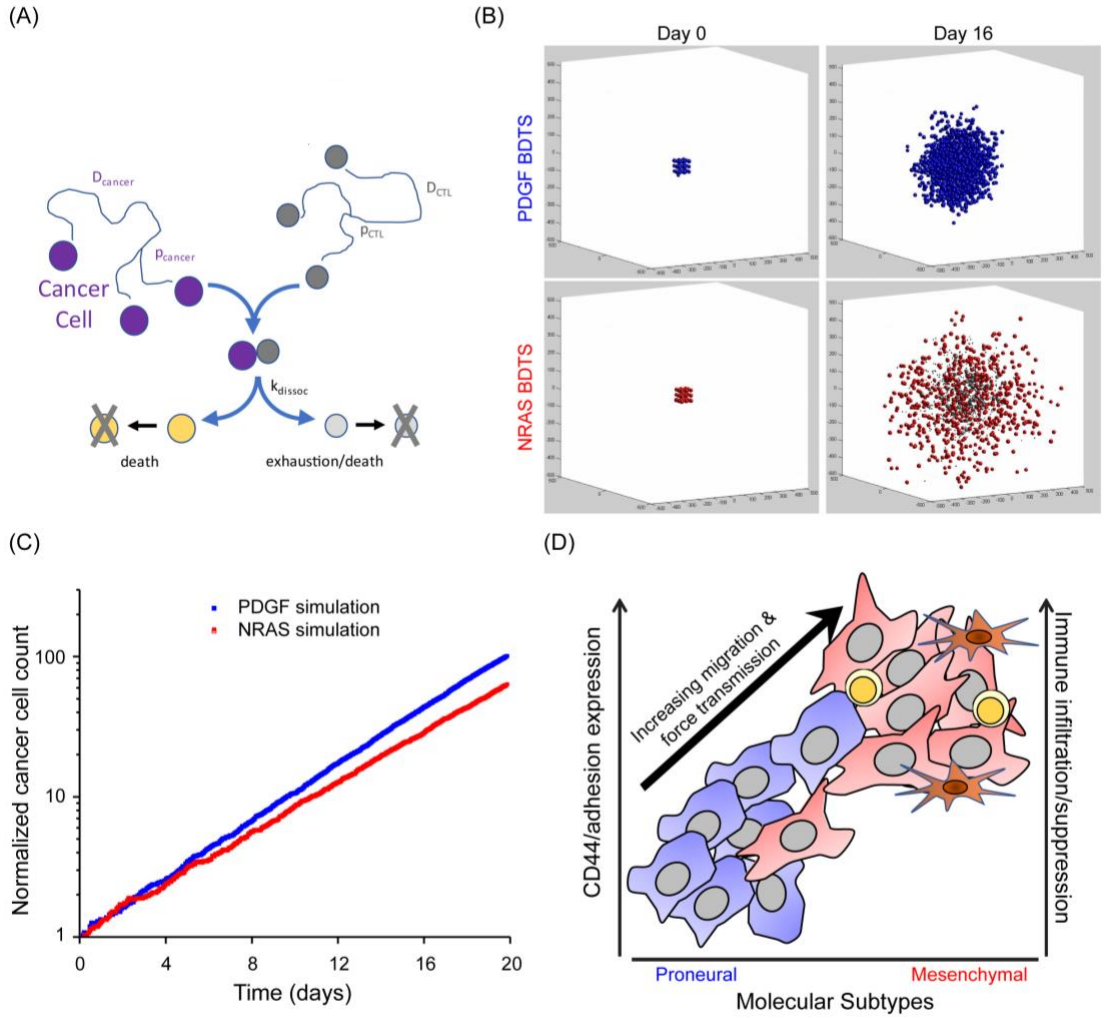

Figure 2.8. Brownian dynamics tumor simulator (BDTS) of 3D NRAS/Mesenchymal and PDGF/Proneural tumors.

A) Schematic showing a diagram of the model. B) Simulator output at day 0 and day 16 for PDGF and NRAS simulations. In NRAS simulations, dead cancer cells are larger grey spheres and T cells are smaller black spheres. C) Cancer cell count over time showing the difference in tumor growth in the presence of T cells with simulated PDGF/Proneural tumors growing faster than NRAS/mesenchymal tumors. D) Cartoon summary of the main findings depicting the relationship between molecular subtypes, cellular adhesion, cell migration, and immune response.

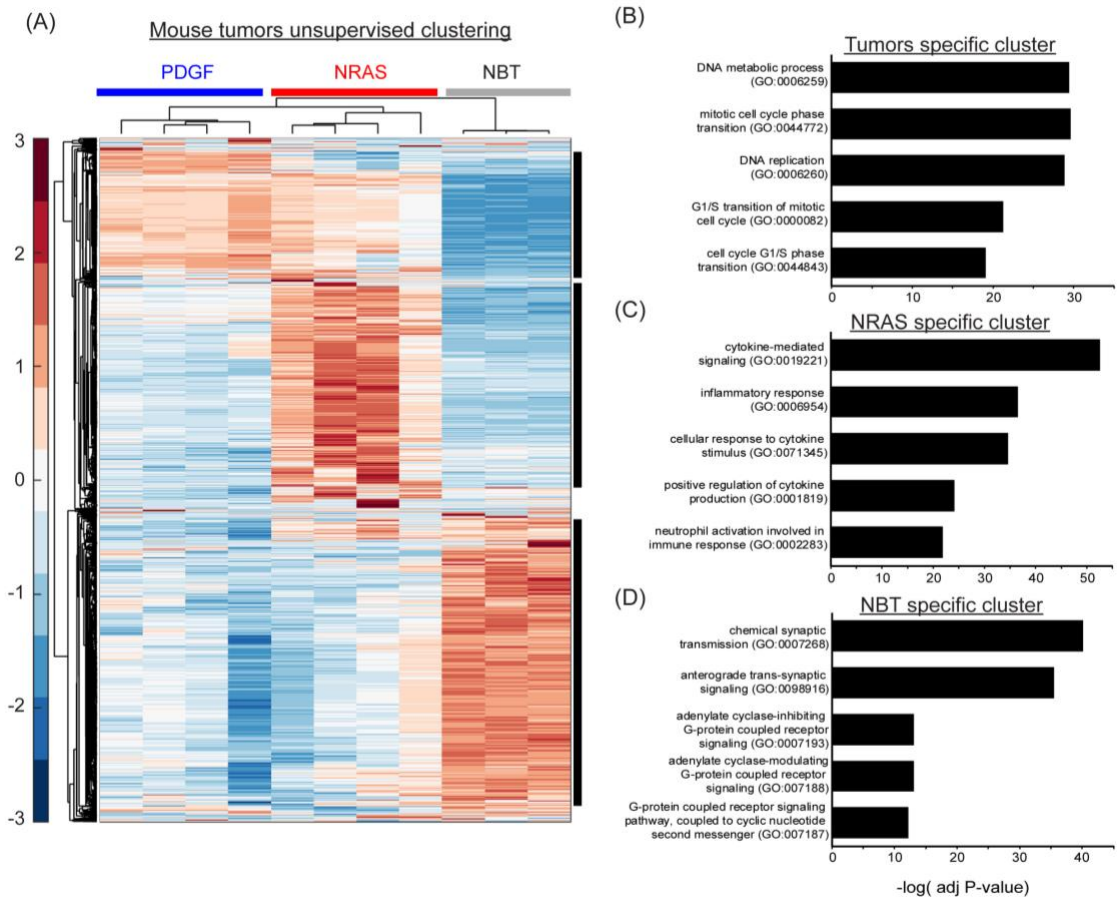

Figure 2.S1. Unsupervised clustering of mouse tumor and healthy brain tissue transcriptomic profiles and pathway enrichment analysis.

A) Heatmap showing expression profile of NRAS and PDGF tumors and healthy mouse brain tissues. Heatmap shows existence of three gene clusters: Tumor-specific cluster, normal brain tissue specific cluster and NRAS tumor-specific cluster. B,C&D) Gene ontology analysis of gene clusters was performed using EnrichR.

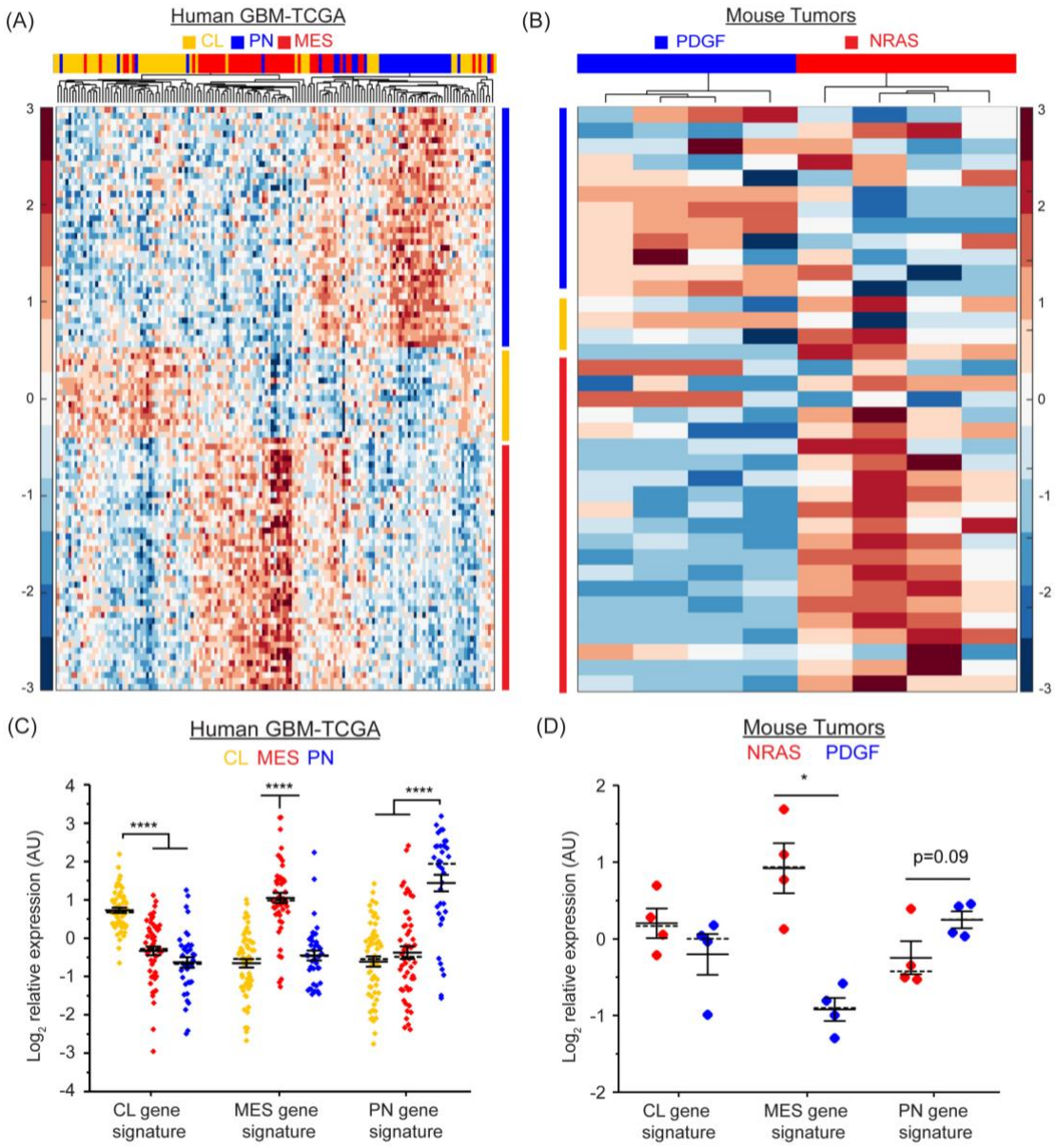

Figure 2.S2. Clustering analysis of mouse and human tumors using gene signatures associated with classical, mesenchymal, and proneural subtypes.

A) Heatmap shows the clustering of human GBM samples using subtype-specific gene signatures. B) Heatmap shows the clustering of mouse tumors using subtype-specific gene signatures. C&D) Quantification of subtype gene signatures within human GBM subtypes and NRAS and PDGF mouse tumors. Solid and dashed lines represent mean and median values respectively. Error bars are S.E.M. +p <0.05 * p <0.01, ** p<0.001, *** p<0.0001, **** p<0.00001.

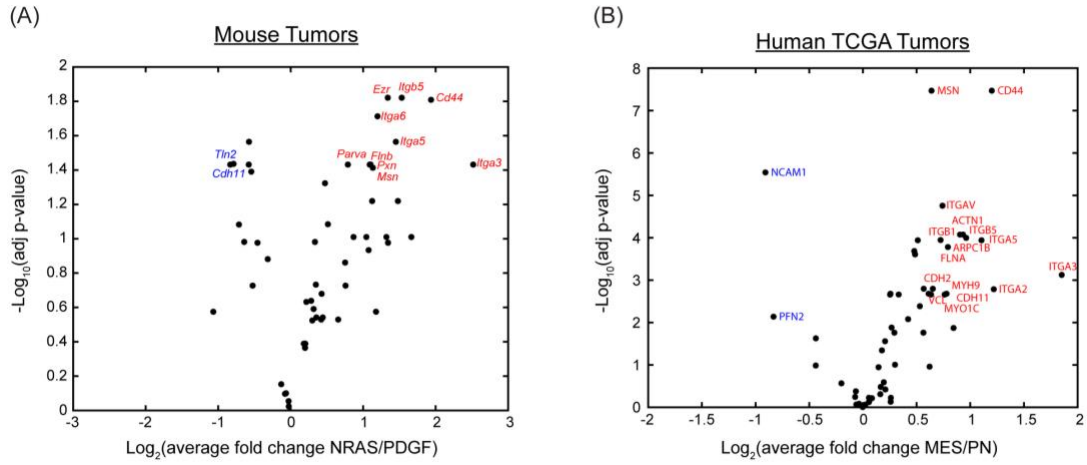

Figure 2.S3. Differential expression analysis of cell migration genes.

Volcano plot depicting $-\log_{10}$(adj p value) calculated using FDR adjusted Student's t test versus $\log_2$(average FC) for individual genes in A) mouse tumors and B) human TCGA-GBM

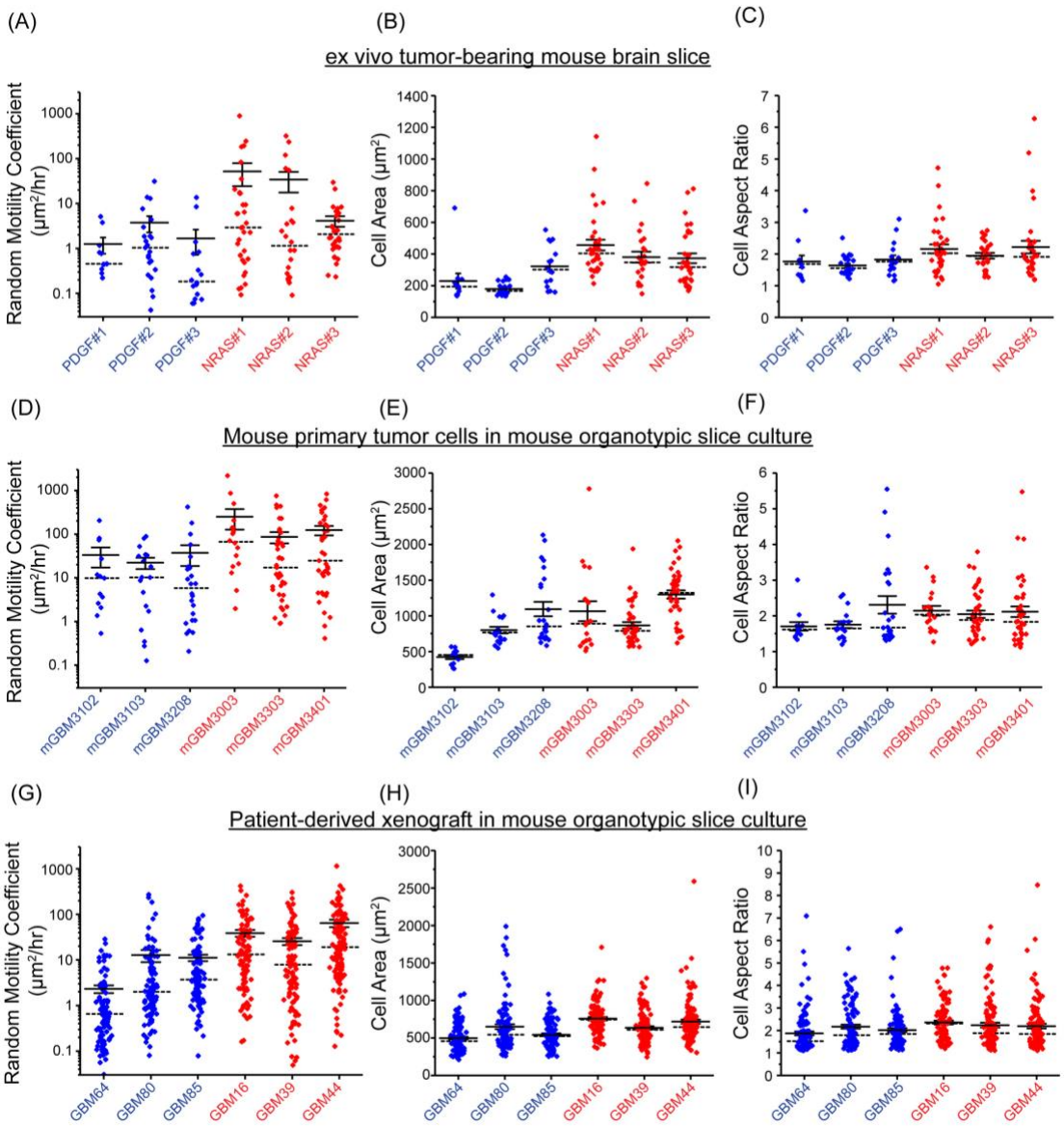

Figure 2.S4. Quantification of single cell migration and cell morphology.

A, B, & C) *Ex vivo* migration and morphology data from each individual animal. D, E, & F) Migration and morphology data for each individual mouse primary tumor line in mouse organotypic brain slice. G, H, & I) Migration and morphology data for each individual PDX line in mouse organotypic brain slice.

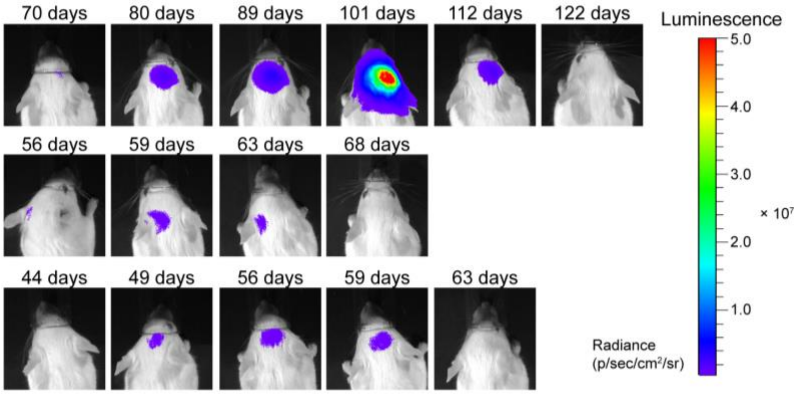

Figure 2.S5. BL image sequences showing tumor regression in some rare cases.

All three surviving mice in NRAS cohort showed tumor regression.

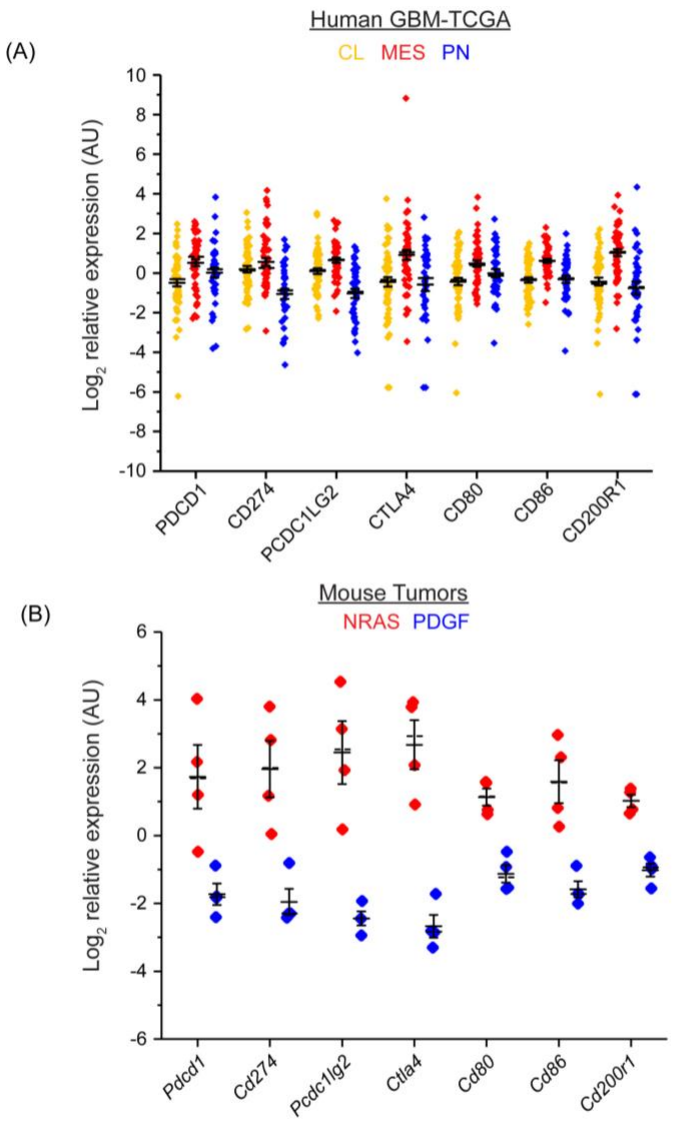

Figure 2.S6. Expression of immune checkpoint genes within mouse tumors.

Expression of immune checkpoint genes were upregulated in NRAS tumors relative to PDGF tumors (B) similar to human mesenchymal and proneural (A).

Table 2.S1: Cell migration simulator parameter values

Symbol	Parameter	Value
N_m	Total number of motors	10,000
N_c	Total number of clutches	250; 750
A_{tot}	Total possible actin protrusion length	100 μm
v_p*	Maximum actin polymerization velocity	200 nm/s
k_{mod}*	Maximum module birth rate	1 s^{-1}
k_{cap}	Module capping rate	0.001 s^{-1}
l_{in}	Initial module length	5 μm
l_{min}	Minimum module length	0.1 μm
κ_{cell}	Cell spring constant	10,000 pN/nm
$n_{c,cell}$	Number of cell body clutches	10;
n_m*	Maximum number of module motors	0.1*N_c
F_m	Motor stall force	2 pN
v_m*	Unloaded motor velocity	120 nm/s
n_c*	Maximum number of module clutches	75; 750
k_{on}	Clutch on-rate	1 s^{-1}
k_{off}*	Clutch unloaded off-rate	0.1 s^{-1}
κ_c	Clutch spring constant	0.8 pN/nm
F_b	Characteristic clutch rupture force	2 pN
κ_s	Substrate spring constant	Variable

Table 2.S2: Characteristics of patient-derived xenograft (PDX) lines used in this study

GBM	Xenograft start	Sex	Molecular subtype (RNAseq)
GBM16	2002	F	mesenchymal
GBM39	2003	M	mesenchymal
GBM44	2003	F	mesenchymal
GBM64	2006	F	proneural
GBM80	2007	M	proneural
GBM85	2008	M	proneural

Table 2.S3: Brownian dynamics tumor simulator parameters values

Parameter Name	Parameter	Value	Units	Reference
Cancer cell radius	r_{cancer}	10	μm	
T cell radius	r_{CTL}	3	μm	
Cancer cell motility	D_{cancer}	7.8; 42	$\mu m^2/h$	This study
T cell motility	D_{CTL}	300	$\mu m^2/hr$	[97,98]
Cancer cell proliferation	p_{cancer}	0.5	1/d	This study
T cell proliferation	p_{CTL}	1	1/d	[99]
Contact duration	$1/k_{dissoc}$	10	min	[98,100]
Cancer cell HP*	HP_{cancer}	1	contacts	[98]
T cell HP*	HP_{CTL}	20	contacts	Unknown, adjustable

Chapter 3

CD44 functions as a molecular clutch to support stiffness-sensitive force transmission and cell migration

*Chapter 3 contains work by **Shamsan, G.A**., Manning, R., Smeester, B.A., Rosenfeld, S.S., Largaespada D.A., and Odde, D.J., In preparation*

Authors: Ghaidan A. Shamsan[1], Riley Manning[1], Branden A. Smeester[2], Steven S. Rosenfeld[3], David A. Largaespada[2,4], David J. Odde[5]

Affiliations:
[1] Department of Biomedical Engineering, University of Minnesota, Minneapolis, MN 55455
[2] Department of Pediatrics, University of Minnesota, Minneapolis, MN 55455
[3] Department of Molecular Pharmacology and Experimental Therapeutics, Mayo Clinic, Jacksonville, FL 32224
[4] Masonic Cancer Center, University of Minnesota, Minneapolis, MN 55455
[5] Department of Biomedical Engineering, University of Minnesota, Minneapolis, MN 55455, USA. Electronic address: oddex002@umn.edu

Authors contribution:
GAS, SSR, DAL and DJO contributed to study conception and design.
GAS and DJO contributed to writing the manuscript
GAS and BAS contributed to the generation of CD44 knockout lines
GAS and RM contributed to data acquisition and analysis
GAS ran and analyzed the cell migration simulations

3.1 Summary

Due to its ability to bind to both extracellular matrix and to intracellular F-actin via adaptor proteins, CD44 has been hypothesized to act as a molecular clutch to enable cancer cell migration. However, while the mechanics and force transmission of integrin-mediated adhesion have been extensively investigated, the mechanics of CD44-dependent force transmission and cell migration mechanics have yet to be similarly characterized. Using an immobilized anti-CD44 antibody to ensure cell adhesion via CD44, we quantitatively characterized the cell adhesion, migration, and force transmission on compliant 2D hydrogels. We find that, in U251 human glioblastoma cells, CD44 acts as a *bona fide* molecular clutch mediating cell migration and force transmission. Integrated computational modeling and biophysical measurements showed that CD44 mediated migration is both adhesion ligand density and substrate stiffness sensitive in a manner consistent with the motor-clutch model. Overall, we conclude that CD44 and integrins exhibit functional conservation of adhesion mechanics despite their highly divergent primary sequences and structures.

3.2 Introduction

Cell migration is an important biological process that plays a key role in a variety of biological and pathological conditions including embryogenesis, wound healing, immune response, and cancer invasion and metastasis [19]. In cell migration, cell-extracellular matrix (ECM) interactions play a critical role because it enables cells to sense and respond to changes in their microenvironment and to maintain cellular function and tissue homeostasis[101]. Cells interact with the

ECM through specialized transmembrane proteins, such as integrins, to mediate cell adhesion and force transmission. These interactions are mediated through molecular clutches, composed of transmembrane and adapter proteins that link the actin cytoskeleton to the outside environment[24,25,102].

CD44 is a cell surface glycoprotein which serves as the major receptor for hyaluronic acid (HA) [40–42]. CD44 regulates many biological processes and it is considered a cancer stem cell and an epithelial-to-mesenchymal transition (EMT) marker [43–45]. CD44 has been linked to several different cancer types, such as breast, lung, prostate, and brain, and has been reported to contribute to cancer invasiveness[46–48]. In addition to its reported function as a signaling molecule, CD44 functions as an adhesion molecule by interacting with HA and other reported ECM components [43]. For instance, in glioblastoma, where HA is highly abundant [40], CD44 has been shown to regulate cell migration and hypothesized to function as a molecular clutch [35]. Despite a number of studies associating CD44 with cell migration, direct biophysical measurements of CD44 function as an adhesion molecule capable of supporting cell adhesion, migration and force transmission have not been made [57,58,103–106]. Previous work has demonstrated CD44 ability to support cell adhesion and described a 3D migration mode which utilized CD44-enriched microtentacle structures [57,58]. However, a key question remains whether CD44-mediated adhesion and migration behave similar to integrin-based adhesions. In addition, can CD44 transmit forces and sense changes in adhesion density and stiffness of the substrate? These questions are

important to understand the biophysics of CD44 and its mechanistic role in cancer cell migration.

We have previously described a cell migration simulator (CMS), based on the motor-clutch framework, to define the biophysics driving adhesion and stiffness sensing [35,36]. The CMS simulates actin-based protrusion dynamics and predicts cell migration in response to changes in the environment or cellular components critical for the process of cell migration. The model incorporates myosin motors, adhesion molecules 'clutches', actin polymerization and adhesion binding and unbinding rates [36]. In this study, we tested the hypothesis that CD44 is a molecular clutch capable of mediating cell migration and force transmission, as previously described for integrins in the context of the motor-clutch framework [24,27,29,31–33,36,38]. We created a CD44-specific substrate via immobilized anti-CD44 antibody (IM7) on polyacrylamide hydrogels to ensure that cell adhesion was CD44-mediated. We showed, using the U251 human glioblastoma cell line, that CD44 is capable of mediating cell adhesion, migration and force transmission. CD44-dependent cell morphology, migration and force transmission was found to be responsive to changes in adhesion density and substrate stiffness. Lastly, CD44-mediated force transmission exhibits load and fail dynamics shown previously to drive stiffness sensing in compliant mechanical environments [24,34,107].

3.3 Results

3.3.1 Immobilized anti-CD44 antibody supports CD44-dependent cell adhesion and migration

To test CD44 function as an adhesion molecule, we sought to create a substrate capable of specifically associating with CD44 where the environmental mechanical properties and surface chemistry can be readily controlled. We chose polyacrylamide hydrogel (PAGs) because it allows for modulating substrate Young's modulus and covalently immobilizing proteins on its surface using bifunctional cross-linkers such as sulfo-SANPAH [96]. We immobilized anti-CD44 monoclonal antibody, IM7, which has been shown to inhibit HA binding to CD44[108], on the surface to engage CD44. Also, a CD44-knockout U251 cell line (CD44KO) was created using CRISPR/Cas9 (Figure 3.1A). U251 cells are able to adhere to IM7 coated PAGs at similar level as Collagen I (Col I) coated PAGs (Figure 3.1B). Adhesion of U251 cells was specific to IM7 and dependent on CD44. Cells plated on IgG2b control isotype did not adhere to PAGs. In addition, CD44KO cells were not able to adhere to IM7 coated PAGs.

In addition to supporting cell adhesion, time-lapse imaging shows that U251 cells are capable of spreading and migrating on IM7 coated PAGs. Figure 3.1C shows image sequences of U251 cells migrating on IM7 and Col I coated PAGs. Similar to integrin-dependent migration, cells on IM7 form a polymerization-driven leading edge and retract the rear as they migrate (Figure 3.1C). Relative to cell migration on Col I coated PAGs, U251 cells are more migratory on IM7 coated PAGs as shown using representative wind-rose

trajectories and MSD plots in Figure 3.1D-E. This establishes IM7 coated PAGs as a CD44-specific substrate to study the biomechanics of CD44-mediated adhesion, migration and force transmission.

3.3.2 Cell migration and morphology are dependent on substrate adhesivity

If CD44 functions as a molecular clutch linking the actin cytoskeleton with the outside environment, the cell migration simulator (CMS) predicts cells would respond to adhesion density as it has been shown in integrin-dependent cell migration systems [22,23]. The simulations predict an optimality in cell migration as a function of adhesion density which was modeled by adjusting the number of clutches (N_c=500-10,000) and maintaining the number of motors (N_m=10,000). Figure 3.2A shows representative wind-rose trajectories from each simulation condition. Trajectories were analyzed using a random walk model and the random motility coefficient of cell migration was computed in Figure 3.2B, which shows migration rate is biphasic with respect to adhesivity, i.e. increases with increased adhesion up to a maximum, and then decreases at the highest clutch level (N_c=10,000). In addition, the simulations predict an increase in cell spread area and aspect ratio (polarization) as a function of increasing number of clutches (Figure 3.2C-D).

To test these predictions and whether U251 cell migration on IM7 exhibit similar behavior as integrin-dependent migration, we altered the amount of IM7 on the surface by coating PAGs using 1, 10, 100, and 300 µg/mL IM7 solution. As predicted from the motor-clutch model, U251 cells exhibit an optimal migration

on 100 µg/mL IM7 coated PAGs. Figure 3.2E-F show representative phase contrast images and wind-rose trajectories for each antibody concentration. Quantification of cell trajectories revealed a biphasic random motility coefficient as a function of increased adhesion density (Figure 3.2G). Migration rate was significantly different at 100 than 300 and 10 µg/mL coating, $p = 0.015$. Consistent with simulation results, cell area and aspect ratio as a function of adhesivity showed similar trends as simulation results (Figure 3.2H-I)

3.3.3 Traction strain energy is dependent on substrate adhesivity

In addition to cell morphology and dynamics, the CMS predicts a monotonic increase in traction forces as a function of clutch number, as shown in Figure 3.3A. To test the model prediction in the context of CD44-mediated force transmission, we performed traction force microscopy (TFM) using PAGs embedded with fluorescent beads and coated with different concentrations of IM7. U251 cells are able to transmit forces and exhibit an increase in traction strain energy as IM7 coating increases (Figure 3.2B). Representative phase contrast images and traction heatmaps of cells on 1 and 300 µg/mL coated gels are shown in Figure 3.2C-D which display traction forces localized to cell periphery. These results demonstrate the ability of CD44 to transmit forces and function as a molecular clutch.

3.3.4 Cell migration and morphology is substrate stiffness sensitive and exhibit optimality

Using HA-methylacrylate hydrogels, CD44-dependent cell spreading was shown to be mechanosensitive [57]. In addition, we previously demonstrated using simulations and experimental data, that cell migration exhibits a biphasic cell migration on Col I coated PAGs[36]. Using a similar parameter set as our previous study, we re-simulated the effect of substrate stiffness on cell migration and morphology, using N_c=7,500, (Figure 3.4A-D). As predicted previously, cell random motility coefficient, area and aspect ratio all exhibit an optimal stiffness. To test whether CD44-dependent cell migration and morphology also exhibit an optimal stiffness, we measured cell migration, spreading and aspect ratio on IM7-coated PAGs of varying Young's modulus. Similar to integrin-dependent migration on Col I coated PAGs, U251 cells exhibit a stiffness sensitive cell migration, spreading and polarization. Figure 3.4E and F show representative phase contrast images and wind-rose trajectories on four different stiffnesses (0.7, 9.3, 98.5 and 195 kPa). Quantification of cell migration shows a stiffness sensitive cell migration with an optimal stiffness between 9.3 and 100 kPa with a modest decrease at 19.5kPa (Figure 3.4G). Furthermore, cell area and aspect ratio exhibit an optimal stiffness at ~98.5 kPa (Figure 3.4H and I). Together, these results show cell migration and morphology are dependent on substrate stiffness in a manner consistent with predictions from the cell migration simulator.

3.3.5 CD44-mediated traction force is stiffness sensitive and exhibits an optimum

Integrin-mediated traction force is stiffness sensitive[24,27,32,36,109–112]. The motor-clutch model predicts a biphasic traction force as a function of substrate stiffness which have been demonstrated experimentally[24,32,34,36]. In addition, due to adhesion reinforcement through talin, an adapter protein which unfold under force and exposes cryptic binding sites enabling vinculin binding and adhesion reinforcement, a monotonic increase in force transmission has been reported using the motor-clutch model [32]. As previously shown, the CMS predict a biphasic traction force as a function of substrate stiffness (Figure 3.5A). To assess whether U251 cells would exhibit a biphasic or monotonic force transmission on IM7 coated PAGs, we measured traction strain energy across different stiffnesses. Similar to force transmission on Col I coated PAGs, U251 cells exhibit a peak traction strain energy at 9.3kPa, p=0.006 (Figure 3.5B). Figure 3.5C-E show representative phase contrast images and traction heatmaps across different stiffness. The results are consistent with CD44 functioning as a molecular clutch without a reinforcement mechanism in U251 cells.

3.3.6 U251 cells exhibit load and fail dynamics characteristic of a motor-clutch behavior

A motor-clutch mechanism of stiffness sensing predicted traction forces with load and fail dynamics on compliant substrates [24]. Such dynamics have

been observed for integrin-mediated traction forces [24,113,114]. Using the motor-clutch model, we simulated single protrusion dynamics at 1 and 3 pN/nm substrate stiffnesses and captured load and fail dynamics with failure cycle times of 5-25 seconds and 0.1-0.5 μm displacement amplitude (Figure 3.6A). To assess whether CD44-mediated traction forces exhibit such dynamics, we tracked individual embedded fluorescent beads positions to potentially observe predicted load and fail dynamics. Fluorescent beads were imaged every five seconds for a total five minutes. Figure 3.6B shows a kymograph displaying load and fail dynamics. Figure 3.6C shows a single bead's position tracking over time. Figure 3.6D-F show example single bead displacement plots. In these plots, load and fail dynamics on 100 μg/mL coated 4.6 kPa PAGs having failure cycles in 10s of seconds and displacement magnitude in the range of 0.1-0.7 μm can be observed.

3.4 Discussion

Activating invasion and metastasis is one of the hallmarks of cancer. In addition to the loss of cell-cell contact, expression of cell adhesion and ECM molecules is a key driver in cancer cell invasion and migration [63]. As one of the key classes of adhesion molecules interacting with ECM, integrins have been widely studied and the molecular details describing integrins' interactions with the ECM and the actin cytoskeleton have been extensively characterized. In addition to integrins, CD44 expression has been associated with cancer aggressiveness and the EMT [43–45,48,115]. In GBM, CD44 expression has been shown to correlate with glioma cell migration in a biphasic relationship with a peak migration rate at

intermediate expression level, which also correlated with the minimum in survival in both glioma animal models and human GBM [35]. Such relationship led to the hypothesis that CD44 can function as an adhesion molecule to regulate glioma cell migration. Here our results confirm CD44's ability to function as a molecular clutch to mediate stiffness and adhesion sensitive cell migration.

To our knowledge, there have been only a limited number of studies using HA-based hydrogels to demonstrate CD44-dependent cell adhesion and migration. Work from the Kumar group using HA-hydrogels demonstrates stiffness sensitive CD44-dependent cell spreading and migration [57,58]. While HA-hydrogels provide a practical, biologically relevant substrate to study CD44-dependent adhesion, they are limited in their ability to allow for traction force measurements to explore the biophysics of CD44-dependent mechanosensitive cell migration. In our study, the use of PAGs allowed for probing CD44-dependent cell migration in a wide range of stiffnesses (1→ 200kPa) and observing migration optimality as a function of substrate Young's modulus, previously inaccessible due to the limited stiffness-range of HA-hydrogels. Furthermore, we quantitatively established the ability of CD44 to transmit traction forces and stiffness and adhesion sensitive force transmission as predicted by a motor-clutch mechanism.

Overall, consistent with earlier work, our results clearly show the ability of CD44 to mediate cell migration and raise the prospect of targeting CD44 to slow cancer cell invasion. Given the optimality in cell migration in response to changes in adhesion (receptors or ligands), it is important to sufficiently inhibit CD44 to

avoid shifting cells from a too adhesive environment (slow migrating) to an optimal environment (fast migrating). Lastly, integrated approaches have been utilized to describe the mechanistic underpinning of mechanotransduction in the context of integrin-mediated adhesion[116]. Such approaches, including the use of molecular tension sensors, can help dissect the molecular mechanism and molecular component of CD44-mediated adhesion and force transmission and other adhesion system such as cadherins. This could unlock a new avenue to target cancer cell migration and limit tumor invasion. Overall, our results point to the highly conserved functional nature of CD44- and integrin-mediated adhesive clutch bonds in terms of migration, morphology, traction force, and traction dynamics, despite highly divergent sequences and structures.

3.5 Materials and Methods

Creation and maintenance of cell lines

Human glioma cell line U251 was originally obtained from Dr. G. Yancey Gillespie (UAB). These cells were previously authenticated using STR assay[36]. U251 cells were cultured using DMEMF12 (Gibco, Thermo Fischer Scientific, Waltham, MA) media containing 8% heat-inactivated fetal bovine serum (Gibco, Thermo Fischer Scientific, Waltham, MA) and 1% penicillin/streptomycin solution (Corning, Corning, NY). CD44 knockout was achieved using the CRISPR/Cas9 system. A guide RNA (gRNA) was created to target exon 2 in human cell lines (GAATACACCTGCAAAGCGGC). A co-transposition method, was used to enhance screening for knockout clones [117,118]. Cell were transfected with Cas9 nuclease, gRNA, PiggyBac transposases, and PiggyBac transposon plasmid containing puromycin selection. Cell were transfected using FuGENE (Promega, Madison, WI) following the manufacturer's protocol. Puromycin selection was performed and single cell clones were generated using serial dilution. Using flow cytometry, CD44KO and CD44WT single clones were identified by staining for CD44.

Casting and coating polyacrylamide hydrogels

Polyacrylamide hydrogels (PAGs) were cast onto No. 0 glass bottom 35 mm culture dishes (MatTek P35G-0-20-C) using a previously described method and formulation [36,96]. Two hundred nm crimson fluorospheres (Invitrogen, Carlsbad, CA) were added to the prepolymer mixture at 0.1% v/v to allow for traction force measurements. Cast gels were then coated using sulfo-SANPAH

(Thermo Fischer Scientific, Waltham, MA) as previously described [36,96]. In this study, Type I Collagen (354236, Corning, Corning, NY) or anti-CD44 antibody IM7 (BDB553131, BD Biosciences, San Jose, CA) or its control isotype (BDB559478, BD Biosciences, San Jose, CA) were used to coat PAGs. In general, 200 µg/mL Col I solution was used and 1—300 µg/mL IM7 solution was used depending on the experiment. In addition, 0.7, 4.6, 9.3, 19.8, 98.5, 195 kPa stiffnesses were used in this study.

Stochastic cell migration simulator and motor clutch model

The CMSv1.0 which was previously described was used to simulate cell migration dynamics in response to changes in adhesion density and substrate stiffness [35,36]. The number of clutches (N_c) was adjusted to model the amount of IM7 on the surface. Also substrate stiffness (κ_{sub}) was varied to model response to changes in substrate Young's modulus. Four hours of cell dynamics were simulated and the first hour was excluded from analysis to allow the system to reach steady state. Analysis was performed using a ten minute sampling interval as previously described [36].

The base motor-clutch model was used to simulate single protrusion force dynamics [24,34]. Parameters used in the simulation are presented in Table 3.S1. For load and fail dynamics, the motor-clutch model was used to simulate single protrusion. Substrate positions, sampled every five seconds for a total of five minutes, were used to create the plots in Figure 3.6A.

Single cell migration and morphology analysis

Before plating cells on PAGs, cells were labeled using NucBlue Live ReadyProbe (Thermo Fischer Scientific, Waltham, MA) to label cells' nuclei. Phase contrast and fluorescence images were taken using a plan fluor 10x/0.30NA objective at 10 minutes intervals for 6-8 hours. Cells were maintained at 37 °C and 5% CO_2 for the duration of imaging using an Oko lab Bold Line top stage incubator (Okolab, Ottaviano, Italy). Time-lapse movies were then analyzed using an ImageJ TrackMate plugin to track cell nuclei overtime. Single cell tracks were then extracted and analyzed using a modified, previously published MATLAB algorithm [36]. Using nucleus centroid coordinates, the mean squared displacement (MSD) of the cell trajectories over time was calculated using the time interval overlap method (Dickinson and Tranquillo, 1993) and the random motility coefficient μ was calculated according to the equation ($MSD(t)=4\mu t$; assuming 2-D geometry).

To calculate cell morphology, individual cell phase contrast images were segmented in MATLAB. Using the segmented region, cell area was then calculated, and an ellipse was fitted to the segmented region. Using the parameters from the fitted ellipse, cell aspect ratio was calculated as the ratio of the major and minor axes.

Traction force microscopy

To measure force transmission, Traction Force Microscopy (TFM) was performed as previously described [36]. Briefly, Nikon TiE or Ti2 microscopes were used to image fluorescent beads position within PAGs before and after cell detachment via trypsin. A Zyla 5.5 sCMOS camera (Andor Technology, Belfast, United Kingdom) and a 40x/0.95NA Ph2 lens with 1.5x zoom (60x total magnification, 110 nm spatial sampling) were used. Cells were maintained at 37 °C and 5% CO_2 for the duration of imaging using an Oko lab Bold Line top stage incubator (Okolab, Ottaviano, Italy). At each stage position, a phase contrast image of the cell was acquired. Next, an image of fluorescent beads at the top surface of the gel was captured using a 575/25 nm LED and eGFP/mCherry filter set with LED fluorescence illumination from a SpectraX Light Engine (Lumencor, Beaverton, OR). Media in dishes was carefully removed, cells were detached with 0.25% trypsin/EDTA (Corning, Corning, NY), and fluorescence images of beads in the absence of cells were acquired at saved stage positions.

Using a previously described method [36], the displacement field was determined using particle image velocimetry (PIV) using the before and after bead images. A window size of 80-pixels (8.8 µm) square was used in PIV and a final lattice spacing of 20 pixels (2.2 µm) was achieved. Stress and displacement vectors were obtained by solving the inverse Boussinesq problem in Fourier space [82]. By integrating the product of the stress and displacement vectors over the entire image, substrate strain energy was determined as previously described [36].

Load and fail dynamics measurements

To measure load and fail dynamics, time-lapse imaging of cells adhered on PAGs embedded with fluorescent beads was performed. Using a 40x/0.95NA Ph2 lens with 1.5x zoom (60x total magnification, 110 nm spatial sampling) phase contrast image of the cell and fluorescent image of the crimson beads were taken every five seconds for a total of five minutes. Nikon NIS element software (Nikon, Melville, NY) was used to align the time-lapse images to correct for any stage drift. Then fluorescent beads within region of interests were tracked using ImageJ TrackMate plugin. X and y coordinates from individual beads were then extracted and used to plot bead displacement over time shown in Figure 3.4D-F.

Statistical analysis

For statistical analysis, Kruskal-Wallis one-way analysis of variance was used. Where appropriate, a subsequent Dunn’s test for multiple comparisons was performed to compare across multiple conditions.

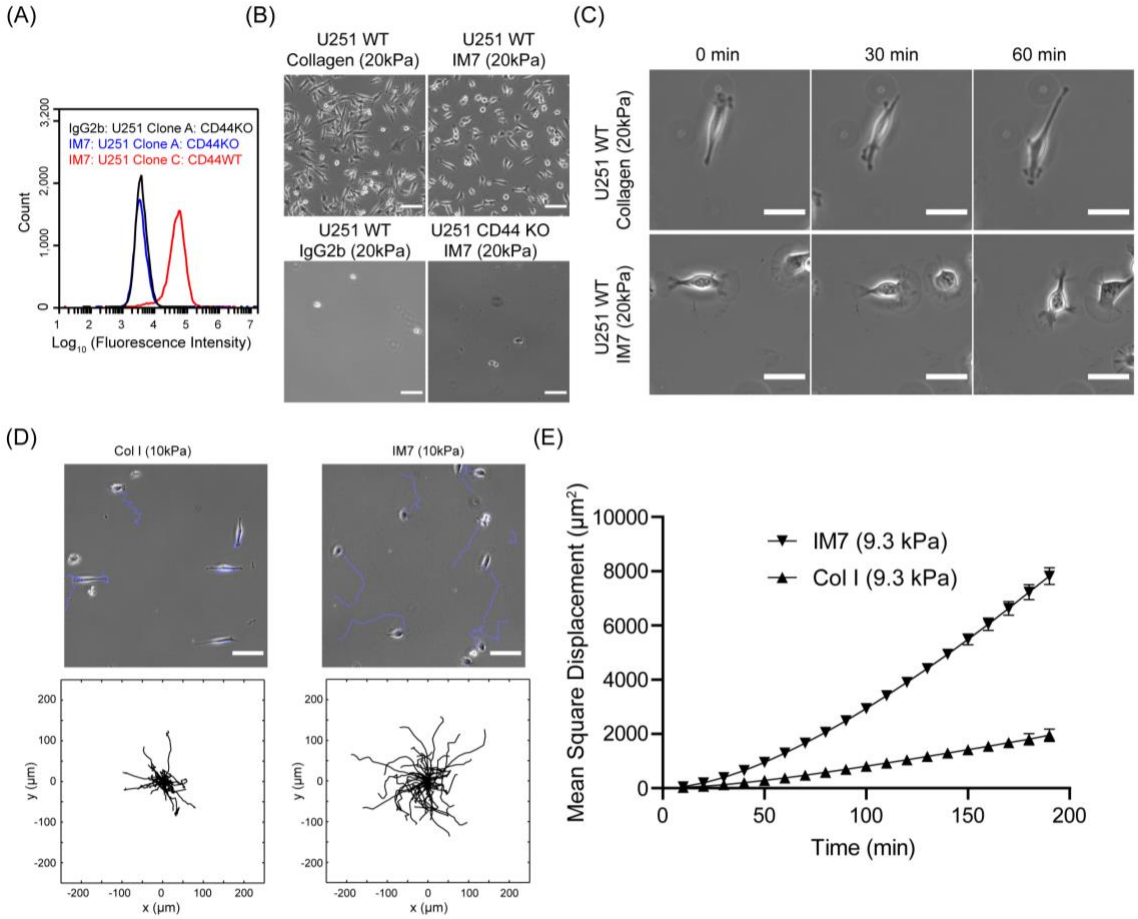

Figure 3.1. CD44-dependent adhesion and migration on compliant polyacrylamide hydrogels.

A) Flow cytometry staining results demonstrating the successful generation of a CD44KO single cell clone. B) Phase contrast images showing U251 cells adhesion on Col I, IM7 and IgG2b coated PAGs. Scale bar is 100 μm. C) Phase contrast images montages showing a migrating U251 cell on Col I and IM7 coated PAGs. Scale bar is 20 μm. D) Representative phase contrast images with cell tracks superimposed and wind-rose plots of cell trajectories on Col I and IM7 coated PAGs. 50 randomly selected cell trajectories 6 hours long each. Scale bar is 100 μm. E) MSD vs. time plot of migrating U251 cells on Col I and IM7 coated PAGs.

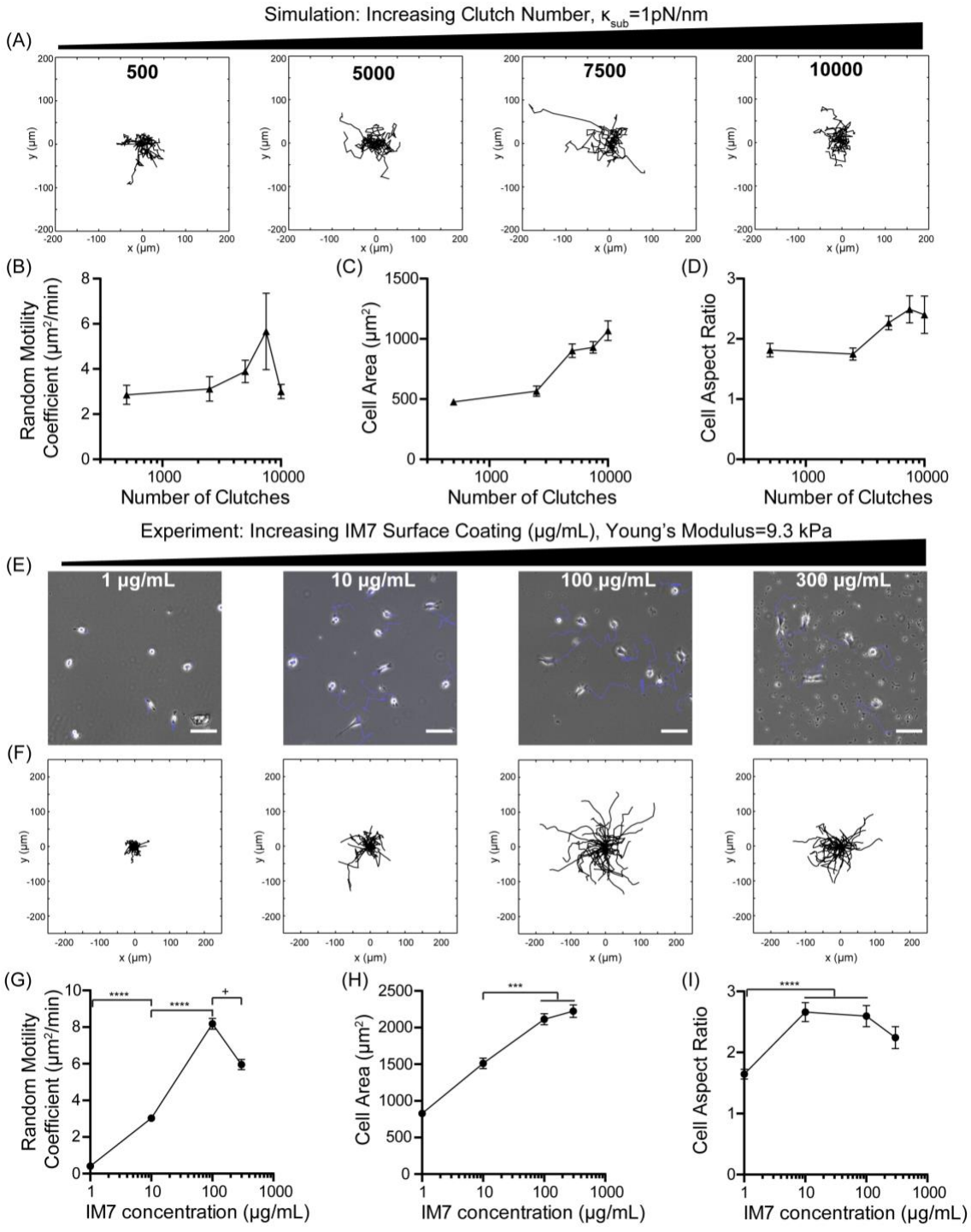
Simulation: Increasing Clutch Number, κsub=1pN/nm
(A)
500
5000
7500
10000
y (μm)
x (μm)
(B)
Random Motility Coefficient (μm²/min)
Number of Clutches
(C)
Cell Area (μm²)
Number of Clutches
(D)
Cell Aspect Ratio
Number of Clutches
Experiment: Increasing IM7 Surface Coating (μg/mL), Young's Modulus=9.3 kPa
(E)
1 μg/mL
10 μg/mL
100 μg/mL
300 μg/mL
(F)
y (μm)
x (μm)
(G)
Random Motility Coefficient (μm²/min)
****
****
+
IM7 concentration (μg/mL)
(H)
Cell Area (μm²)
***
IM7 concentration (μg/mL)
(I)
Cell Aspect Ratio
****
IM7 concentration (μg/mL)

Figure 3.2. Cell migration and morphology are dependent on substrate adhesivity as predicted by the cell migration simulator.

A-D) Simulations results varying the clutch number. A) Representative wind-rose plot of cell trajectories. Fifteen randomly selected trajectories 3 hours long each. B) Quantification of cell migration represented by the random motility coefficient which shows an optimal adhesion for cell migration. C and D) Quantification of cell area and aspect ratio. E-I) Experiment results across different coating densities. E) Representative phase contrast images superimposed with cell trajectories showing cell morphology. Scale bar is 100 μm. F) Representative wind-rose plots of cell trajectories. Fifty randomly selected cell trajectories 6 hours long each. G) Quantification of cell migration displaying an optimum cell migration on 100 μg/mL coated PAGs. H and I) Quantification of cell area and aspect ratio. Error bars are S.E.M. +$p < 0.05$ * $p < 0.01$, ** $p < 0.001$.

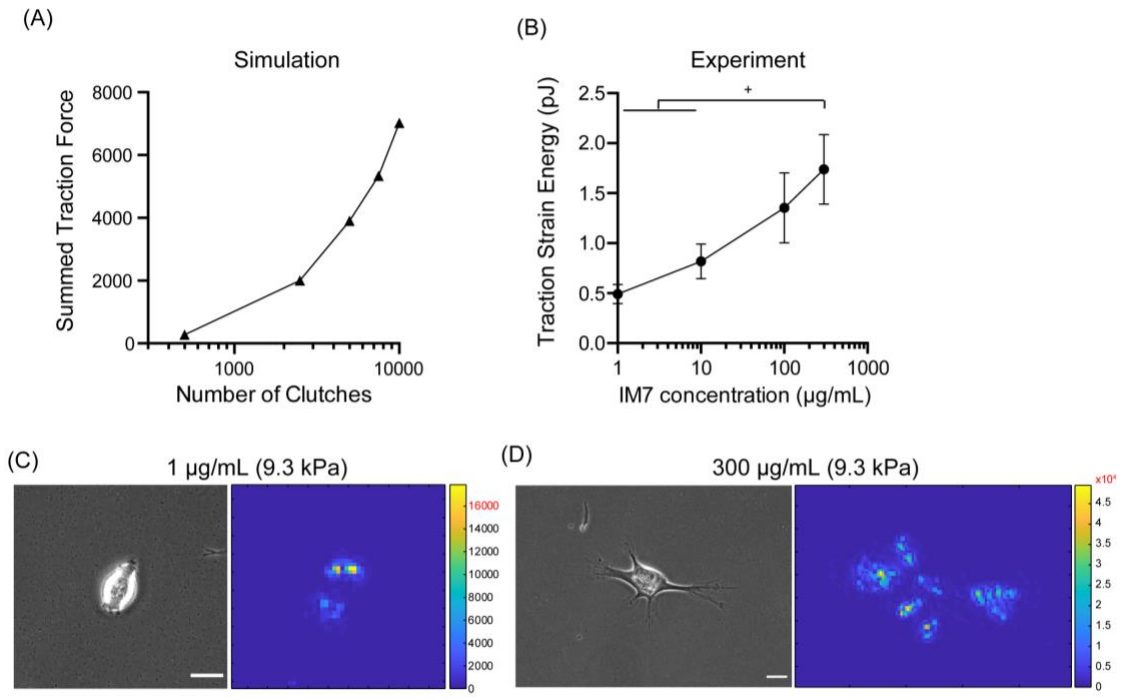

Figure 3.3. Traction strain energy is dependent on substrate adhesivity as predicted by the cell migration simulator.

A) Summed traction forces measurements of simulated cells on different amount of adhesion. B) U251 traction strain energy increases monotonically with increase IM7 coating. C and D) Representative phase contrast and traction heatmaps on 1 and 300 µg/mL IM7 coated PAGs (9.3 kPa). Scale bar is 20 µm. Error bars are S.E.M. +p <0.05 * p <0.01, ** p<0.001.

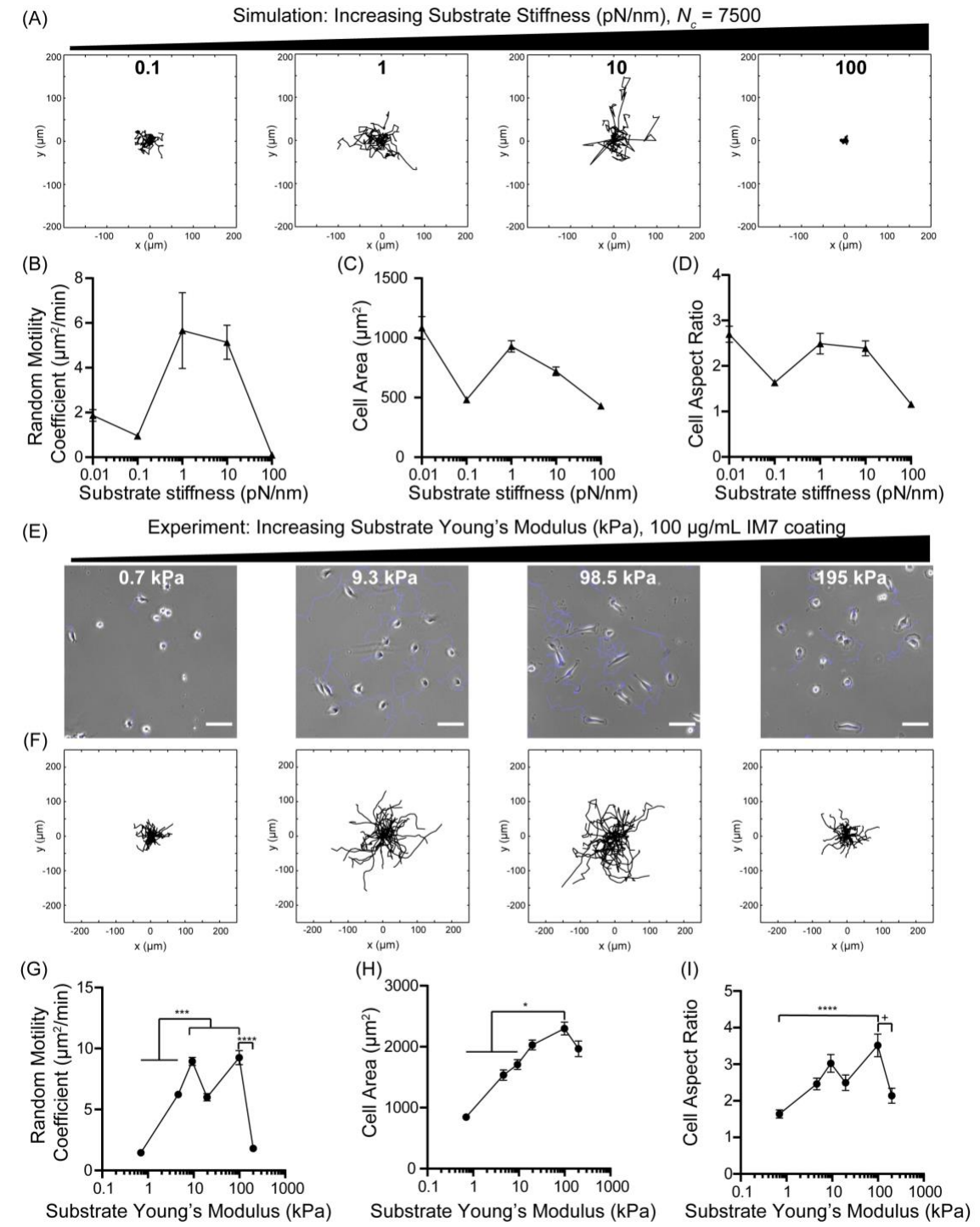
(A)
Simulation: Increasing Substrate Stiffness (pN/nm), N_c = 7500
0.1
1
10
100
y (μm)
x (μm)
(B)
Random Motility Coefficient (μm²/min)
Substrate stiffness (pN/nm)
(C)
Cell Area (μm²)
Substrate stiffness (pN/nm)
(D)
Cell Aspect Ratio
Substrate stiffness (pN/nm)
(E)
Experiment: Increasing Substrate Young's Modulus (kPa), 100 μg/mL IM7 coating
0.7 kPa
9.3 kPa
98.5 kPa
195 kPa
(F)
y (μm)
x (μm)
(G)
Random Motility Coefficient (μm²/min)
Substrate Young's Modulus (kPa)
(H)
Cell Area (μm²)
Substrate Young's Modulus (kPa)
(I)
Cell Aspect Ratio
Substrate Young's Modulus (kPa)

Figure 3.4. Cell migration and morphology is stiffness sensitive.

A-D) Simulation results varying the substrate stiffness and using N_c=7,500. A) Representative wind-rose plot of cell trajectories. Fifteen randomly selected trajectories 3 hours long each. B) Quantification of cell migration represented by the random motility coefficient which shows an optimal stiffness for cell migration. C and D) Quantification of cell area and aspect ratio which also show biphasic dependency on substrate stiffness. E-I) Experimental results across different substrate Young's modulus on 100 µg/mL IM7 coated PAGs. E) Representative phase contrast images superimposed with cell trajectory showing cell morphology. Scale bar is 100 µm. F) Representative wind-rose plots of cell trajectories. Fifty randomly selected cell trajectories 6 hours long each. G) Quantification of cell migration displaying an optimum cell migration between 4.6 kPa and 200 kPa. H and I) Quantification of cell area and aspect ratio which exhibit a peak at 100kPa. Error bars are S.E.M. +$p < 0.05$ * $p < 0.01$, ** $p<0.001$.

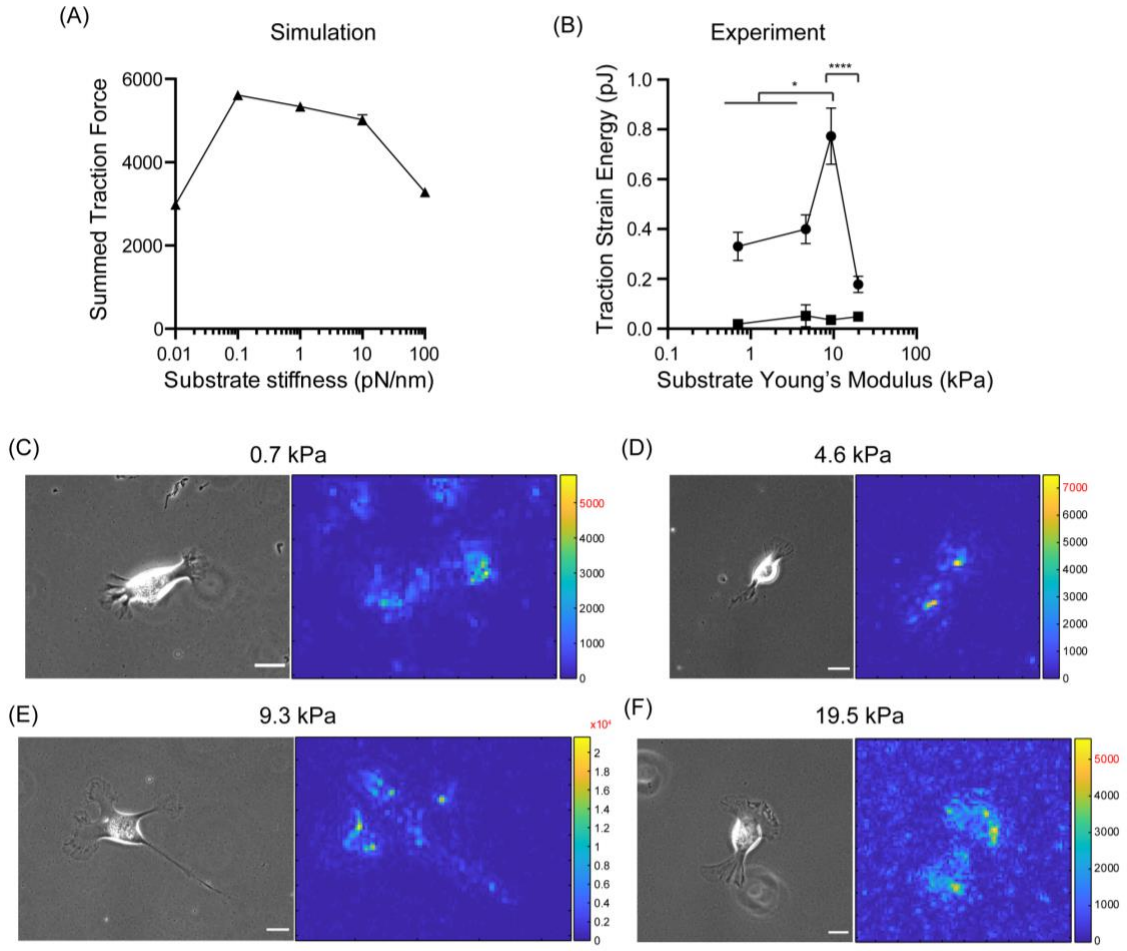

Figure 3.5. Traction force is biphasically dependent on substrate stiffness as predicted by the cell migration simulator.

A) Summed traction forces measurements of simulated cells on different stiffnesses. B) U251 traction strain energy exhibits an optimal stiffness for force transmission. C-F) Representative phase contrast and traction heatmaps on 0.7, 4.7, 9.3 and 19.5 kPa, respectively and coated with 100 µm/mL. Scale bar is 20 µm. Error bars are S.E.M. +p <0.05 * p <0.01, ** p<0.001.

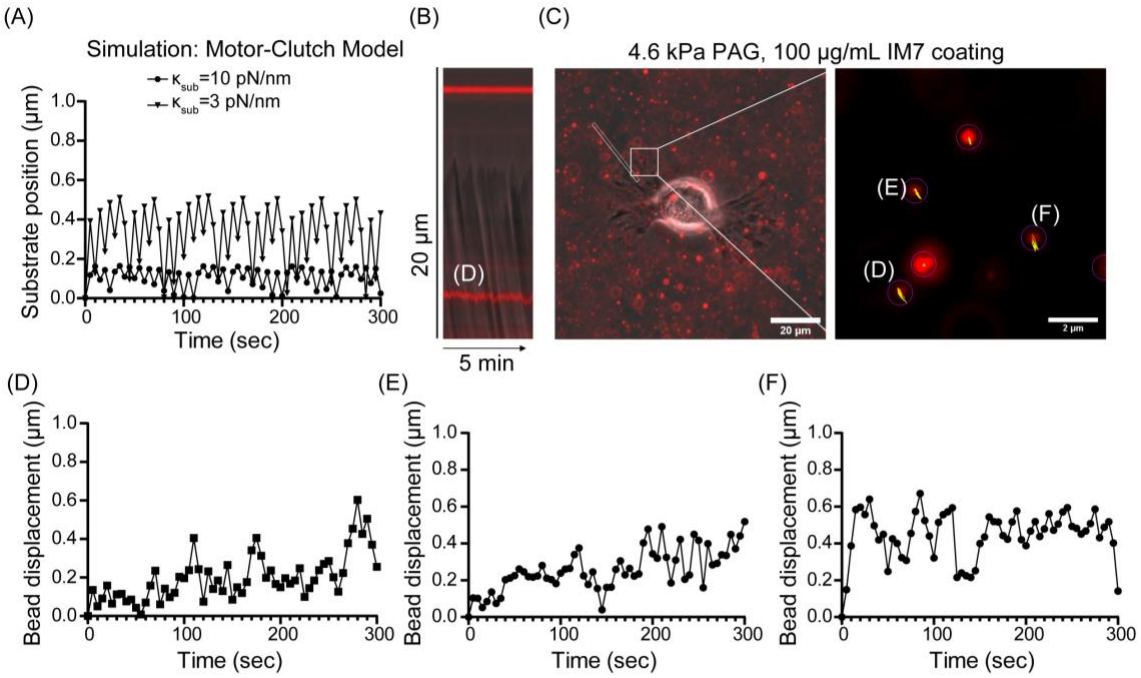

Figure 3.6. U251 cells exhibit substrate load and fail dynamics on compliant substrates.

A) Single protrusion dynamics as predicted by the motor clutch model. B) Kymograph of substrate-embedded 200 nm red fluorescent beads under U251 cells exhibiting load and fail dynamics. C) An image showing an adherent cell on a PAG embedded with fluorescent beads. Image at right represents the output from single bead tracking. D-F) Example bead displacement vs. time plots showing load and fail dynamics.

Table 3.S1: Motor-clutch model parameters values

Symbol	Parameter	Value
n_m*	Number of motors	1,000
F_m	Motor stall force	2 pN
v_m*	Unloaded motor velocity	120 nm/s
n_c*	Maximum number of module clutches	750
k_{on}	Clutch on-rate	1 s^{-1}
k_{off}*	Clutch unloaded off-rate	0.1 s^{-1}
κ_c	Clutch spring constant	0.8 pN/nm
F_b	Characteristic clutch rupture force	2 pN
κ_s	Substrate spring constant	1, 3 pN/nm

Chapter 4

Emerging Technologies in mechanotransduction research

*Chapter 4 contains work by **Shamsan, G.A**., and Odde D.J., Current Opinion in Chemical Biology (Edited by Yan Jie and Terence Strick), Accepted*

Ghaidan A. Shamsan[1] and David J. Odde[1]
[1] Department of Biomedical Engineering, University of Minnesota, Minneapolis, MN 55455, USA

4.1 Summary

Mechanotransduction research focuses on understanding how cells sense and respond to mechanical stimuli by converting mechanical signals into biochemical and biological responses. Cells have been shown to respond to mechanical stimuli through specialized biological machinery such as adhesion complexes. Research in the last two decades helped identified key components of cellular mechanotransduction. In recent years, integrated approaches, which are highlighted here, are emerging to provide new insights into the mechanistic and theoretical underpinnings of mechanotransduction. In particular, mathematical modeling has helped elucidate the mechanism underlining ligand spacing and distribution sensing, as well as sensing viscoelastic properties of the extracellular matrix. In addition, molecular tension sensors have helped dissect the forces involved in mechanotransduction at high spatial and temporal resolutions.

4.2 Introduction

The extracellular matrix (ECM) plays a critical role in many cellular functions including cell proliferation, migration, and differentiation[119]. The ability of cells to sense and respond to changes in their microenvironment is essential for maintaining cellular function and tissue homeostasis[101]. Decades of research have expanded our understanding of cells' ability to sense their physical environment and respond by triggering downstream events. The ability of cells to convert mechanical signals into biochemical and behavioral responses is known as mechanotransduction[120]. Cells use physical forces to probe and remodel their

physical environment[121,122]. Changes in the mechanics of the environment lead to changes in force transmission which then trigger downstream events[123]. Part of cells' ability to respond to the mechanics of their environment requires cells' ability to generate and transmit forces. This requires physical cell-ECM and cell-cell interactions through specialized transmembrane proteins such as integrins and cadherins.

In recent years, integrated approaches are emerging to provide new insights into the mechanistic and theoretical underpinnings of mechanotransduction. This includes the use of physics-based mathematical-computational modeling, advanced molecular and imaging tools, and advanced fabrication techniques. In this article, we highlight the recent impact of mathematical-computational modeling and the development of molecular tension sensors in aiding our mechanistic understanding of mechanotransduction. *We contend that integrating mathematical-computational modeling with molecular-scale force measurements will significantly advance our understanding of the mechanisms of mechanotransduction.*

4.3 Mathematical modeling in mechanotransduction

Mathematical and computational modeling provides the ability to integrate knowledge and to explain and predict non-intuitive behaviors both qualitatively and quantitatively. Computational modeling has enabled engineers and scientists to address complex questions and design sophisticated experiments to help understand multifaceted processes, especially where closed form analytical solutions are difficult or impossible to obtain. In mechanotransduction, modeling

has helped us describe how cells transmit forces and respond to the mechanical and biochemical properties of the microenvironment. This includes cells' ability to sense the substrate elastic and viscoelastic properties[30,109,124] as well as to sense ligand density and distribution[28]. Many models of mechanotransduction have relied on the molecular clutch hypothesis which describes how cells transmit forces, generated by the actomyosin interaction and actin polymerization, to the outside environment through plasma membrane-spanning adhesion molecules, such as integrins, termed "molecular clutches"[25]. Based on the molecular clutch hypothesis, the motor-clutch model was developed to explain the theoretical mechanism by which cellular protrusions transmit contractile forces and respond to the stiffness of their microenvironment (Figure 4.1A)[24]. In the motor-clutch model, molecular motors transmit forces to the external environment through rigid actin filaments and compliant transmembrane molecular clutches[24,34]. Importantly, the force generation is provided by myosin molecular motors and/or F-actin polymerization against the plasma membrane, both of which obey a force-velocity relationship. The consequence of the force-velocity relationship is that when a cell is pulling on soft environments, it takes longer time to reach a high traction force than when a cell is pulling on a stiff environment, which becomes a key determinant of stiffness sensing (Figure 4.1B and 4.1C)[34,107]. In recent years, the framework of the motor-clutch model has been adapted to investigate key aspects of mechanotransduction including rigidity sensing, adhesion reinforcement, viscoelasticity sensing, and ligand density and distribution[27–32,35,36].

The stiffness of the environment has been shown to control cellular force transmission, migration, differentiation, and cancer progression[125]. The use of mathematical modeling provided a mechanical mechanism by which force transmission is controlled by the stiffness of the environment. In the original framework of the motor-clutch model, stiffness regulation of adhesion binding dynamics elicits a biphasic force transmission and F-actin retrograde flow as a function of substrate stiffness[24]. Further parameter space analyses and experimental validation demonstrated mechanisms regulating mechanosensitivity and the determinant of optimal stiffness[34,36]. Despite the biphasic force transmission predicted in the model, monotonic force transmission as a function of substrate stiffness was being reported in the literature, which was not predicted in the motor-clutch model[126]. However, we note that the observation of a monotonically increasing traction force as a function of substrate stiffness is consistent with a biphasic prediction, assuming the optimal stiffness is above the highest stiffness measured in the experiment. In recent work, Elosegui-Artola *et al.* incorporated a switch-like mechanosensitivity regulation to model adhesion reinforcement through talin[32], which has been shown to unfold under force and expose cryptic binding sites to vinculin[127]. Talin mechano-response was modeled by recruiting additional clutches to the site of adhesion after surpassing a threshold force. As a result, a monotonic force transmission as a function of stiffness was predicted in the model[32]. Indeed, in cells expressing talin, increasing stiffness results in monotonically increasing force transmission, but

when talin is knocked-out a biphasic stiffness-force transmission relationship is restored as predicted in the base motor-clutch model[24,32].

In addition to responding to substrate rigidity, cells sense and respond to substrate stress relaxation (substrate viscoelasticity)[30,124]. Indeed, living tissues and reconstituted extracellular matrices were shown to exhibit stress relaxation property[128]. Like substrate Young's modulus, substrate stress relaxation enhances cell spreading[30], and regulates stem cell fate[129]. Recently, Gong *et al.* applied Monte Carlo and analytical methods to simulate cell spreading in response to substrate viscosity to explore the mechanism of substrate viscosity sensing[29]. Using the motor-clutch model framework and a standard linear viscoelastic model to describe the substrate, they explored the effect of different material properties (viscosity and elasticity) on cell spreading. They identified an optimal substrate viscosity at which cell spreading is maximum that is determined by the ratio of clutch binding and substrate relaxation timescales. Their finding suggests that substrate viscosity stiffens soft substrates to enhance clutch engagement and cell spreading by balancing substrate relaxation and clutch binding timescales. Using elastic and viscoelastic materials, they were able to show an increase in cell spreading in response to viscosity. In this work, computational modeling again informed the design of more sophisticated experiments to help understand the role of substrate viscoelastic properties on cellular spreading and function.

Mathematical modeling has also had an impact in predicting the cellular response to ligand density and distribution. Ligand density has been shown to control cell migration speed *in vitro*, *in vivo*, and *in silico* using computation modeling[22,23,35]. Oria *et al.* investigated cells' ability to sense ligand spacing utilizing advanced fabrication techniques and mathematical modeling[28]. They found ligand spacing and distribution control adhesion's growth and collapse, which ultimately affected YAP nuclear localization[28]. At low substrate stiffness, increasing ligand spacing promoted the growth of focal adhesions, but led to adhesion collapse on rigid substrates. They were able to explain the observed behavior using a molecular-clutch mechanism. In their model, the spacing of ligands was incorporated and neighboring ligands were linked together using elastic springs. The model predicted that increasing ligand spacing would promote adhesion growth by increasing the likelihood of reaching a threshold force which leads to integrin recruitments and adhesion growth. As stiffness continues to increase, forces continue to increase leading to the unbinding of clutches and adhesion collapse. When ligand spacing is low, forces are distributed across more ligands, reducing the likelihood of reaching the threshold force on low substrate stiffness. Simply put, increasing the spacing of ligand reduces the force needed to cross the threshold force per integrin needed for adhesion recruitment. This leads to a shift in the stiffness at which adhesion recruitment occurs. Having a computational model capable of explaining the experimental results, allowed the authors to model different perturbations and design new experiments to further characterize the molecular components that

control the cell's ability to sense ligand spacing. Highlighting the value of the model in predicting non-intuitive behavior, the model predicted a biphasic response to contractility inhibition on a rigid substrate. As predicted, a low dose of blebbistatin *increased* adhesion length by preventing adhesion collapse but a higher dose didn't alter adhesion length because it prevented adhesion reinforcement and adhesion growth[28]. Such counterintuitive predictions and experimental validations both build our confidence in the models and provide fundamental new insights.

4.4 Molecular tension sensors in mechanotransduction

Various methods have been developed to quantify forces on individual adhesion bonds involved in mechanotransduction; including single-molecule force spectroscopy, traction force microscopy, and molecular tension sensors; these methods are reviewed in depth by Roca-Cusachs *et al*[122]. In this section, we highlight the impact of molecular tension sensors in mechanotransduction. Molecular tension sensors were developed to measure nanometers-scale displacements caused by mechanical tension within load-bearing proteins. Most of the tension probes utilize Förster Resonance Energy Transfer (FRET) to measure the distance between two fluorophores (donor and acceptor) separated by a mechanically characterized linker[130,131]. This allows for molecular tension measurements using light microscopy. FRET-based molecular tension sensors have been applied to study mechanotransduction by either genetically encoding the tension sensor within the protein of interest[131–134] or by immobilizing it on the substrate on the molecule supporting cell adhesion (Figure 4.2)[135,136].

The first genetically encoded tension sensor was developed by Grashoff *et al.* where they designed a tension sensor module (TSMod) consisting of two fluorophores (mTFP-1 and Venus(A206K)) linked by a 40-amino-acid-long linker that acts like an elastic spring[131]. Using their tension sensor module, they were able to measure mechanical tension across vinculin, a protein which connects the F-actin filaments to integrins, i.e. a so-called “adaptor” protein critical to the molecular clutch bonds that mediate cell adhesion to the environment. Using their FRET-based tension sensor they showed that during adhesion growth and assembly tension across vinculin is highest. Furthermore, using fluorescent lifetime imaging, they reported that individual vinculin molecules experience an average force of 2.5 pN.

FRET-based tension sensors have been used to measure tension across proteins involved in mechanotransduction. In a recent study, Ringer *et al*., developed a FRET-based tension sensor module with switch-like behavior and increased sensitivity at 3-5pN[137]. Using their improved tension sensor module, they sought to measure intramolecular force within talin-1. By placing their tension sensor modules at different locations within the talin-1 rod domain, they identified a vinculin-dependent tension gradient within the rod domain of talin-1. They reported higher tension closer to the head domain (N-terminal), low tension in between actin-binding domains (C-terminal), and lack of any forces at the C-terminal end of talin-1. This demonstrates that higher forces are exerted at the N-terminal part of the talin rod domain, presumably due to the presence of vinculin

binding sites which provide an extra mechanical linkage that distribute load to the F-actin cytoskeleton. Due to switch-like behavior of their tension sensor module, they were able to calculate the fraction of talin molecules under tension and showed that close to 70% of talin molecules are under tension at the N-terminal end of the rod domain and only 40% are under tension at the C-terminal end of the rod domain. Their work also provided a new sensor design utilizing two different pairs of fluorophores, which allows for simultaneous measurement of tension on two different proteins.

Previous designs of FRET-based tension sensors were limited in the range of forces detected (i.e. pNs) and relied on tension sensor calibrations using purified proteins[131]. In more recent advances in FRET-based molecular tension probes, LaCroix *et al.* developed tunable peptide designs with wider ranges of force magnitude sensitivity[134]. Their new designs use biophysical modeling to more accurately calibrate the tension probe using peptide length and avoid the extensive calibration normally needed. Using their new design and method, they developed an optimized tension sensor module and detected a force gradient within focal adhesions by measuring forces across vinculin. In addition, using tension sensors with distinct mechanical sensitivities and lengths, they demonstrated an extension-based control of vinculin loading. Having developed these tension sensors allowed them to explore extension- vs. force-based control of force loading. They showed, in the presence of tension sensors with different mechanical properties, cells were able to maintain extension by adjusting forces applied on vinculin. This result highlights the power of molecular tension sensors

in dissecting mechanisms of mechanotransduction across proteins and highlighted cells' ability to control protein extension.

In addition to genetically encoded tension sensors, immobilized FRET-based and DNA-hairpin tension sensors on a substrate have greatly informed our understanding of mechanotransduction and force transmission across adhesions. These sensors enabled the measurements of forces on individual integrins at the cell-ECM interface. Using immobilized FRET-based tension sensors, the majority of ligand-bound integrins were shown to exert forces in the range of 1-7pN[136]. While this range is lower than reported forces using fluorescent DNA hairpins of known unfolding force[138], it is possible that DNA unfolding sensors measure maximum force over some time interval while the FRET-based sensors measure mean force within their range of force sensitivity. Overall, both immobilized and genetically encoded molecular tension sensors enabled single molecule and submolecular tension measurements at high temporal resolution, which could help inform and validate current models. In addition, genetically encoded tension sensors open the possibility to measure subcellular structure forces *in vivo* and *ex vivo*[139] and with higher sensitivity we will potentially be able to overcome some of the challenges of *in vivo* force measurements using FRET-based tension sensors[140,141].

4.5 Conclusion

The highlighted recent body of work shows the added value that modeling and molecular tension sensors have provided in our mechanistic understanding of mechanotransduction. Going forward it will be important to continue to

incorporate these technologies to improve our mechanistic understanding and to further investigate the emerging behaviors predicted by experimentally-validated computational models. Furthermore, the current state of mechanotransduction research presents the opportunity to apply the current models and molecular tension sensors to other systems beyond integrin-mediated adhesions to include, for example, to investigate CD44-mediated adhesions and cell-cell adhesions through cadherins.

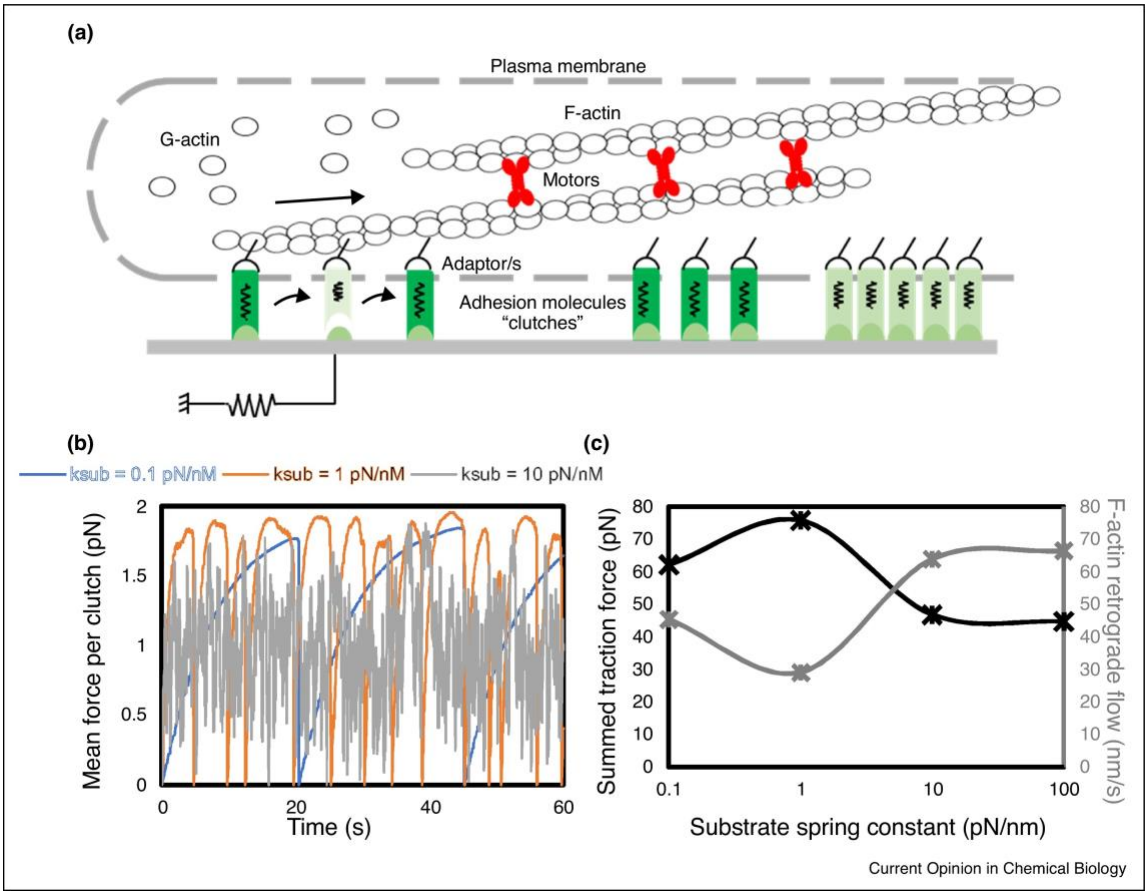

Figure 4.1. The motor-clutch model of force transmission.

(a) A schematic of the motor clutch model illustrating force transmission on a linear elastic substrate. (b) and (c) Output of motor-clutch model simulations showing the effect of substrate stiffness (κ_{sub}) on clutch force dynamic, summed traction forces, and F-actin retrograde flow.

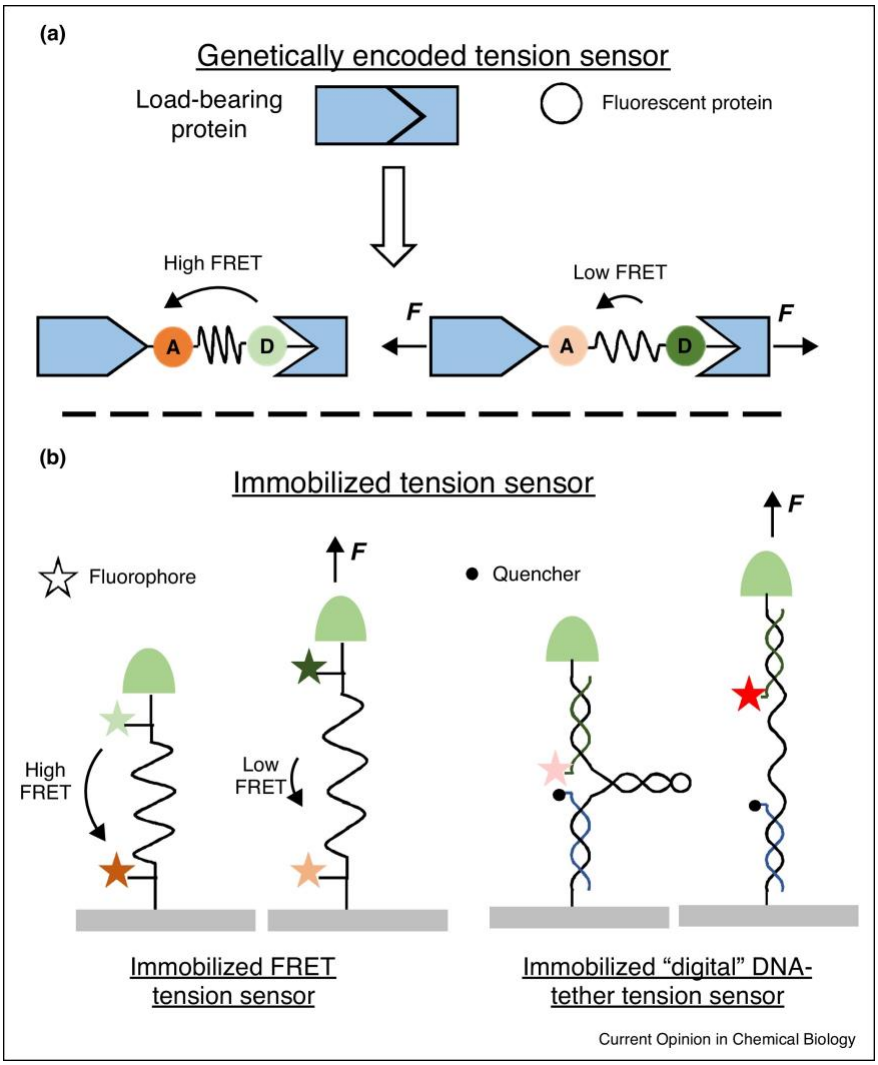

Figure 4.2. Commonly used molecular tension sensor designs.

(a) a schematic of a genetically encoded tension sensor utilizing FRET, A: acceptor, D: donor. (b) schematics of two immobilized tension sensor designs, one a FRET-based tension sensor, and the other a DNA-tether tension sensor with proximity-based fluorescence quenching

Chapter 5

Conclusions and future directions

In this dissertation, our goal was to better our understanding of the mechanics of glioblastoma cancer cell migration. Because of the critical role cancer cell migration plays in glioblastoma progression, it was essential to understand how cancer cell infiltrate healthy brain tissue and propose therapeutic strategies to slow/stop disease progression.

In Chapter 2, we developed mouse tumor models to test the hypothesis that glioma cell migration is a key characteristic of glioblastoma molecular subtypes. Using NRAS- and PDGF- driven mouse brain tumors, we demonstrated, as predicted by our cell migration simulator, mesenchymal tumor cells are more migratory, polarized and generate larger forces. Our finding was consistent with an epithelial-to-mesenchymal transition (EMT) phenotype associated with increased CD44 expression in mesenchymal tumors relative to proneural tumors[31]. Furthermore, despite the increased cancer cell migration and an EMT-like phenotype, NRAS/Mesenchymal tumors grew slower and had enhanced immune response. Elevated immune response in mesenchymal tumors have been reported [16,17,72]. The enhanced immune signature detected in our transcriptomic data was associated with immune-mediated tumor cell killing. The presence of the immune response provides a mechanism by which survival is extended in NRAS/Mesenchymal tumors despite their enhanced migration relative to PDGF/Proneural tumors. Furthermore, we showed glioblastoma cancer cell migration and immune-mediated cell killing counteract each other

which may explain the lack of a strong survival difference between subtypes clinically, while also opening up new opportunities for subtype-specific therapies, especially those subtypes linked to EMT.

While our results in Chapter 2 point to CD44 expression as a possible mechanism driving enhanced cell migration in mesenchymal tumors, direct testing of the role of CD44 is still needed. Going forward, targeting CD44 using shRNA or CRISPR/Cas9 in NRAS/Mesenchymal tumors can be used to confirm the role of CD44 in glioma cell migration. We predict knocking down or knocking out CD44 in mesenchymal tumor or mesenchymal PDX lines would lead to reduced cell migration and improved survival outcome in mice. Furthermore, the therapeutic potential of targeting CD44 can be tested by treating animals using anti-CD44 antibody. These studies can be done using genetically induced mouse tumor models or syngeneic injections using isolated tumor lines developed in Chapter 2. In addition, to investigating the anti-tumoral immune response observed in NRAS/Mesenchymal tumors, orthotopic injections of mesenchymal and proneural mouse primary lines can be used to inject immunocompromised. Unlike the survival difference observed in genetically induced models, where NRAS/Mesenchymal has better survival outcome, we predict NRAS/Mesenchymal injected mice to have similar or worst survival than PDGF/Proneural injected mice. The predicted lower survival is attributed to NRAS/Mesenchymal enhanced cancer cell migration.

Therapeutically, since our genetically induced mouse models recapitulate key features of human glioblastomas including transcriptomic changes, cell

migration and immune microenvironment, standard of care therapies could be applied to understand tumor response to radiation and chemotherapy (TMZ). In addition, since NRAS/Mesenchymal tumors are immunologically ‘hot’ and PDGF/PN are immunologically ‘cold’, a stratification strategy can be test on our mouse models where NRAS/Mesenchymal tumors are treated with immune-checkpoint blockage, to overcome immune suppression, and PDGF/Proneural tumors are treated using oncolytic viral therapy to help induce immune cell infiltration.

CD44 expression levels have been shown to correlate with glioblastoma cancer cell migration and survival in a biphasic dependency [35]. Our work in Chapter 2 also suggests CD44 functions as an adhesion molecule to support glioblastoma cancer cell migration. In Chapter 3, we tested the hypothesis that CD44 is able to support cell migration and force transmission similar to integrin-dependent adhesions. Using immobilized anti-CD44 antibody, we confirmed that CD44 is capable of supporting cell migration and force transmission in agreement with a motor-clutch mechanism. CD44-dependent cell morphology, migration and force transmission was found to be responsive to changes in adhesion density and substrate stiffness. This highlights a key similarity between integrin-dependent and CD44-dependent adhesion, migration and force transmission.

Going forward, CD44-dependent migration behavior of patients derived cells, on IM7 coated hydrogels, could be investigated and correlated with CD44 expression. We expect a biphasic relationship between cell migration and CD44

expression levels. Unlike integrin-dependent adhesions, CD44 molecular clutch components linking CD44 intracellular domain to the cytoskeleton have not been characterized. Knock down experiments of known adapter protein for CD44 could help identify the key player in CD44-dependent adhesion. In parallel, using CD44 knockout cell line developed in Chapter 3, a rescue CD44 cDNA construct can be introduced with different truncations to investigate the mechanical consequence of perturbing CD44 interactions with the actin cytoskeleton. Molecular tension sensors can be designed and used to probe the forces involved in CD44-dependent adhesions at the molecular level[116]. Finally, in Chapter 4 of this dissertation, I am presenting a review of emerging technologies in mechanotransduction research. These technologies are highly applicable to studying CD44-mediated adhesion, migration and force transmission.

Overall, in addition to advancing our current understanding of the mechanics of glioma cell migration, this dissertation provides a framework to study cancer progression using multidisciplinary approaches including genetic modeling, optical imaging, and mathematical modeling. In addition, this dissertation describes a method for studying CD44-dependent migration that can be readily adapted to exploring any adhesion molecule of interest.

Bibliography

1. Omuro, A. & DeAngelis, L. M. Glioblastoma and other malignant gliomas: A clinical review. *JAMA - Journal of the American Medical Association* vol. 310 1842–1850 (2013).
2. Dolecek, T. A., Propp, J. M., Stroup, N. E. & Kruchko, C. CBTRUS statistical report: primary brain and central nervous system tumors diagnosed in the United States in 2005-2009. *Neuro. Oncol.* **14 Suppl 5**, v1-49 (2012).
3. Lee, J. H. *et al.* Human glioblastoma arises from subventricular zone cells with low-level driver mutations. *Nature* **560**, 243–247 (2018).
4. Davis, M. E. Glioblastoma: Overview of disease and treatment. *Clin. J. Oncol. Nurs.* **20**, 1–8 (2016).
5. Stupp, R. *et al.* Effects of radiotherapy with concomitant and adjuvant temozolomide versus radiotherapy alone on survival in glioblastoma in a randomised phase III study: 5-year analysis of the EORTC-NCIC trial. *Lancet Oncol.* **10**, 459–466 (2009).
6. Stupp, R. *et al.* Radiotherapy plus Concomitant and Adjuvant Temozolomide for Glioblastoma. *N. Engl. J. Med.* **352**, 987–996 (2005).
7. Hegi, M. E. *et al.* MGMT Gene Silencing and Benefit from Temozolomide in Glioblastoma . *N. Engl. J. Med.* **352**, 997–1003 (2005).
8. Yan, H. *et al.* IDH1 and IDH2 Mutations in Gliomas . *N. Engl. J. Med.* **360**, 765–773 (2009).
9. Stupp, R. *et al.* Cilengitide combined with standard treatment for patients with newly diagnosed glioblastoma with methylated MGMT promoter (CENTRIC EORTC 26071-22072 study): a multicentre, randomised, open-label, phase 3 trial. *Lancet. Oncol.* **15**, 1100–1108 (2014).
10. McGranahan, T., Therkelsen, K. E., Ahmad, S. & Nagpal, S. Current State of Immunotherapy for Treatment of Glioblastoma. *Current Treatment Options in Oncology* vol. 20 24 (2019).
11. Kirson, E. D. *et al.* Alternating electric fields arrest cell proliferation in animal tumor models and human brain tumors. *Proc. Natl. Acad. Sci. U. S. A.* **104**, 10152–10157 (2007).
12. Stupp, R. *et al.* Effect of tumor-treating fields plus maintenance temozolomide vs maintenance temozolomide alone on survival in patients with glioblastoma a randomized clinical trial. *JAMA - J. Am. Med. Assoc.* **318**, 2306–2316 (2017).
13. McLendon, R. *et al.* Comprehensive genomic characterization defines human glioblastoma genes and core pathways. *Nature* **455**, 1061–1068 (2008).
14. Phillips, H. S. *et al.* Molecular subclasses of high-grade glioma predict prognosis, delineate a pattern of disease progression, and resemble stages in neurogenesis. *Cancer Cell* **9**, 157–73 (2006).
15. Verhaak, R. G. W. *et al.* Integrated genomic analysis identifies clinically relevant subtypes of glioblastoma characterized by abnormalities in PDGFRA, IDH1, EGFR, and NF1. *Cancer Cell* **17**, 98–110 (2010).
16. Wang, Q. *et al.* Tumor Evolution of Glioma-Intrinsic Gene Expression Subtypes Associates with Immunological Changes in the Microenvironment. *Cancer Cell* **32**, 42-56.e6 (2017).
17. Neftel, C. *et al.* An Integrative Model of Cellular States, Plasticity, and Genetics for Glioblastoma. *Cell* **178**, 835-849.e21 (2019).
18. Patel, A. P. *et al.* Single-cell RNA-seq highlights intratumoral heterogeneity in primary

glioblastoma. *Science (80-.).* **344**, 1396–1401 (2014).

19. Lauffenburger, D. A. & Horwitz, A. F. Cell migration: a physically integrated molecular process. *Cell* **84**, 359–69 (1996).

20. Albert, B. *et al. Molecular Biology of the Cell*. (Garland Science, 2008).

21. Gardel, M. L. *et al.* Mechanical integration of actin and adhesion dynamics in cell migration. *Annu. Rev. Cell Dev. Biol.* **26**, 315–33 (2010).

22. DiMilla, P. A., Barbee, K. & Lauffenburger, D. A. Mathematical model for the effects of adhesion and mechanics on cell migration speed. *Biophys. J.* **60**, 15–37 (1991).

23. Palecek, S. P., Loftust, J. C., Ginsberg, M. H., Lauffenburger, D. A. & Horwitz, A. F. Integrin-ligand binding properties govern cell migration speed through cell-substratum adhesiveness. *Nature* **385**, 537–540 (1997).

24. Chan, C. E. & Odde, D. J. Traction dynamics of filopodia on compliant substrates. *Science* **322**, 1687–1691 (2008).

25. Mitchison, T. & Kirschner, M. Cytoskeletal dynamics and nerve growth. *Neuron* **1**, 761 (1988).

26. Sunyer, R. *et al.* Collective cell durotaxis emerges from long-range intercellular force transmission. *Science* **353**, 1157–61 (2016).

27. Elosegui-Artola, A. *et al.* Rigidity sensing and adaptation through regulation of integrin types. *Nat. Mater.* **13**, 631–637 (2014).

28. Oria, R. *et al.* Force loading explains spatial sensing of ligands by cells. *Nature* **552**, 219 (2017).

29. Gong, Z. *et al.* Matching material and cellular timescales maximizes cell spreading on viscoelastic substrates. *Proc. Natl. Acad. Sci. U. S. A.* **115**, E2686–E2695 (2018).

30. Chaudhuri, O. *et al.* Substrate stress relaxation regulates cell spreading. *Nat. Commun.* **6**, 6365 (2015).

31. Mekhdjian, A. H. *et al.* Integrin-mediated traction force enhances paxillin molecular associations and adhesion dynamics that increase the invasiveness of tumor cells into a three-dimensional extracellular matrix. *Mol. Biol. Cell* **28**, 1467–1488 (2017).

32. Elosegui-Artola, A. *et al.* Mechanical regulation of a molecular clutch defines force transmission and transduction in response to matrix rigidity. *Nat Cell Biol* **18**, 540–548 (2016).

33. Prahl, L. S. *et al.* Microtubule-Based Control of Motor-Clutch System Mechanics in Glioma Cell Migration. *Cell Rep.* **25**, 2591-2604.e8 (2018).

34. Bangasser, B. L., Rosenfeld, S. S. & Odde, D. J. Determinants of maximal force transmission in a motor-clutch model of cell traction in a compliant microenvironment. *Biophys. J.* **105**, 581–92 (2013).

35. Klank, R. L. *et al.* Biphasic Dependence of Glioma Survival and Cell Migration on CD44 Expression Level. *Cell Rep.* **18**, 23–31 (2017).

36. Bangasser, B. L. *et al.* Shifting the optimal stiffness for cell migration. *Nat. Commun.* **8**, (2017).

37. Liu, C. J., Shamsan, G. A., Akkin, T. & Odde, D. J. Glioma Cell Migration Dynamics in Brain Tissue Assessed by Multimodal Optical Imaging. *Biophys. J.* **117**, (2019).

38. Estabridis, H. M., Jana, A., Nain, A. & Odde, D. J. Cell Migration in 1D and 2D Nanofiber Microenvironments. *Ann. Biomed. Eng.* **46**, 392–403 (2018).

39. Prahl, L. S., Stanslaski, M. R., Vargas, P., Piel, M. & Odde, D. J. Predicting Confined 1D Cell Migration from Parameters Calibrated to a 2D Motor-Clutch Model. *Biophys. J.* **118**, 1709–1720 (2020).

40. Ruoslahti, E. Brain extracellular matrix. *Glycobiology* **6**, 489–92 (1996).

41. Yang, B., Yang, B. L., Savani, R. C. & Turley, E. A. Identification of a common hyaluronan binding motif in the hyaluronan binding proteins RHAMM, CD44 and link protein. *EMBO J.* **13**, 286–96 (1994).

42. Peach, R. J., Hollenbaugh, D., Stamenkovic, I. & Aruffo, A. Identification of hyaluronic acid binding sites in the extracellular domain of CD44. *J. Cell Biol.* **122**, 257–64 (1993).

43. Ponta, H., Sherman, L. & Herrlich, P. A. CD44: From adhesion molecules to signalling regulators. *Nature Reviews Molecular Cell Biology* vol. 4 33–45 (2003).

44. Polyak, K. & Weinberg, R. A. Transitions between epithelial and mesenchymal states: Acquisition of malignant and stem cell traits. *Nature Reviews Cancer* vol. 9 265–273 (2009).

45. Bloushtain-Qimron, N. *et al.* Cell type-specific DNA methylation patterns in the human breast. *Proc. Natl. Acad. Sci. U. S. A.* **105**, 14076–14081 (2008).

46. Breyer, R. *et al.* Disruption of intracerebral progression of C6 rat glioblastoma by in vivo treatment with anti-CD44 monoclonal antibody. *J. Neurosurg.* **92**, 140–9 (2000).

47. Toole, B. P. Hyaluronan-CD44 interactions in cancer: Paradoxes and possibilities. *Clinical Cancer Research* vol. 15 7462–7468 (2009).

48. Naor, D., Nedvetzki, S., Golan, I., Melnik, L. & Faitelson, Y. CD44 in cancer. *Critical Reviews in Clinical Laboratory Sciences* vol. 39 527–579 (2002).

49. Dzwonek, J. & Wilczynski, G. M. CD44: molecular interactions, signaling and functions in the nervous system. *Front. Cell. Neurosci.* **9**, 175 (2015).

50. Banerji, S. *et al.* Structures of the Cd44-hyaluronan complex provide insight into a fundamental carbohydrate-protein interaction. *Nat. Struct. Mol. Biol.* **14**, 234–9 (2007).

51. Okamoto, I. *et al.* CD44 cleavage induced by a membrane-associated metalloprotease plays a critical role in tumor cell migration. *Oncogene* **18**, 1435–46 (1999).

52. Nagano, O. & Saya, H. Mechanism and biological significance of CD44 cleavage. *Cancer Sci.* **95**, 930–5 (2004).

53. Martin, T. A., Harrison, G., Mansel, R. E. & Jiang, W. G. The role of the CD44/ezrin complex in cancer metastasis. *Crit. Rev. Oncol. Hematol.* **46**, 165–186 (2003).

54. Legg, J. W. & Isacke, C. M. Identification and functional analysis of the ezrin-binding site in the hyaluronan receptor, CD44. *Curr. Biol.* **8**, 705–708 (1998).

55. Tsukita, S. *et al.* ERM family members as molecular linkers between the cell surface glycoprotein CD44 and actin-based cytoskeletons. *J. Cell Biol.* **126**, 391–401 (1994).

56. Yonemura, S. Ezrin/Radixin/Moesin (ERM) Proteins Bind to a Positively Charged Amino Acid Cluster in the Juxta-Membrane Cytoplasmic Domain of CD44, CD43, and ICAM-2. *J. Cell Biol.* **140**, 885–895 (1998).

57. Kim, Y. & Kumar, S. CD44-Mediated Adhesion to Hyaluronic Acid Contributes to Mechanosensing and Invasive Motility. *Mol. Cancer Res.* **12**, 1416–1429 (2014).

58. Wolf, K. J. *et al.* A mode of cell adhesion and migration facilitated by CD44-dependent microtentacles. *Proc. Natl. Acad. Sci. U. S. A.* **117**, (2020).

59. Freeman, S. A. *et al.* Transmembrane Pickets Connect Cyto- and Pericellular Skeletons

Forming Barriers to Receptor Engagement. *Cell* **172**, 305-317.e10 (2018).

60. Pietras, A. *et al.* Osteopontin-CD44 signaling in the glioma perivascular niche enhances cancer stem cell phenotypes and promotes aggressive tumor growth. *Cell Stem Cell* **14**, 357–69 (2014).

61. Vaillant, B. D. *et al.* CD44 as a prognostic and predictive marker for GBM. *J. Clin. Oncol.* **29**, 2049–2049 (2011).

62. Mooney, K. L. *et al.* The role of CD44 in glioblastoma multiforme. *Journal of Clinical Neuroscience* vol. 34 1–5 (2016).

63. Hanahan, D. & Weinberg, R. A. Hallmarks of cancer: The next generation. *Cell* vol. 144 646–674 (2011).

64. Hoelzinger, D. B., Demuth, T. & Berens, M. E. Autocrine factors that sustain glioma invasion and paracrine biology in the brain microenvironment. *J. Natl. Cancer Inst.* **99**, 1583–93 (2007).

65. Lefranc, F., Brotchi, J. & Kiss, R. Possible future issues in the treatment of glioblastomas: special emphasis on cell migration and the resistance of migrating glioblastoma cells to apoptosis. *J. Clin. Oncol.* **23**, 2411–22 (2005).

66. de Gooijer, M. C., Guillén Navarro, M., Bernards, R., Wurdinger, T. & van Tellingen, O. An Experimenter's Guide to Glioblastoma Invasion Pathways. *Trends in Molecular Medicine* vol. 24 763–780 (2018).

67. Bhat, K. P. L. *et al.* Mesenchymal Differentiation Mediated by NF-κB Promotes Radiation Resistance in Glioblastoma. *Cancer Cell* **24**, 331–346 (2013).

68. Mao, P. *et al.* Mesenchymal glioma stem cells are maintained by activated glycolytic metabolism involving aldehyde dehydrogenase 1A3. *Proc. Natl. Acad. Sci. U. S. A.* **110**, 8644–8649 (2013).

69. Ozawa, T. *et al.* Most human non-GCIMP glioblastoma subtypes evolve from a common proneural-like precursor glioma. *Cancer Cell* **26**, 288–300 (2014).

70. Yoshida, T., Matsuda, Y., Naito, Z. & Ishiwata, T. CD44 in human glioma correlates with histopathological grade and cell migration. *Pathol. Int.* **62**, 463–470 (2012).

71. Ahuja, D., Sáenz-Robles, M. T. & Pipas, J. M. SV40 large T antigen targets multiple cellular pathways to elicit cellular transformation. *Oncogene* vol. 24 7729–7745 (2005).

72. Doucette, T. *et al.* Immune heterogeneity of glioblastoma subtypes: extrapolation from the cancer genome atlas. *Cancer Immunol. Res.* **1**, 112–22 (2013).

73. Wiesner, S. M. *et al.* De novo induction of genetically engineered brain tumors in mice using plasmid DNA. *Cancer Res.* **69**, 431–9 (2009).

74. Calinescu, A. A. *et al.* Transposon mediated integration of plasmid DNA into the subventricular zone of neonatal mice to generate novel models of glioblastoma. *J. Vis. Exp.* 52443 (2015) doi:10.3791/52443.

75. Núñez, F. J. *et al.* IDH1-R132H acts as a tumor suppressor in glioma via epigenetic up-regulation of the DNA damage response. *Sci. Transl. Med.* **11**, (2019).

76. Koschmann, C. *et al.* ATRX loss promotes tumor growth and impairs nonhomologous end joining DNA repair in glioma. *Sci. Transl. Med.* **8**, (2016).

77. Brennan, C. W. *et al.* The somatic genomic landscape of glioblastoma. *Cell* **155**, 462 (2013).

78. Kuleshov, M. V. *et al.* Enrichr: a comprehensive gene set enrichment analysis web server 2016 update. *Nucleic Acids Res.* **44**, W90–W97 (2016).

79. Hou, J. C. *et al.* Modeling distributed forces within cell adhesions of varying size on continuous substrates. *Cytoskeleton* **76**, 571–585 (2019).

80. Tsukita, S., Oishi, K., Sato, N., Sagara, J. & Kawai, A. ERM family members as molecular linkers between the cell surface glycoprotein CD44 and actin-based cytoskeletons. *J. Cell Biol.* **126**, 391–401 (1994).

81. Fehon, R. G., McClatchey, A. I. & Bretscher, A. Organizing the cell cortex: The role of ERM proteins. *Nature Reviews Molecular Cell Biology* vol. 11 276–287 (2010).

82. Butler, J. P., Tolić-Nørrelykke, I. M., Fabry, B. & Fredberg, J. J. Traction fields, moments, and strain energy that cells exert on their surroundings. *Am. J. Physiol. Cell Physiol.* **282**, C595-605 (2002).

83. Klank, R. L., Rosenfeld, S. S. & Odde, D. J. A Brownian dynamics tumor progression simulator with application to glioblastoma. *Converg. Sci. Phys. Oncol.* **4**, 015001 (2018).

84. Ray, A., Morford, R. K., Ghaderi, N., Odde, D. J. & Provenzano, P. P. Dynamics of 3D carcinoma cell invasion into aligned collagen. *Integr. Biol. (United Kingdom)* **10**, 100–112 (2018).

85. Vey, N. *et al.* Phase I clinical study of RG7356, an anti-CD44 humanized antibody, in patients with acute myeloid leukemia. *Oncotarget* **7**, 32532–32542 (2016).

86. Menke-van der Houven van Oordt, C. W. *et al.* First-in-human phase I clinical trial of RG7356, an anti-CD44 humanized antibody, in patients with advanced, CD44-expressing solid tumors. *Oncotarget* **7**, 80046–80058 (2016).

87. Chaffer, C. L. & Weinberg, R. A. A perspective on cancer cell metastasis. *Science* vol. 331 1559–1564 (2011).

88. Arima, Y. *et al.* Decreased expression of neurofibromin contributes to epithelial-mesenchymal transition in neurofibromatosis type 1. *Exp. Dermatol.* **19**, (2010).

89. Krusche, B. *et al.* EphrinB2 drives perivascular invasion and proliferation of glioblastoma stem-like cells. *Elife* **5**, (2016).

90. Janda, E. *et al.* Ras and TGFβ cooperatively regulate epithelial cell plasticity and metastasis: Dissection of Ras signaling pathways. *J. Cell Biol.* **156**, 299–313 (2002).

91. Brubaker, D. K. & Lauffenburger, D. A. Translating preclinical models to humans. *Science (80-.).* **367**, 742–743 (2020).

92. Kim, D. *et al.* TopHat2: Accurate alignment of transcriptomes in the presence of insertions, deletions and gene fusions. *Genome Biol.* **14**, R36 (2013).

93. Trapnell, C. *et al.* Transcript assembly and quantification by RNA-Seq reveals unannotated transcripts and isoform switching during cell differentiation. *Nat. Biotechnol.* **28**, 511–515 (2010).

94. Scott, M. C. *et al.* Comparative transcriptome analysis quantifies immune cell transcript levels, metastatic progression, and survival in osteosarcoma. *Cancer Res.* **78**, 326–337 (2018).

95. Dickinson, R. B. & Tranquillo, R. T. Optimal estimation of cell movement indices from the statistical analysis of cell tracking data. *AIChE J.* **39**, 1995–2010 (1993).

96. Wang, Y.-L. & Pelham, R. J. Preparation of a flexible, porous polyacrylamide substrate for mechanical studies of cultured cells. *Methods Enzymol.* **298**, 489–496 (1998).

97. Boissonnas, A., Fetler, L., Zeelenberg, I. S., Hugues, S. & Amigorena, S. In vivo imaging of cytotoxic T cell infiltration and elimination of a solid tumor. *J. Exp. Med.* **204**, 345–356 (2007).

98. Halle, S. *et al.* In Vivo Killing Capacity of Cytotoxic T Cells Is Limited and Involves Dynamic Interactions and T Cell Cooperativity. *Immunity* **44**, 233–245 (2016).

99. Riggs, T. *et al.* A comparison of random vs. chemotaxis-driven contacts of T cells with dendritic cells during repertoire scanning. *J. Theor. Biol.* **250**, 732–751 (2008).

100. Halle, S., Halle, O. & Förster, R. Mechanisms and Dynamics of T Cell-Mediated Cytotoxicity In Vivo. *Trends in Immunology* vol. 38 432–443 (2017).

101. Humphrey, J. D., Dufresne, E. R. & Schwartz, M. A. Mechanotransduction and extracellular matrix homeostasis. *Nat. Rev. Mol. Cell Biol.* **15**, 802–812 (2014).

102. Swaminathan, V. & Waterman, C. M. The molecular clutch model for mechanotransduction evolves. *Nat. Cell Biol.* **18**, 459–461 (2016).

103. Razinia, Z. *et al.* Stiffness-dependent motility and proliferation uncoupled by deletion of CD44. *Sci. Rep.* **7**, (2017).

104. Nam, K., Oh, S., Lee, K., Yoo, S. & Shin, I. CD44 regulates cell proliferation, migration, and invasion via modulation of c-Src transcription in human breast cancer cells. *Cell. Signal.* **27**, 1882–94 (2015).

105. Subramaniam, V. *et al.* CD44 regulates cell migration in human colon cancer cells via Lyn kinase and AKT phosphorylation. *Exp. Mol. Pathol.* **83**, 207–215 (2007).

106. Zhu, H. *et al.* The Role of the Hyaluronan Receptor CD44 in Mesenchymal Stem Cell Migration in the Extracellular Matrix. *Stem Cells* **24**, 928–935 (2006).

107. Bangasser, B. L. & Odde, D. J. Master Equation-Based Analysis of a Motor-Clutch Model for Cell Traction Force. *Cell. Mol. Bioeng.* **6**, 449–459 (2013).

108. Zheng, Z. *et al.* Monoclonal antibodies to CD44 and their influence on hyaluronan recognition. *J. Cell Biol.* **130**, 485–495 (1995).

109. Lo, C.-M., Wang, H.-B., Dembo, M. & Wang, Y. Cell Movement Is Guided by the Rigidity of the Substrate. *Biophys. J.* **79**, 144–152 (2000).

110. Engler, A. *et al.* Substrate Compliance versus Ligand Density in Cell on Gel Responses. *Biophys. J.* **86**, 617–628 (2004).

111. Califano, J. P. & Reinhart-King, C. A. Substrate Stiffness and Cell Area Predict Cellular Traction Stresses in Single Cells and Cells in Contact. *Cell. Mol. Bioeng.* **3**, 68–75 (2010).

112. Trichet, L. *et al.* Evidence of a large-scale mechanosensing mechanism for cellular adaptation to substrate stiffness. *Proc. Natl. Acad. Sci. U. S. A.* **109**, 6933–6938 (2012).

113. Jiang, J., Zhang, Z., Yuan, X. & Poo, M. Spatiotemporal dynamics of traction forces show three contraction centers in migratory neurons. *J. Cell Biol.* **209**, 759–774 (2015).

114. Plotnikov, S. V, Pasapera, A. M., Sabass, B. & Waterman, C. M. Force fluctuations within focal adhesions mediate ECM-rigidity sensing to guide directed cell migration. *Cell* **151**, 1513–27 (2012).

115. Chen, C., Zhao, S., Karnad, A. & Freeman, J. W. The biology and role of CD44 in cancer progression: Therapeutic implications. *Journal of Hematology and Oncology* vol. 11 (2018).

116. Shamsan, G. A. & Odde, D. J. Emerging technologies in mechanotransduction research. *Current Opinion in Chemical Biology* vol. 53 125–130 (2019).

117. Moriarity, B. S. *et al.* Simple and efficient methods for enrichment and isolation of endonuclease modified cells. *PLoS One* **9**, (2014).

118. Marko, T. A. *et al.* Slit-Robo GTPase-Activating Protein 2 as a metastasis suppressor in

osteosarcoma. *Sci. Rep.* **6**, 39059 (2016).

119. Lim, C. T., Bershadsky, A. & Sheetz, M. P. Mechanobiology. *J. R. Soc. Interface* **7 Suppl 3**, S291-3 (2010).

120. Ingber, D. E. Cellular mechanotransduction: putting all the pieces together again. *FASEB J.* **20**, 811–827 (2006).

121. Paluch, E. K. *et al.* Mechanotransduction: use the force(s). *BMC Biol.* **13**, 47 (2015).

122. Roca-Cusachs, P., Conte, V. & Trepat, X. Quantifying forces in cell biology. *Nat. Cell Biol.* **19**, 742–751 (2017).

123. Elosegui-Artola, A., Trepat, X. & Roca-Cusachs, P. Control of Mechanotransduction by Molecular Clutch Dynamics. *Trends Cell Biol.* **28**, 356–367 (2018).

124. Cameron, A. R., Frith, J. E. & Cooper-White, J. J. The influence of substrate creep on mesenchymal stem cell behaviour and phenotype. *Biomaterials* **32**, 5979–5993 (2011).

125. Discher, D. E., Janmey, P. & Wang, Y. L. Tissue cells feel and respond to the stiffness of their substrate. *Science* vol. 310 1139–1143 (2005).

126. Ghassemi, S. *et al.* Cells test substrate rigidity by local contractions on submicrometer pillars. *Proc. Natl. Acad. Sci. U. S. A.* **109**, 5328–33 (2012).

127. del Rio, A. *et al.* Stretching single talin rod molecules activates vinculin binding. *Science* **323**, 638–41 (2009).

128. Cheng, S., Clarke, E. C. & Bilston, L. E. Rheological properties of the tissues of the central nervous system: A review. *Med. Eng. Phys.* **30**, 1318–1337 (2008).

129. Chaudhuri, O. *et al.* Hydrogels with tunable stress relaxation regulate stem cell fate and activity. *Nat. Mater.* **15**, 326–334 (2016).

130. Meng, F., Suchyna, T. M. & Sachs, F. A fluorescence energy transfer-based mechanical stress sensor for specific proteins in situ. *FEBS J.* **275**, 3072–3087 (2008).

131. Grashoff, C. *et al.* Measuring mechanical tension across vinculin reveals regulation of focal adhesion dynamics. *Nature* **466**, 263–266 (2010).

132. Borghi, N. *et al.* E-cadherin is under constitutive actomyosin-generated tension that is increased at cell-cell contacts upon externally applied stretch. *Proc. Natl. Acad. Sci.* **109**, 12568–12573 (2012).

133. Ringer, P. *et al.* Multiplexing molecular tension sensors reveals piconewton force gradient across talin-1. *Nat. Methods* **14**, 1090–1096 (2017).

134. LaCroix, A. S., Lynch, A. D., Berginski, M. E. & Hoffman, B. D. Tunable molecular tension sensors reveal extension-based control of vinculin loading. *Elife* **7**, (2018).

135. Morimatsu, M., Mekhdjian, A. H., Adhikari, A. S. & Dunn, A. R. Molecular Tension Sensors Report Forces Generated by Single Integrin Molecules in Living Cells. *Nano Lett.* **13**, 3985–3989 (2013).

136. Chang, A. C. *et al.* Single Molecule Force Measurements in Living Cells Reveal a Minimally Tensioned Integrin State. *ACS Nano* **10**, 10745–10752 (2016).

137. Austen, K. *et al.* Extracellular rigidity sensing by talin isoform-specific mechanical linkages. *Nat. Cell Biol.* **17**, 1597–606 (2015).

138. Zhang, Y., Ge, C., Zhu, C. & Salaita, K. DNA-based digital tension probes reveal integrin forces during early cell adhesion. *Nat. Commun.* **5**, 5167 (2014).

139. Cai, D. *et al.* Mechanical Feedback through E-Cadherin Promotes Direction Sensing during Collective Cell Migration. *Cell* **157**, 1146–1159 (2014).

140. Eder, D., Basler, K. & Aegerter, C. M. Challenging FRET-based E-Cadherin force measurements in Drosophila. *Sci. Rep.* **7**, 13692 (2017).

141. Ma, V. P.-Y. & Salaita, K. A brighter force gauge for cells. *Elife* **7**, (2018).